E864: Proposal for Funding

Measurements of Rare Composite Objects and High Sensitivity Searches for Novel Forms of Matter Produced in High Energy Heavy Ion Collisions

C.B. Dover, M. Schwartz, T.G. Throwe
Brookhaven National Laboratory, Upton, NY

M.S.Z. Rabin
University of Massachusetts, Amherst, MA

E.S. Hafen, P. Haridas, I.A. Pless
Massachusetts Institute of Technology, Cambridge, MA

C. Pruneau
McGill University, Montreal, Canada

J.R. Hall
University of New Mexico, Albuquerque, NM

T. Armstrong, R.A. Lewis, G.A. Smith
Penn State University, University Park, PA

K. Barish, G.E. Diebold, J. Germani, S.V. Greene, B. Shiva Kumar,
J. Lajoie, R.D. Majka*, J.T. Mitchell, F.S. Rotondo,
J.Sandweiss*, A.J. Slaughter, E.J. Wolin
Yale University, New Haven, CT

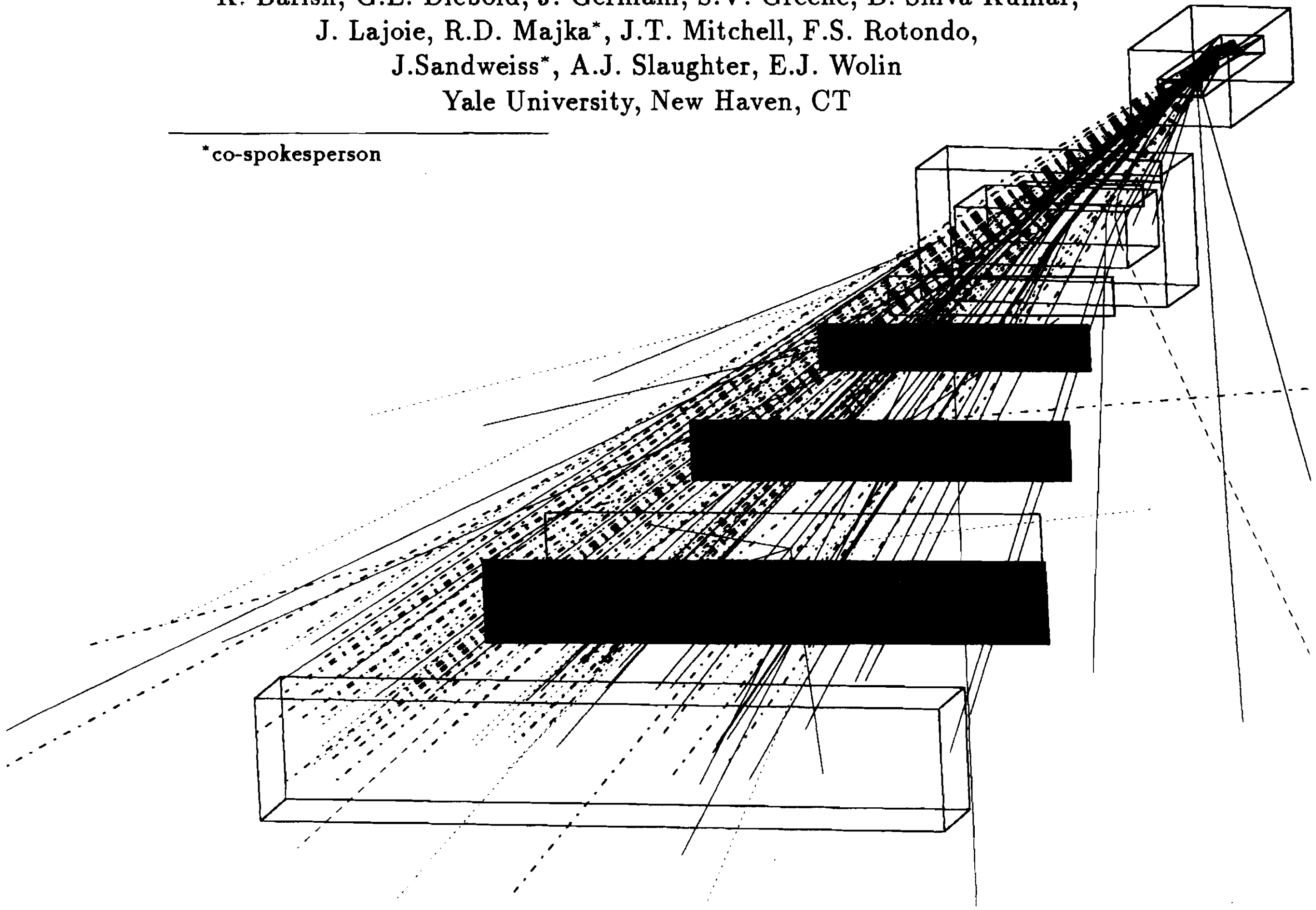

---

*co-spokesperson

Contents

List of Figures

List of Tables

E864: Proposal for Funding

Measurements of Rare Composite Objects and High Sensitivity Searches for Novel Forms of Matter Produced in High Energy Heavy Ion Collisions

1 Overview

1.1 Introduction

In this proposal we describe an experimental program to carry out high sensitivity searches for a variety of possible new particles, and high sensitivity measurements of known but rarely produced states.

In this overview we give a brief description of the goals and techniques of the experiment. This should provide an overall understanding of the experiment, and set the stage for a careful reading of the sections following. The individual sections on the physics, experimental method, etc., provide the detail needed to understand our goals and our claims regarding sensitivities and background rejections.

We point out that our design for E864, and our understanding of the physics potential of the high energy heavy ion collisions, was strongly influenced and encouraged by the participation of some of us in AGS experiment E814.

1.2 Physics Motivation and Historical Background

The concept of **strange quark matter, single multiquark bags** (in the sense of the MIT bag model) containing roughly **equal numbers of u, d, and s quarks**, dates back to the work of Jaffe [1] and Chin and Kerman [2]. In 1984 Witten [3] proposed that strange quark matter might be absolutely stable and might indeed be the true ground state of baryonic matter. In essence, the use of three types of quarks in "building" a single large bag avoids some of the energy penalty stemming from the **Pauli principle** when only two types are available. In addition, the negative charge of the strange quark causes the resulting droplets of quark matter to be nearly neutral, thus avoiding instabilities due to Coulomb repulsion energy.

Strange quark matter has many fascinating properties, and its existence would have major impacts on physics, astrophysics, cosmology, and possibly on technology as well [4]. A recent international workshop [5] reviewed the physics of strange quark matter and its role in astrophysics and cosmology. A remarkable conclusion from a recent letter of intent for a CERN strangelet search [6] was that "this hypothesis [strange quark matter] has not been scathed by seven years of intense and combined effort of cosmologists, astrophysicists, and hunters of exotica."

In essence, even though the consequences of the existence of strange quark matter are major, e.g. neutron stars are really strange quark matter stars (or perhaps have cores thereof), there is sufficient ambiguity in the parameters, and sufficiently limited data that the basic question remains open. Further, experiments with the requisite sensitivity (such as E864) have only recently been initiated.

Farhi and Jaffe [7] worked out the physics of strange quark matter in the context of the MIT bag model. **The term *strangelets* refers to strange quark matter systems of low baryon number, A, which are stable against strong decay but not necessarily against weak decay.** It is these which might be accessible in AGS high energy heavy ion experiments.

As is discussed in the section on physics goals, a sensitivity of $\approx 3 \times 10^{-11}$, the goal of E864, does allow significant constraints on the parameters of strange quark matter.

However, there is a more general motivation for a high energy heavy ion search with high sensitivity and broad reach. These collision systems represent a new "entrance channel" which has not been previously explored, and which make **new regimes of quantum numbers experimentally accessible.** Strange quark matter is the best known of such possible states, but there are others as well. The SU(3) chiral soliton (Skyrme) model predicts light ($A = 2, 3, 4$) clusters with multiple strangeness, which could be stable with respect to strong and even weak interactions. These predictions are speculative but sufficiently dramatic to merit an experimental test. The chiral solitons are not strangelets; the solitons are bound states of individual hyperons, while the quarks in a strangelet form a single state, and are not bound as a collection of individual baryons. Moreover, solitons may form bound composites with modest baryon numbers like $A \geq 2$, while strangelets are expected to be unstable when $A \lesssim 10$.

The fundamental point here is that high energy heavy ion collisions produce a system with high density of strangeness and baryon number in both configuration space and momentum space. States with multiple strangeness and/or baryon number can be produced which would have negligible production rates in other collision processes.

In addition, the collision system for high energy heavy ions is dynamically different from that encountered in "elementary particle" collisions. It has been speculated that if QCD is "slightly" broken or if, contrary to current thinking, QCD does not lead to absolute confinement of color, states of bare color might be much more readily produced in high energy heavy ion collisions than in simpler collision systems. These aspects are described more fully in the section on physics goals.

In summary, these collision systems provide a new dynamical regime whose study may result in discoveries of new elementary particle and nuclear systems.

1.3 Chronology of E864

Our interest in strangelets dates back to 1988 when, as members of BNL E814, we initiated a search for strangelets in the products of heavy ion collisions. The initial searches set upper limits on positively-charged strangelet production at the level 10^{-4} to 5×10^{-5} per interaction, depending on the strangelet's characteristics [8, 9]. These limits rule out some of the parameter space of the quark–gluon plasma production models [4]. E814 has recently collected additional data, which is presently being analyzed. This includes data on negatively-charged strangelets with expected sensitivity at the 10^{-4} level, and data on positively-charged strangelets with an expected sensitivity between 10 and 30 times better than that of E814's previous result [10]. Complementary data on antiproton production [11] and the coalescence of light nuclei [10] were also obtained.

Present sensitivity limits must be improved by about 6 orders of magnitude to critically test the existence of strangelets. This motivated a series of meetings in August and December of 1989 to study methods of searching for exotic composite objects in heavy ion collisions. About 35 physicists attended these meetings. In addition to E864's wide-band approach, two other serious designs were proposed. The first, by Hank Crawford, emphasized the measurement of negatively-charged particles in a focussing spectrometer. The second, by Shoji Nagamiya, specifically studied the neutral H-dibaryon. The E864 design emerged as a way to simultaneously study positively- and negatively-charged particles, as well as neutrals. This required a large acceptance so that the complete range of Z/A could be studied in a reasonable running time.

A collaboration formed to pursue the wide-band approach, and a proposal was submitted to Brookhaven's Program Advisory Committee (PAC) on 7 May 1990. The collaboration consisted of 14 physicists from Brookhaven, University of Massachusetts, McGill University, University of New Mexico, and Yale University. The PAC concluded that the wide-band approach was attractive, but that the decision should be deferred until the detectors were better understood and the collaboration was strengthened.

The collaboration, expanded by the addition of the Penn State University group, resubmitted the proposal in November 1990. The update included additional physics goals of the experiment, as well as more complete technical designs and background studies. The PAC concluded that the experiment had merit both for its discovery potential and its study of the production of nuclei and antinuclei. However, the PAC felt a panel of experts should be convened to study the proposal and to determine: (i) if the experiment could achieve the needed sensitivity, (ii) could be constructed within the $6M estimated cost (not including the beam line), and (iii) if the collaboration had sufficient strength to achieve its goals.

The panel, chaired by Doug Bryman (TRIUMF), included Hank Crawford (LBL), Hugh Brown (BNL), and Craig Woody (BNL). This panel concluded that the above three requirements were met, and that the experiment would be an exciting addition to the AGS physics program.

In March 1991, Brookhaven's PAC decided to approve E864 for 1200 hours of running for positive particles; the additional time we requested for negatives was deferred because at the time the Bryman Committee met, only positive running was reviewed.

Since the approval, the MIT group joined the collaboration, and the Brookhaven group was strengthened with the addition of M. Schwartz. Moreover, much progress has been made on background studies and detector development. These developments, along with the physics goals and cost estimates, are the subject of this proposal.

1.4 Design Considerations

E864 is designed to be sensitive to many of the speculative new composite states, and thus can detect particles with positive, negative, or zero charge.

The range of charge-to-mass ratio covered will be large, from $-1.0 \lesssim Z/A \lesssim -0.1$ during the negative-particle search to $0.1 \lesssim Z/A \lesssim 0.7$ in the positive-charge search. E864 will further be sensitive to particle production within about 1 unit of the center-of-mass rapidity, since almost all production models indicate that composite-object production will be peaked at the center-of-mass rapidity.

E864 will be capable of detecting particle states with proper lifetimes ≈ 50 ns or longer, while the sensitivity for shorter lifetimes will be compromised due to decay losses. This allows for detection of most metastable strangelet states. For example, strangelets undergoing most weak decays will have lifetimes between about 10^{-1} and 10^{-6} sec [2]. There is a possibility, currently under investigation, that particles decaying after the magnets could be identified in the E864 spectrometer as well. If feasible, this would extend our sensitivity to proper times of order 10 ns. Experiments for particles with shorter lifetimes, typical of hyperon decays, would be interesting but would require a completely different experimental approach.

E864 is designed to use the heaviest ions provided by the AGS, specifically the ^{197}Au beam (which should become available for physics experiments in the winter of 1993). Using this beam in conjunction with heavy targets, such as Pb or Au, will create final states with the most extreme conditions and greatest density of strangeness and baryon number.

Finally, E864 will study the production of a wide variety of known nuclear states which are expected to be produced in these collisions. These include both known light nuclei up to $A \approx 10$, and antinuclei through $A = -3$. These states are likely produced by the coalescence mechanism, which has proven to be an accurate production model at BEVALAC energies. Their production properties are of considerable interest in understanding the dynamics of the collisions, and they provide essential data for the interpretation of any negative results found in the searches. For example, it is possible to relate the coalescence production rates of strangelets to those for the light nuclei in a fairly model-independent manner. Thus it will be possible to interpret negative results in terms of a range of excluded strangelet parameters. Similar analyses are possible for other proposed multistrange baryonic systems.

1.5 Experimental Design

E864 is a mass spectrometer with high rate capability, large acceptance and excellent resolution. The detector measures magnetic rigidity, charge, time of flight, and energy (via calorimetry). High redundancy in the measurements is a key feature. The layout of the detector elements is shown in Fig. 5.

The magnet M1 is a standard AGS 18D72, and M2 will be borrowed from SLAC.

The symbols H1, H2, and H3 refer to scintillation counter hodoscopes. The counters are vertical slats and are read out at each end by phototubes so as to provide accurate time measurement via the mean time of the two photomultiplier tubes.

The symbols S1, S2, and S3 refer to straw tube proportional chamber stations. Each station consists of six planes: two vertical planes, two planes tilted at +20°, and and two planes tilted at −20°. Each coordinate (x,y,u) needs two planes in order to assure full efficiency. Station S1 is located inside the vacuum chamber.

Considerable study has gone into the design of the collimation and vacuum chamber. Background tracks from the vacuum chamber walls, magnet pole tips, etc. were studied using a detailed GEANT simulation. A satisfactory design was worked out, and is indicated in Fig. 6. The dimensions of the major detector elements are given in Table 1.

We plan to use the first two straw tube arrays as simple proportional counters without drift time information. The third straw tube will be used in the drift mode. The diameter of the tubes in the first two arrays is chosen to give acceptable occupancy, and is small enough to give the necessary resolution without drift time information. The third array is sufficiently far downstream so that a larger tube diameter (0.8

Element	Dimensions and Number of Detectors
Straw 1	128 cm wide by 22.5 cm high 6 layers of 0.4 cm diameter proportional counters total number of channels = 1,920
Straw 2	234 cm wide by 41.6 cm high 6 layers of 0.4 cm diameter proportional counters total number of channels = 3,510
Straw 3	513 cm wide by 82 cm high 6 layers of 0.8 cm diameter proportional counters total number of channels = 3,858
Hodo 1	280 cm wide by 48.0 cm high 256 scintillation counters, 1.094 cm wide, 0.5 cm thick
Hodo 2	392 cm wide by 64.0 cm high 256 scintillation counters, 1.531 cm wide, 1.0 cm thick
Hodo 3	584 cm wide by 88.0 cm high 256 scintillation counters, 2.281 cm wide, 1.0 cm thick
Calorimeter	7.2 m wide by 1.3 m high 936 Lead-scintillating fiber towers each 10 cm square, 1m long

Table 1: Dimensions of the E864 Spectrometer Elements

cm) can be tolerated and, with drift time information, excellent position resolution can be obtained. The straw tube detector will be the responsibility of the Penn State group, who have had experience with similar systems in Fermilab E760 and E706.

The thickness of the hodoscope counters is still under investigation. The dimensions indicated in Table 1 are known to be adequate, but we are investigating the possibility that the second and third hodoscope could be made somewhat thinner. Our design specification for the RMS mean-time resolution of the hodoscopes is 0.2 ns. We demonstrate in the chapter on experimental methods that this resolution can be achieved. The Yale (WNSL) group is taking major responsibility for this system.

The calorimeter, a lead/scintillating fiber "spaghetti" design, offers many advantages for the E864 application. This is the fastest known calorimeter, and has an expected RMS time resolution of 0.5 ns. The design is inherently hermetic, unlike calorimeters using wavelength shifters, and can be made completely compensating. Because of the compensation and the high degree of sampling, the spaghetti design offers the best known hadronic energy resolution. A stochastic term between $\Delta E/E = .3/\sqrt{E}$ and $\Delta E/E = .5/\sqrt{E}$ is achievable, depending on how we trade off cost and resolution. We have kept in close touch with the SPACAL collaboration at CERN, and our requirements have been met or exceeded by prototypes they have already built and tested [12].

It would be wasteful and expensive, however, to simply copy the SPACAL design. The SPACAL calorimeter is 2 m long so that it can measure particle energies of several hundred GeV. The E864 calorimeter may detect particles with energies as high as tens of GeV, but the depth of these showers will be dictated by the energy per baryon of the particle, which will be limited to the beam's 12 GeV/nucleon. The size of the constant term in the resolution is of much greater importance for the higher CERN energy application than for E864. Finally, we are crucially interested in the timing accuracy of the calorimeter, while the CERN program is not. For these reasons we will carry out a modest R&D program to optimize the spaghetti design for E864. This is further discussed in the section on experimental methods.

The few disadvantages of the spaghetti design, such as difficulty in longitudinal segmentation and possible sensitivity to radiation damage, are not important considerations for the E864 application. Finally, the Yale (YAUG) group is responsible for construction of the spaghetti calorimeter.

The groups building the remainder of the E864 apparatus are: The University of Mass, MIT, and the University of New Mexico are responsible for the trigger counter system. BNL is responsible for the DA system and late energy trigger. The BNL AGS department is taking responsibility for the beam line, counting house, AC power, etc.

1.6 Trigger and Backgrounds

The E864 trigger has two separate modes of operation. The first is optimized for the study of high-mass objects, while the second is for the study of low-mass objects.

First, a pretrigger will be imposed which requires an interaction in the target with sufficient multiplicity to indicate a "central" interaction. This will be a common pretrigger to both high-mass and low-mass searches.

A "late energy" trigger for the high-mass study will be used to detect mid-rapidity particles depositing 4 - 5 GeV or more in the calorimeter. The actual requirement will be that at least 3.3 GeV must be deposited in the peak tower with a time-of-flight at least 2 ns later than a $v = c$ particle. Any tower giving such a late energy signal will trigger the system. HIJET/GEANT simulations determined that 3.3 GeV is the appropriate cutoff to avoid triggering on commonly-produced central nucleons, while antideuterons, strangelets, and light nuclei with $A \geq 8$ will be efficiently found by this trigger. Monte-Carlo simulations indicate that such a late energy trigger will be sufficiently selective so that the system can operate with an interaction rate of 10^6 Hz.

Low-A nuclei and the multiply-strange dibaryons will not satisfy the late energy trigger because of their small energy deposition. However, such events are expected to be produced at substantial rates on the scale of the E864 sensitivity. We thus plan to run in the low-mass mode with the pretrigger requirement alone.

This two mode strategy will work well if the D/A system can accept roughly 4000 events per spill (spill time $\approx$ 1 s). A D/A system whose capacity exceeds this requirement is currently taking data in Fermilab experiment E791 (some members of the Yale group collaborate on E791). In fact, the D/A system for E864 requires only about 10% of the capability of the Fermilab E791 system. For our sensitivity calculations we have assumed a system with the required capacity will be available.

A considerable study of backgrounds has been carried out and is outlined in the section on backgrounds. We note that the Bryman committee analyzed our work carefully, and studied the large body of documentation we provided. The committee agreed with our conclusions, and made several helpful criticisms which led to useful changes in the details of our design.

One of the key features of E864 is the simultaneous measurement of the particle trajectories in space and time. Each photomultiplier tube is connected to a TDC and to an ADC, so that time and pulse height information are both available. Each scintillation counter thus provides a unique space-time point on the track. The horizontal coordinate is determined by the counter number, the vertical coordinate by the time difference between the top and bottom tubes, and the time-of-flight by the mean time of the two tubes. We chose the size of the counters to minimize the occupancy rate in each slat. If two particles strike the counter, the resulting time and vertical position will be in error for either of the incident particles. It is also required that the pulse heights in each plane agree within error.

The requirement that the same hits make a good space track AND a good time track, together with the redundancy provided by three hodoscope measurements, means that the only backgrounds of consequence are those which somehow produce a real track with a velocity within the range of interest for E864.

We have found (with Monte Carlo studies) that the largest background is due to neutrons which interact in the first or second straw tube plane (or the vacuum window) which produce a proton which makes the "good" track and which has a velocity close to that of the incident neutron. Such an event must occur in accidental coincidence with an overlapping cluster of neutrons which strike the same tower that the proton happens to aim at. This background enters at about the 10^{-11} level (of the total reaction cross section). Further, there are several handles left in the analysis which should reduce it further.

For the purely neutral states our analysis is not quite as far advanced, and in general the background will enter at a higher level. The more massive the neutral system, the smaller the background. For the H-dibaryon we have estimated that the background will enter at the 10^{-3} level. However, according to coalescence estimates, which should give fairly reliable lower limits to the cross section, the H should be produced at about the 10^{-3} level or greater. This would yield a very large number of H particles in our experiment, and signal-to-noise of the order of unity should be adequate. There are further analysis techniques (involving recognizing overlapping neutrons) which should further improve the signal-to-noise. For masses $\gtrsim$ 7 GeV, the neutral background level is below 10^{-5}. More complete studies are currently in progress.

1.7 Location of E-864 at the AGS

Working with the AGS liaison physicists and engineers, we have analyzed a number of possible locations for our experiment. It appears that the best solution, taking all factors (including cost) into account is to place the experiment in the A3 line. It would then operate in an exclusive OR mode with the TPC. At the present time there is no approved heavy ion experiment for the TPC but a letter of intent has been submitted. However, the experiment envisioned could probably share the beam in a reasonable fashion with E864 since the TPC experiment would not require most of the beam time and the transfer between the two experiments can be made in 4 to 6 hours.

The main advantage of the A3 location is that a beam line already exists to this location which is of higher quality than the D line, the other possibility. A complication of the A line location is the fact that E878, a quadrupole spectrometer-based experiment to measure yields of antideuterons produced in ^{28}Si beam heavy ion collisions and to search for new states at selected values of Z/A, is to be located in that line. Although E878 has not been approved for runs with the Au beam (the focus of E864), it is anticipated that if the apparatus performs as expected a gold beam run will be approved.

The current plan is to construct as much of E864 as possible while E878 is in place (the overlap occurs mainly at the front end), and, assuming no delays in schedule, to remove the E878 apparatus as soon as the winter 1993 heavy ion run ends. We would plan to install enough of the front end of E864 so that we could take some test data during the proton run in the spring and summer of 1993. The experiment, in its stage 1 design, would then be installed and would use the heavy ion run of the winter of 1994.

This plan illustrates another advantage of the A line location, namely, the ability to provide particles to the experiment during proton running. This would still be in an *OR* mode with the normal user of the A line during proton running. However, given the fast switching time it would seem that short test runs could be arranged. Such runs would be invaluable in getting the detector and the D/A system on the air. The alternate solution in the D line would not have permitted beams to the experiment during proton running.

1.8 Staging and Funding Plan

A complete discussion of the cost of E864 is given in the section on costs, so we give here some summary numbers and describe the plans for staging and funding the experiment.

The costs for the experiment can be divided as follows.

- The cost for BNL to build the beam, provide the analysing magnets, provide the counting houses, electrical power, and air conditioning totals \$2.53M. Of this, \$0.637M must be spent in FY 92 to remain on a schedule which permits the system to have a physics run in the winter of 1994. The costs estimated in succeeding years are \$1.393M in FY 93 and \$0.5M in FY 94.

- The costs for R&D which needs to be done to define the details of the detector total \$156k. All of this needs to be spent in FY 92 in order to remain on schedule. Major elements of this are \$70.5k for calorimeter R&D and prototype construction and \$44.2k for straw tube R&D and prototypes.

- The cost for the equipment of the experiment is estimated to be \$5.847M. This estimate includes all components. There is a possibility that this cost can be reduced by using existing equipment, e.g. cables. There may also be a significant saving if we are able to use the high voltage system developed for the HERA experiment ZEUS, in which small high voltage supplies are built into the base of each photomultiplier tube.

Because of the rather large cost of the detector, we have planned to build it in stages. For a variety of reasons our collaboration believes that it is essential for us to carry out significant new physics measurements in the run in the winter of 1994. The timeliness of the topic, the competition from CERN, and the essential role played by young postdoctoral scientists and graduate students in this program all tend to make a delay until 1995 for first results highly undesirable and possibly fatal to the experiment. The ability to do this is a constraint on the degree of staging which is acceptable.

Our plan is to provide all of the scintillation counter hodoscopes, the two straw chambers (S2 and S3) which are not inside the vacuum chamber, and about 25% of the calorimeter for the 1994 run. This staging defers about \$ 1.95M of equipment funds to FY 94 and, as noted previously, about \$ 0.5M of BNL costs for the beam, etc. to FY 94. With the detector described we can still make major advances in the new particle searches (levels of $\approx 10^{-10}$ rather than $\approx 10^{-11}$ for the full detector). The partial calorimeter will be located to optimize detection of neutrals and will permit searches for the H-dibaryon, neutral strangelets, etc.

1.9 Possibilities for Future Growth

Many improvements are possible in E864. The DA capacity can easily be increased by a large factor. By increasing the beam rate (not a problem in our proposed location) or target thickness, up to an order of magnitude more events could be recorded without a significant loss of efficiency due to overlapping events.

After gaining experience with the apparatus we could also implement a more sophisticated trigger, allowing the higher interaction rate to be used without actually increasing the number of events recorded.

Both of these two upgrades are relatively easy within the scope of the present design.

A major expansion of the E864 program could be implemented at RHIC using an internal gas jet target and downstream spectrometer similar to E864 (indeed many pieces of E864 could be used with minor modification). RHIC has many advantages: the higher energy at RHIC may be favored over AGS energies according to recent RQMD calculations [13]. Gas jet operation at RHIC will allow interaction rates up to 10^8 Hz which would be difficult with an extracted beam. The jet would also be "thin" so that seconderies would have negligible rescattering probability. The macro duty cycle at RHIC is 100%, a very significant advantage relative to the 20% of AGS fixed target operation. Because the kinematics (Lorentz boost, etc.) are similar to AGS fixed target operation, the E864 detectors, appropriately spaced, would remain useful for such an experiment.

2 Physics Goals

2.1 General Orientation

Relativistic heavy ion collisions in the central regime are characterized by the formation of dense, hot hadronic matter or perhaps, with luck, droplets of quark-gluon plasma. This zone of dense matter hadronizes into a large multiplicity of particles: in addition to an abundant supply of pions, one also finds antiparticles ($\bar{p}$) and strange particles ($K^{\pm}, \Lambda \ldots$) in the collision debris. Occasionally, composite objects can be formed, such as antinuclei ($\bar{d}, \bar{t}, \overline{^3\text{He}}$) and hadronic systems with multiple units of strangeness S (strangelets, the H-dibaryon, strange chiral solitons, etc.), assuming that the latter are indeed stable with respect to strong decay. Such objects are formed in only a tiny fraction of all heavy ion collisions, so an experiment of very high sensitivity is required to detect their presence, or to extract meaningful constraints on theoretical models from their absence. E864 is such an experiment, with unprecedented sensitivities in the range 10^{-10} to 10^{-11} per collision.

Why heavy ions? If we focus on the excitation of the strangeness degree of freedom in hadronic collisions, heavy ion collisions offer the only practical method of creating systems with multiple strangeness S, say $|S| \geq 3$. Reactions induced with strange meson beams, for instance (K^-, π^-) or (K^-, K^+) processes, can be used to produce single- and double-Λ hypernuclei, but only heavy ions enable us to go beyond the production of $S = -1, -2$ objects. In a heavy ion collision, each of the independent nucleon-nucleon collisions can lead to the creation of an $s\bar{s}$ strange quark-antiquark pair. It is already known from the first round of AGS experiments with Si beams at 15 GeV/nucleon that substantial numbers of strange particles are produced in central collisions [14]. For Au-Au collisions at the AGS, we anticipate that 10 - 15 Λ's will be produced in a typical central collision, permitting the exploration of a significant domain in strangeness and baryon number in experiment E864. We return to some more detailed theoretical estimates later.

E864 is an experiment with strong interdisciplinary aspects, with important implications in both nuclear and elementary particle physics. A fundamental question concerns the stability of strange quark matter. The strangelets proposed in Refs. [3] and [7] are stable in a certain domain of the underlying parameters of the Bag Model of quantum chromodynamics (QCD), namely the strange quark current mass m_s, the bag constant B, and the QCD coupling constant α_s. The effective parameters (B, α_s, m_s) determined by a fit to baryon ($A = 1$) and meson ($A = 0$) spectra cannot be reliably used to predict the binding energy of systems of larger (A, S), as emphasized by Ref. [7]. In particular, it is difficult to predict the minimum values of A and S for which strangelets are stable, even if one is convinced of the stability of such objects in the bulk limit (large A, with $A + S \ll A$). The question of the existence of strangelets, both large and small A, is one that must be resolved experimentally. This is a task that E864 can accomplish. Thus a dominant theme among the particle physics aspects of E864 is non-perturbative QCD: the limits we obtain on the production of multi-strange objects can provide significant constraints on effective models for the non-perturbative regime. As an example, consider dibaryons with $A = 2$, $S = -2$. The six-quark Bag Model [1] leads to the prediction of a stable H-dibaryon ($J^{\pi} = 0^{+}$, $I = 0$) in the SU(3) limit, while a version of the chiral soliton model [15] leads to a stable $\Sigma^{-}\Sigma^{-}$ bound state ($I = 2$). Both of these models are consistent with the observed spectroscopy of strange baryons. This illustrates the difficulty of extrapolating effective models of non-perturbative QCD, even by one unit in baryon number! As discussed in detail later, the expected production rates of the putative $\Sigma^{-}\Sigma^{-}$ bound state is well within the sensitivity of E864, and a meaningful limit on H production may be possible within the E864 setup.

The stability of strange quark matter is related to other problems in astrophysics and cosmology. For instance, if strangelets exist, they could be a candidate for "dark matter," as originally envisioned in Ref. [3]. The astrophysical problem of the strangeness content of the cores of neutron stars is also a closely related one, involving the equation of state of high density, low temperature hadronic matter.

Thus far we have mentioned only some specific motivations for E864 based on various speculative theoretical models. However, one should also emphasize the flexible and global nature of the open geometry, "wide band" approach adopted here, which is capable of accommodating the unexpected. E864 can be regarded as a general, high sensitivity search for new neutral or charged particles. We will provide limits on the production of fractionally-charged free quarks, as well as unanticipated neutral particles. For instance, there is the possibility, however remote, that SU(3) color symmetry is slightly broken in such a way that free gluons are produced rather than free quarks. Slansky *et al.* suggest that SU(3) is spontaneously broken to SU(2)×U(1) [16], and Saly *et al.* report that free gluons may arise as a result of dynamical symmetry breaking [17]. The phenomenological aspects of these suggestions were considered by Rinfret and Watson [18], and Berezinsky *et al.* [19]. The experimental signature of the hypothetical ninth gluon would be distinctive: it would appear as an massive neutral hadron. One might argue that the hot, dense hadronic soup resulting from a central collision of very heavy ions provides enhanced prospects for producing such new particles. The sensitivity of this experiment offers significant discovery potential.

E864 will also address a number of questions of fundamental interest in nuclear physics, such as the production rates or limits for a number of light nuclei, some rather ordinary ones (t, ^{3}He, ^{4}He, ^{6}Li...) and some unusual ones (^{7}B, ^{8}He, ^{11}Li...).

Excellent limits can be obtained on the production of neutron rich nuclei, for instance ^{4}H or ^{10}He, which have been searched for in numerous other experiments and not found, presumably because they are unstable with respect to strong emission of neutrons. The rates for central production of light nuclei provide a stringent test of coalescence models [20], in which such composite objects are formed at a late stage of the reaction process ("freezeout") from baryons which overlap in phase space. Such a coalescence picture works rather well at BEVALAC energies of 0.4 - 2 GeV/A [21], and it is important to establish whether this success extends to AGS energies, or whether additional cluster production mechanisms enter due to the formation of a hot and dense intermediate state of hadronic matter or even a quark-gluon plasma.

The rates for production of antinuclei in heavy ion collisions are a sensitive probe of the time dependent reaction dynamics. There is some preliminary evidence for the production of $\bar{d}$'s in heavy ion collisions at AGS energies [22], at a rate below that expected on the basis of the coalescence model. Antimatter is strongly absorbed in nuclear matter, due to annihilation processes such as $\bar{N}N \to \pi$'s or $\bar{d}N \to \bar{N} + \pi$'s. Thus $\bar{d}$, $\overline{^{3}\mathrm{He}}$, and $\bar{t}$ abundances will be very sensitive to hadron densities, a "formation time" for $\bar{p}$'s, and other features of the dynamics. Due to the very high sensitivity, E864 has a fair chance to observe $\bar{t}$ and $\overline{^{3}\mathrm{He}}$.

The rates for light nuclei formed in central collisions (as contrasted with beam fragmentation) are interesting in their own right as tests of models for heavy ion reaction dynamics, but they also serve to illuminate the coalescence production mechanism which is so important in understanding the meaning of the strangelet search. From the A dependence of production rates, one deduces a "penalty factor" for the addition of another nucleon to a cluster. From theoretical estimates or eventual measurement of cross sections for Λ or $\Lambda\Lambda$ hypernuclear production (E864 is not sensitive to these because of their short lifetime $\tau \approx 0.2$ ns), one obtains a similar "penalty factor" for the addition of a unit of strangeness to a cluster. Thus one can use measured rates for nuclear clusters as a baseline for coalescence estimates of strangelet production. We return to this point later.

We summarize the main areas of emphasis of E864:

a) search for strangelets, i.e. long-lived ($\tau > 50$ ns) multi-strange quark matter,

b) measurement of rates for antinucleus production,

c) measurement of cross sections for coalescence production of nuclei,

d) the unexpected: general high sensitivity search for new particles, both neutral and charged.

We now provide a more detailed discussion of a), b), and c).

2.2 Multi-Strange Clusters

We consider three examples of such objects, namely strangelets, the H-dibaryon and H-nuclei, and strange chiral solitons. We discuss the physics motivation for each case, and supply estimates of the production rates for such composites in heavy ion collisions at AGS energies.

2.3 Strangelets: Mass Formula

The basic idea that a new form of matter, so-called strange quark matter, might exist and be stable against strong decay (or possibly even absolutely stable) has been suggested in Refs. [2, 3, 7]. The discovery of strange quark matter, or the determination of significant upper limits for its production rate, is a major goal of the proposed experiment. The "new" matter consists of multi quark states containing u, d, and s quarks in a single "bag." In essence, the strangeness degree of freedom allows more quarks to occupy low lying levels than is possible with two flavors. This leads to the possibility that an assembly of baryon number, A, might be metastable or even stable when all of the quarks are in a single bag. This is in contrast to the case of ordinary nuclei where the quarks of a large A system are (mostly!) organized into 3 quark, color-neutral bags (the neutrons and protons) which interact with one another by meson exchange forces.

A mass formula of Bethe-Weizacker type for strangelets was developed in Ref. [23]. The energy $E(A,Y,Z)$ of a strangelet of baryon number A, hypercharge $Y = A + S$ (S = strangeness) and electric charge Z assumes the form

$$E(A,Y,Z) = \epsilon_0 A + 4\pi\sigma r_0^2 A^{2/3} + \frac{1}{2}\frac{\delta_Y}{A}(Y - Y_{\rm min})^2 + \frac{1}{2}\left[\frac{\delta_Z}{A} + \frac{6\alpha}{5r_0 A^{1/3}}\right](Z - Z_{\rm min})^2$$

The two parameters of the theory are the energy per baryon ϵ_0 in bulk matter (large A) and the strange quark mass m_s. The most stable strangelets have (Y,Z) close to ($Y_{\rm min}$,$Z_{\rm min}$). The quantities of interest here, namely the regions of $\{A, Y, Z\}$ where the system is stable with respect to weak and strong neutron emission, are much more sensitive to ϵ_0 than m_s. The strangelet surface tension, σ, radius parameter r_0, as well as the parameters δ_Y, $Y_{\rm min}$, δ_Z, $Z_{\rm min}$ of the above Taylor expansion can all be expressed in terms of m_s and an angle θ defined by

$$\frac{\epsilon_0}{m_s} = \left(2 + \left[\frac{1}{2}(1 + \cos^3\theta)\right]^{1/3}\right) / \sin\theta$$

In particular,

$$y_{\min} = Y_{\min}/A = \frac{1 - \cos^3\theta}{1 + \cos^3\theta}$$

$$r_0 = \frac{1}{m_s} \frac{\sin\theta}{[\frac{2}{3\pi}(1 + \cos^3\theta)]^{1/3}}$$

Typically, the strangelet density $\rho = 3/4\,\pi r_0^3$ is of order twice that of non-strange nuclear matter. In weak or strong neutron emission from strangelets, respectively, the energy releases $Q_{W,S}$ are given by

$$Q^n_W = E(A, Y, Z) - E(A - 1, Y, Z) - m_n$$

$$Q^n_S = E(A, Y, Z) - E(A - 1, Y - 1, Z) - m_n$$

The qualitative features of strangelet stability, as a function of $y = Y/A$ and A, for fixed $\epsilon_0 = 930$ MeV, $m_s = 150$ MeV/c^2 and $Z = Z_{\min}$, are shown in Fig. 1, taken from Berger and Jaffe [23]. For $A = 15$, typical stability regions in the (Z, Y) plane are indicated in Fig. 2, from Ref. [4]. As ϵ_0 increases towards the neutron mass m_n, the region of strong neutron decay marches to the left in Fig. 2, and intersects the weak decay region, which marches to the right. If there is a gap between the weak and strong decay regions, E864 would have the best chance of finding a stable strangelet with $A \approx A_{\min}$ and $y \approx y_{\min}$, in the vicinity of the dot in Fig. 1. At AGS energies, since the amount of strangeness produced is limited, the region of stability for $y < 0(|S| > A)$ is probably not accessible. For $Z \approx Z_{\min}$, the value of $A_{\min}$ is given roughly by

$$A_{\min}^{1/3} \approx \frac{8\pi r_0^2\sigma}{3}\left(\frac{1}{m_n - \epsilon_0}\right) \approx \frac{(60\text{MeV})}{(m_n - \epsilon_0)}$$

For $m_s = 150$ MeV, the variation of $A_{\min}$ with ϵ_0 is displayed in Table 2.

Note that θ, $Y_{\min}$, r_0 and σ vary only weakly with changes in ϵ_0, whereas $A_{\min}$ and the associated strangeness value $S_{\min} = (y_{\min} - 1)A_{\min}$ are very sensitive to ϵ_0.

There is clearly a limit to the amount of strangeness and baryon number that we can assemble in a bound strangelet, starting with the hadronic soup resulting from a central Au-Au collision. The coalescence estimates presented later, although perhaps somewhat conservative, suggest that composite strange clusters with $|S| + A \lesssim 14$ might be formed with measurable rates in E864. Thus if ϵ_0 is too large, we cannot fabricate a cluster with $S \approx S_{\min}$. Inspection of Table 2 reveals that if $\epsilon_0 < 910$ MeV, we are in the domain of sensitivity of E864. Viewed in the context of an assumed Bethe-Weizacker mass formula, the absence of a strangelet signal in E864 could be translated into a constraint on the volume term ϵ_0.

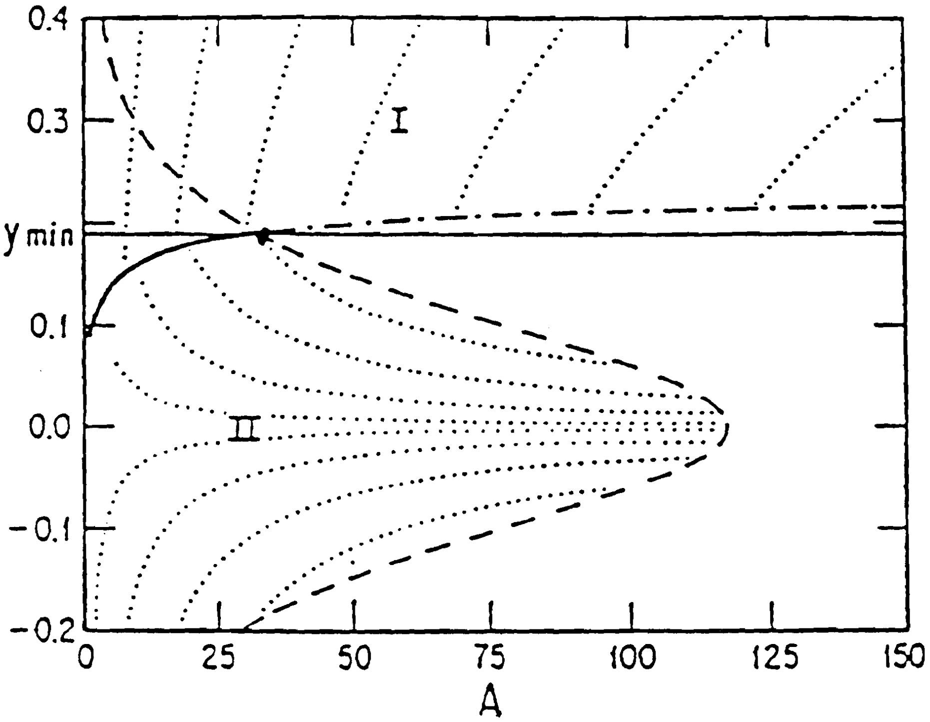

Figure 1: Strangelet stability as a function of Y and A for fixed $\epsilon_0 = 930$ MeV, $m_s = 150$ MeV/c^2, and $Z = Z_{min}$. From Ref. [23].

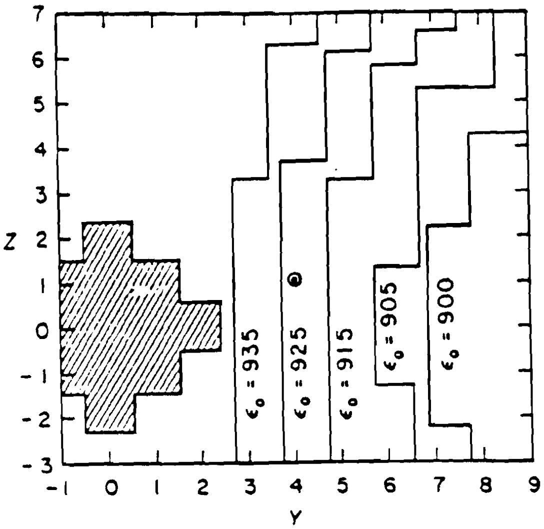

Figure 2: Stability regions in the (Z, Y) plane for an $A = 15$ strangelet. From Ref. [23].

ϵ_0	θ	$y_{\min}$	$A_{\min}$	$S_{\min}$
930	28.34°	0.189	275	−223
925	28.50°	0.191	73	− 59
920	28.67°	0.194	30	− 24
910	29.00°	0.198	9	− 7

Table 2: The variation of A_{min} with ϵ_0 for $m_s = 150$ MeV.

The calculations based on the MIT Bag Model, which yield a Bethe-Weizacker mass formula, are suggestive but clearly are not definitive predictions. Since this approach is essentially a Taylor series in $A^{-1/3}$, it is not reliable for small A. In particular, it is unclear at what minimum value of A stable strangelets ($Q_S < 0$, $Q_W < 0$) occur. Farhi and Jaffe [7] have done explicit quark shell model calculations for $A \lesssim 6$, finding no stable strangelets (the H-dibaryon is a possible exception, treated explicitly later). That perturbative calculation was based on one-gluon exchange; multi-quark states with a high degree of symmetry may become stable because of non-perturbative effects [24]. Thus one should properly regard the possible existence of strange quark matter as a question to be resolved by experiment.

2.3.1 Production of Strangelets in Heavy Ion Collisions

It is difficult to make quantitative estimates of strangelet production rates in heavy ion collisions. However, to set the scale, it is perhaps useful to provide rate estimates based on a conventional hadronic coalescence mechanism. This is a conservative approach which neglects other production processes that may occur in the earlier dense matter stage of the collision. The coalescence picture for the formation of ordinary non-strange nuclei is well established at BEVALAC energies (0.4 - 2 GeV/A) [21]. The number of clusters $N(A,S)$ of baryon number A and strangeness S produced per collision is written as

$$N(A,S) = \frac{N(A,S)}{N(A,0)}\frac{N(A,0)}{N_\alpha}N_\alpha,$$

where N_α is the number of α particles. The addition of one non-strange baryon to a cluster incurs a penalty factor P, while the conversion of a non-strange quark u, d to a strange quark s at fixed A leads to a strangeness suppression factor λ. Thus we have

$$\frac{N(A,S)}{N(A,0)} \approx \lambda^{|S|} \quad ; \frac{N(A,0)}{N_\alpha} \approx P^{A-4}$$

In the thermal model [25], we have

$$P \approx \rho_p \lambda_T^3 \quad ; \lambda_T = h/(2\pi m_p T)^{1/2}$$

where ρ_p is the proton density at freezeout, λ_T is the thermal wavelength and T is the temperature. From the t/p and α/p ratios measured in 2 GeV/A collisions at the BEVALAC, we obtain $P \approx 0.2$ [21]. For the higher energy AGS collisions, T is larger, and we estimate $P \approx 0.1$. The factor λ can be estimated in several ways: 1) from the observed Λ/p ratio at AGS energies ($\lambda \approx 1/10$); 2) from the measured [26] probability ratio $P(s\bar{s})/P(u\bar{u})$ in a variety of leptonic and hadronic collisions ($\lambda \simeq 0.1 - 0.15$); 3) from the assumption of thermal and chemical equilibrium of strange particles

$$\lambda \approx (N_{K^-}/N_{K^+})^{1/2} e^{-(m_\Lambda - m_N)/T} \approx \frac{1}{7}$$

All of these estimates lead us to the approximate value $\lambda \approx 1/10$, which we adopt here. Extrapolating the observed ratio $N_\alpha/N_p \approx 5 \times 10^{-3}$ (Ne-Pb at 2 GeV/A), we estimate the $N_\alpha/N_p \approx 2 \times 10^{-3}$ or $N_\alpha \approx 1/4$ for Au-Au collisions at the AGS. Note that N_α will be directly measured by E864, so this extrapolation will ultimately be unnecessary. Our rough guess is then

$$N(A,S) \approx \frac{1}{4} P^{A-4} \lambda^{|S|} \approx \frac{1}{4} 10^{4-A-|S|}$$

An experiment with sensitivity $\epsilon = 2.5 \times 10^{-n}$ could detect fragments with

$$|S| + A \leq 3 + n$$

with $n = 11$ for E864. This illustrates the importance of high sensitivity; a change of one order of magnitude in ϵ shrinks the accessible domain in $|S| + A$ by one unit. The region of sensitivity is enlarged somewhat if one considers N–N collisions which produce more than one $s\bar{s}$ pair (the thresholds for $NN \rightarrow \Xi KKN$ and $NN \rightarrow \Omega^- KKKN$ are at $s^{1/2} = 3.25$ and 4.1 GeV, respectively). With the guess $N(\Xi)/N(\Lambda) \approx \lambda/10 \approx 10^{-2}$ (the additional 1/10 from the restricted phase space for the Ξ), we arrive at the region of sensitivity for E864 shown in Fig. 3.

Strangelets are predicted to lie not far from the line $S + A = 0$ in Fig. 3, so one should be able to see such objects with up to seven units of strangeness. Note that E864 will also be able to find stable dibaryon states with high strangeness $|S| < 5$, if such composites exist. The strangelets are predicted to be of higher density than

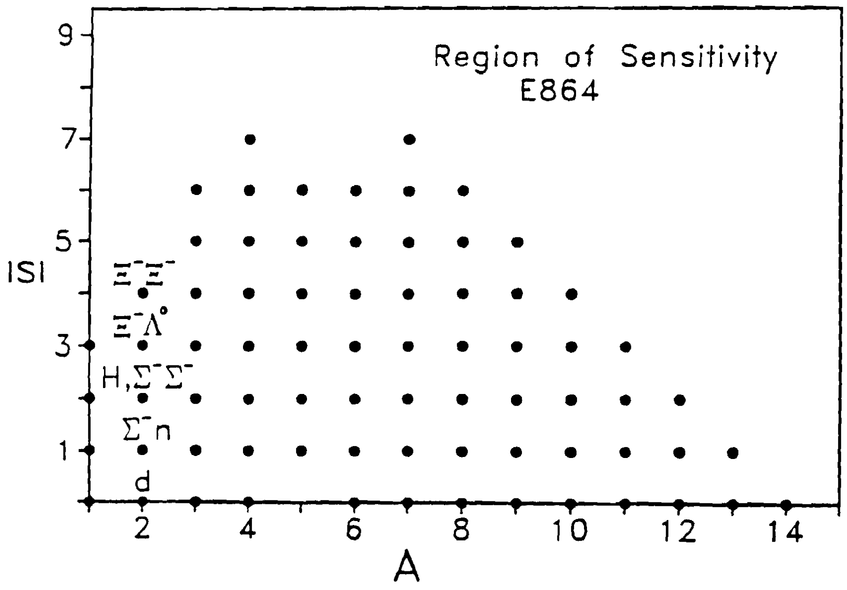

Figure 3: The sensitivity of E864, expressed in (S, A) space. Strangelets are expected to lie near $S + A = 0$.

ordinary nuclei, perhaps 1.5 - 2 ρ_0. Our coalescence estimates are normalized to the α which has a central density (in a very small volume) comparable to that of a strangelet. Thus we hope that wave function overlaps for a strangelet are not much smaller than we have estimated. Since we have included no explicit dependence of coalescence factors on the binding energy, our estimates might be taken to apply to formation rates for ordinary multi-Λ hypernuclei as well. We note that the experience to be gained from the E864 studies of the production of light nuclei and of the antinuclei will be crucial for a realistic application of coalescence models to strangelet production.

We emphasize that the above coalescence estimates are rather conservative. One of the most interesting aspects of strangelet production is the possible enhancement which could occur if "droplets" of quark–gluon plasma were to be produced in the collision [27, 28]. The basic idea is that as the quark–gluon plasma makes the transition to the final hadronic state, the kaons it radiates are primarily those bearing the antistrange quark, i.e. they are K^+ or K^0 rather than K^- or $\overline{K^0}$. This is understood in terms of the relative ease in finding a u or d quark as compared with finding a $\bar{u}$ or $\bar{d}$ quark in the baryon rich system formed by heavy ion collisions at AGS energies. Reference [28] predicts measurable probabilities for strangelet production via the "strangeness distillation" mechanism, starting from a droplet of quark–gluon plasma. This mechanism preferentially produces negatively-charged strangelets. Crawford, Desai and Shaw [29] have also estimated production rates for strangelets from a droplet of quark–gluon plasma. The production probability is given as a product of probabilities for: (i) plasma droplet formation, (ii) producing a system of baryon number A, and (iii) cooling the droplet by meson and later γ emission. The rates obtained are substantially larger than our coalescence estimates. As an example, they obtain strangelet formation probabilities for $A = 10$, $Z = -3$ between 10^{-5} for $S = -4$ and 8×10^{-10} for $S = -11$. Thus one might expect to detect strangelets with A as large as 20 – 25 with the high sensitivity of E864. However, this presupposes the formation of quark–gluon plasma in a certain sizable fraction of central Au–Au collisions at AGS energies, which is certainly a bold assumption. Calculations of absolute rates are clearly very uncertain. Our coalescence estimates are well normalized to the rate for the production of α's, an observable quantity which then serves as a calibration for the strangelet search. In any case, we conclude that if strangelets exist and if droplets of quark–gluon plasma with $A \geq 10$ are formed with any appreciable frequency, the proposed experiment will observe them. Indeed, one of the prime motivations for the use of the heaviest possible projectile ions is the desire to enhance the probability that regions of quark–gluon plasma will be produced in the collisions.

One general feature of all the production models is worth noting. In particular, they all predict that the mean transverse momentum of the produced strangelets will scale as $\sqrt{A}$. In thermodynamic models, this arises because the energy is the quantity which equilibrates and at the same energy, the momentum scales as the square root of the mass (at the temperatures reached in these collisions, the strangelet motion in the center of mass system is non relativistic).

In the quark–gluon plasma model, the larger the size of a droplet, the more hadrons it must radiate to reach its final state. These give rise to a random series of transverse momentum kicks and the final strangelet arrives at the random walk limit proportional to $\sqrt{A}$. A similar process occurs in the coalescence picture where the final transverse momentum is the result of a series of transverse momentum impulses due to the accreted constituents. We note that the mean transverse momentum of Λ^0 produced in 200 GeV/c per nucleon O–Au collisions [30] is ≥ 0.8 GeV/c, and the mean transverse momentum of protons is about 0.5 GeV/c. Indeed, there is a general tendency for the mean transverse momentum of particles to increase as the mass increases. We thus assume that the mean transverse momentum of strangelets produced in AGS heavy ion collisions will be given by:

$$\langle P_t \rangle = K\sqrt{A}$$

where the constant K is taken as

$$0.5\mathrm{GeV/c} \leq K \leq 0.9\mathrm{GeV/c}$$

The range of K should account for the uncertainty in the production processes at least in so far as the mean transverse momentum is concerned.

The sensitivity of E864 is discussed in detail in the sections on rates and backgrounds. In 1000 calendar hours of running, the strangelet search should reach a sensitivity (90% confidence level) of 3×10^{-11} per interaction. This level of sensitivity was assumed in Fig. 3. A number of possible improvements are conceivable to improve this level should that be necessary. This sensitivity represents a factor of $\sim 10^6$ over the level achieved to date in AGS experiment E814 [8] and a factor of $\sim 10^5$ over what we believe the limit to be in E814.

2.3.2 Weak and Strong Decays of Strangelets: An Example

It is perhaps useful to map out the region of stability of strangelets for a particular choice of the parameters $\{\epsilon_0, m_s\}$ in the assumed Bethe-Weizacker mass formula. For illustration, we take $\epsilon_0 = 900$ MeV, $m_s = 150$ MeV, corresponding to $\theta = 29.35°$. We then obtain

$$Y_{\min} = 0.2A, \quad Z_{\min} = 0.1A/(1 + 0.01A^{2/3})$$

$$4\pi\sigma r_0^2 = 87.2\mathrm{MeV}, \quad \delta_Y = 171.3\mathrm{MeV}, \quad \delta_Z = 183.7\mathrm{MeV}$$

The strangelet radius parameter is $r_0 = 0.91$ fm, corresponding to a density twice that of nuclear matter.

One can now determine the region of (A, Y, Z) values for which strangelets are stable with respect to both strong ($Q_S < 0$) and weak ($Q_W < 0$) hadron emission. In addition to neutron emission considered previously, we also consider stability with respect to proton or π^- emission. Stability against proton emission sets a limit on the amount of positive charge a strangelet may carry, while π^- stability constrains the amount of negative charge. The systems considered in this example are all stable with respect to strong or weak Λ and Σ emission. The Q values are given by

$$\begin{aligned}
Q_S^p &= E(A,Y,Z) - E(A-1,Y-1,Z-1) - m_p \\
Q_W^p &= E(A,Y,Z) - E(A-1,Y,Z-1) - m_p \\
Q_S^{\pi^-} &= E(A,Y,Z) - E(A,Y,Z+1) - m_{\pi^-} \\
Q_W^{\pi^-} &= E(A,Y,Z) - E(A,Y+1,Z+1) - m_{\pi^-}
\end{aligned}$$

We then have

$$\begin{aligned}\Delta Q^N &= Q_W^{p,n} - Q_S^{p,n} = \frac{\delta_Y}{2(A-1)}[1 + 2(Y_{\rm min} - Y)] \\ \Delta Q^\pi &= Q_W^{\pi^-} - Q_S^{\pi^-} = \frac{\delta_Y}{2A}[1 + 2(Y - Y_{\rm min})]\end{aligned}$$

For $Y > Y_{\rm min} + 1/2$, we have $\Delta Q^N < 0$, whereas for $Y < Y_{\rm min} - 1/2$, $\Delta Q^\pi < 0$; thus strong nucleon decay dominates where $|S|$ becomes too small and strong pion decay occurs when $|S|$ gets too large. Together, these decay processes provide bounds on S and Z for stable strangelets of fixed A. For example, the requirement of stability against strong π^- emission ($Q_S^{\pi^-} < 0$) implies

$$Z \geq Z_{\rm min} - A m_{\pi^-}/\hat{\delta}_Z,$$

with $\hat{\delta}_Z = \delta_Z + 6\alpha A^{2/3}/5r_0$. Since $Z_{\rm min} > 0$ and $Z_{\rm min}$ increases with A, the above condition does not permit stable negatively charged strangelets for large A. However, in the region of small $A \sim 10$ which is probed by E864, a substantial region of negatively charged stable strangelets is allowed. For our example, we have stability for

$$\frac{Z}{A} \geq 0.1 - \frac{m_{\pi^-}}{\delta_Z} \approx -2/3$$

Thus we arrive at an interesting conclusion: if we assume the form of the Bethe-Weizacker mass formula given by the Bag Model, and ϵ_0 is small enough to yield a region of stability, then most of the stable strangelets of small A will in fact be negatively charged. Stated another way: for small A, the requirement of stability against proton emission provides a rather stringent restriction on positive Z, while π^- emission allows a more generous region of negative Z.

To illustrate the above observations, we consider the stability of strangelets with $A = 7$, for the choice $\epsilon_0 = 900$ MeV. The condition of stability against proton emission rules out strangelets with $Z \geq 2$. For $Z \leq 0$, the proton stability conditions play no role, since they are less restrictive than those for neutron emission. The allowed regime of stability with respect to both weak and strong neutron and π^- emission is shown in Table 3. The lower bound on S comes from π^- emission and the upper bound from neutron emission. We include all entries for which the amount of negative charge is limited by the condition $Z \geq -|S|$, which characterizes systems composed of SU(3) octet baryons in the hadron basis (no Δ^-). Inspection of Table 3 discloses that there are 26 stable objects predicted with $A = 7$; of these, 17 are negatively charged. Of course, this zone of stability is very sensitive to our choice of ϵ_0: as ϵ_0 increases, the number of stable objects decreases, and the region of stability moves to higher A.

Z	Bounds on S
1	$-9 \leq S \leq -5$
0	$-8 \leq S \leq -5$
-1	$-8 \leq S \leq -5$
-2	$-7 \leq S \leq -5$
-3	$-7 \leq S \leq -4$
-4	$-7 \leq S \leq -4$
-5	$-6 \leq S \leq -5$

Table 3: Regions of stability of an $A = 7$ strangelet, with $\epsilon_0 = 900$ MeV.

The domain of stable $A = 7$ systems with $Z < 0$ is accessible to E864, and the experimental backgrounds are less severe than for $Z > 0$. We now refine our previous estimates of coalescence rates to include the Z dependence, in order to see which of these objects might be observed by E864. For $Z < 0$, the lightest hadronic configuration which can coalesce to form the strangelet is composed of n, Λ and Σ^- particles. Heavier configurations of the same (A, Z, S), where $n\Lambda$ is replaced by $\Sigma^- p$, are neglected; they could also contribute to coalescence, but are further "off-shell."

The generalization of our previous estimate for the number of strangelets N per collision is

$$N(A,S,Z) = (\frac{3}{2})^2 N_\alpha P^{A-4} \lambda^{|S|} (\frac{N_{\Sigma^-}}{N_\Lambda})^{|Z|}$$

for $Z < 0$, where P is the penalty factor for adding a neutron to a cluster, λ is the penalty for converting a neutron to a Λ, and N_{Σ^-}/N_Λ is the penalty for changing a Λ to Σ^- (this builds up the negative charge). The neutron-to-proton ratio for the Au-Au collision is 3/2; the factor $(3/2)^2$ reflects the conversion of the two protons in the α to neutrons. Using the values $N_\alpha = 1/4$, $P = \lambda = 1/10$, $N_{\Sigma^-}/N_\Lambda = 1/2$, we arrive at 26 stable strangelets with $A = 7$. Of these, 18 have rates $\geq 2 \times 10^{-11}$, and are thus likely to be within the sensitivity of E864. These 18 objects, along with their estimated production rates, are displayed in Table 4. Figure 4 also illustrates the stable $A = 7$ strangelets, with the 18 detectable strangelets circled.

If the sensitivity of the experiment were to be decreased to the 10^{-10} level, 13 of the above species are still detectable, at the 10^{-9} level, 6 are detectable, and at the 10^{-8} level, none are accessible. The importance of very high sensitivity is thus clear: the zone of stable and also detectable objects shrinks rather quickly with decreasing

S	Z	$N(7,S,Z)$
-4	-3	7×10^{-9}
-4	-4	4×10^{-9}
-5	1	4×10^{-9}
-5	0	6×10^{-9}
-5	-1	3×10^{-9}
-5	-2	1×10^{-9}
-5	-3	7×10^{-10}
-5	-4	4×10^{-10}
-5	-5	2×10^{-10}
-6	1	4×10^{-10}
-6	0	6×10^{-10}
-6	-1	3×10^{-10}
-6	-2	1×10^{-10}
-6	-3	7×10^{-11}
-6	-4	4×10^{-11}
-7	1	3×10^{-11}
-7	0	6×10^{-11}
-7	-1	3×10^{-11}

Table 4: Estimated number N of $A = 7$ strangelets per Au–Au collision. All are within E864's sensitivity.

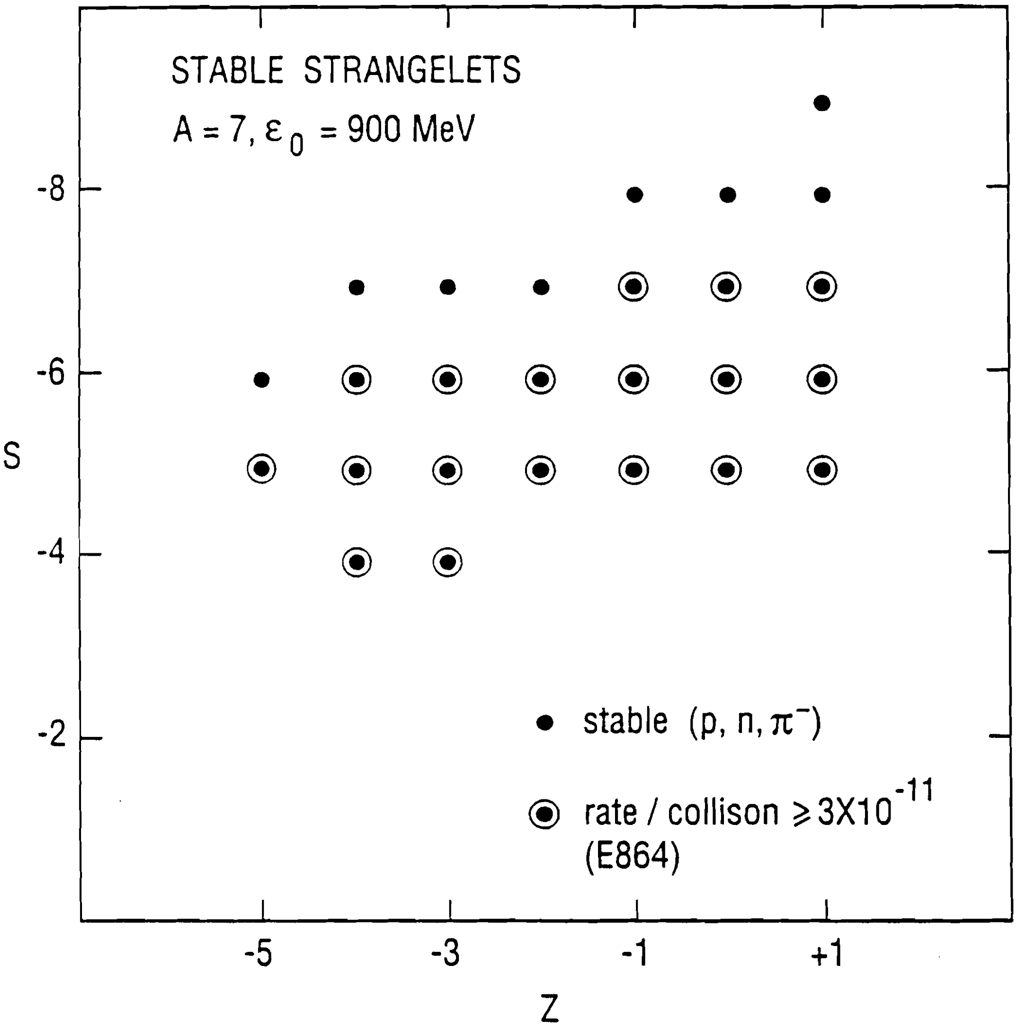

Figure 4: The $A = 7$ strangelets which are stable against strong and weak p, n, and π decay. The species which are likely to be accessible with E864's sensitivity are shown by circled dots. We have assumed a Bethe-Weizacker strangelet mass formula with $\epsilon_0 = 900$ MeV, $m_s = 150$ MeV, and estimated production rates with a simple coalescence model.

sensitivity.

It is important to note that the objects produced with the highest rate are near the boundary of the region of stability, in particular those with minimum $|S|$. In addition to the $A = 7$ strangelets shown in Table 4, a few of the stable $A = 8, 9$ systems could also be detected by E864.

The above discussion was based on the existence of a Bethe-Weizacker mass formula for strangelets, and the further assumption that the parameters δ_Y, δ_Z, $Y_{\min}$, and $Z_{\min}$ are uniquely related to ϵ_0/m_s as in the Bag Model. In this particular dynamical framework, E864 will serve to provide a lower limit on the energy per particle ϵ_0 of bulk strange matter, if no strangelets are found, assuming that the coalescence model estimates of production rates are reasonable.

2.4 The H-dibaryon and H-nuclei

The H particle, a dibaryon with the quantum numbers of two Λ's in the ${}^1S_0$ state ($J^\pi = 0^+$, $I = 0$, electrically neutral), is the most promising candidate for a deeply bound six-quark state. The $S = -2$ sector plays a special role in the spectrum of six-quark bag states, since only a six-quark system with $2u$, $2d$, and $2s$ quarks can exist in an SU(3)-flavor singlet configuration with spin zero, which takes maximum advantage of the attraction due to color-magnetic interactions arising from one-gluon exchange (OGE). Within the context of the MIT Bag Model, Jaffe was the first to note that the H could be deeply bound with respect to the $\Lambda\Lambda$ strong decay threshold [1]. Since Jaffe's pioneering work, there have been a number of attempts to refine the Bag Model calculation by including SU(3) breaking, center of mass corrections, etc. (see Ref. [31], for example). The problem of H binding has also been treated in various versions of the Skyrme soliton model [32, 33, 34], in lattice QCD [35], and in hybrid quark/gluon plus meson exchange models [36, 37]. Hybrid models in which the short range behavior is treated perturbatively via OGE generally yield a bound H, whereas if non-perturbative instanton effects are included at short distances, the H is pushed above the $\Lambda\Lambda$ threshold [38]. The repulsive three-body interaction generated by instantons only operates in the SU(3)-flavor channel, i.e., the H, and does not enter in baryon spectroscopy or nucleon-nucleon scattering. The most recent lattice QCD calculation, of course a non-perturbative result, yielded a very deeply bound H, near the mass of two neutrons [35]. Thus the various theoretical speculations range from a deeply bound H (binding energy of order $2m_\Lambda - 2m_n \approx 350$ MeV), as in lattice QCD calculations, to a loosely bound or even unbound object, as in various meson exchange models with some treatment of quark/gluon degrees of freedom at short distances. Clearly a sensitive H search is called for, in order to shed light on the fundamental question of the existence of strange dibaryons.

Several H searches are underway, most notably via the (K^-, K^+) double strangeness exchange reaction at the Brookhaven AGS [39]. In one version of the experiment, the $K^- + p \rightarrow K^+ + \Xi^-$ reaction is used to tag the production of the Ξ^- hyperon, which is then captured at rest via the two-body process $\Xi^- + d \rightarrow H + n$. The final state neutron is detected, rather than the H. In a second version, the $K^- + {}^3\mathrm{He} \rightarrow K^+ + H + n$ reaction is studied. Theoretical estimates exist for these cross sections, which are typically of order of a few tenths of a $\mu b/sr$ for the latter reaction [40, 41]. The K^- beam intensities at the AGS Booster are sufficient to measure such cross sections, but one does not have orders of magnitude in sensitivity to spare. In contrast, the H dibaryon is expected to be copiously produced in high energy heavy ion collisions, with estimated rates of order 10^{-2} to 10^{-3} per central Si–Au collision at AGS energies, based on several forms of the coalescence model [42, 43]. The H yield will be significantly higher in Au–Au collisions.

The (K^-, K^+) experiments do not detect the H directly, so there is no restriction on its weak decay lifetime. However, the $\Xi^- + d \rightarrow H + n$ branching ratio is likely to be measurable only if the H does not lie too far below the $\Lambda\Lambda$ threshold [41]. E864, on the other hand, is sensitive to the H if its lifetime τ_H is of order 50 ns or longer, because of the long flight time required. According to the lifetime estimates of Donoghue [44], τ_H exceeds 10 ns only if the H lies below the ΣN threshold (100 MeV below the $\Lambda\Lambda$ threshold). Thus E864 is sensitive to a deeply bound H, and is nicely complementary to the H search via the $\Xi^- + d \rightarrow H + n$ reaction, which can detect a weakly bound H.

Experiment E864 can search for the H directly by using time of flight and calorimetry. The main problem is the background due to neutrons and antineutrons. The H might be expected to be produced (because of its mass) at larger transverse momenta than those characteristic of neutrons. The large acceptance and its disposition will allow the search to extend to transverse momenta of 1.5 GeV/c. An analysis of the sensitivity of the proposed experiment for the direct detection of the H is presented elsewhere.

Another approach to searching for the H in heavy ion collisions is to look for the composites of the H which may well exist if the H is stable against strong decay [45]. The forces between two H's or between H and d are expected to be attractive and only a small amount of nuclear attraction is required to bind such systems. The $(HH)_{L=0}$ bound state with $J^\pi = 0^+$, $I = 0$, is an $S = -4$ analog to the α particle. There is also the possibility that three or more H's could be bound together. The rate of production of an HH bound state is expected to be of the order of 10^{-7}

to 10^{-9} per central collision and the rate for Hd should be greater, perhaps of the order of 10^{-6} [45]. The latter can be estimated from the ratio of t production to d production (which will be measured) and the calculated ratio of H to p production. If these composites exist, their production rates will be within the discovery range of E864.

Experimentally, the H composites provide signatures which are easier to separate from the background than is the case for direct H detection. The HH state should be cleanly separated from neutron backgrounds. For example, with a typical Lorentz factor of 2.0, the energy in the calorimeter from a neutron will be 0.94 GeV while the energy in the calorimeter from the HH will be 4.0 GeV. An antineutron with the same velocity will deposit 2.81 GeV in the calorimeter.

2.5 Multiply-Strange Chiral Solitons

In the SU(3) chiral soliton (Skyrme) model, there are predictions of a variety of light ($A = 2, 3, 4$) clusters with multiple strangeness, which could be stable with respect to strong and possibly even weak non-leptonic decays [46, 47]. This form of the soliton model is consistent with the masses of strange and non-strange baryons ($A = 1$). These predictions are very speculative, but sufficiently dramatic to merit an experimental test. These objects are distinct from strangelets, in that binding is already possible for very small A and negatively charged states are as stable as positively charged ones. They are also distinct from six quark bag states (e.g., the H) since soliton states of isospin $I \neq 0$ are bound (ex. $\Sigma^-\Sigma^-$, with $I = 2$). Some of the possible dibaryon ($A = 2$) soliton states are indicated in Table 5, together with the energy release Q in weak decay processes for systems bound at the strong decay threshold.

The binding energies of the above $A = 2$, $S = -2$ to -6 states are quite model dependent, but could be as much as 20% of the rest mass in the Skyrme model. As seen from Table 5, a binding energy of 5% is already sufficient to stabilize the $A = 2$, $I = 2$, $J = 0$ bound state ($\Sigma^-\Sigma^-$) against mesonic weak decay. Such an object could be detected by E864: it is negatively charged with $|e/m| \geq 0.78|e/m|\bar{p}$ and it requires only two units of strangeness for its production, a more favorable situation than for strangelets. Note that these $A = 2$ systems will not be strongly bound by conventional long (π) and medium (σ) range meson exchange. Their existence would represent a dramatic confirmation of the short range chiral dynamics of the SU(3) soliton picture. The dynamics of the six quark bag, with one-gluon exchange treated perturbatively, produces a different level order for the $A = 2$ system. In the bag, the color magnetic energy is minimized for SU(3) flavor representations of

Decay Process	Q (MeV)
$(\Sigma^-\Sigma^-) \rightarrow \Sigma^- n\pi^-, \Sigma^- ne^-\bar{\nu}$	118, 257
$(\Sigma^-\Xi^-) \rightarrow \Sigma^-\Sigma^-$	124
$(\Xi^-\Xi^-) \rightarrow \Xi^-\Sigma^-, \Xi^-\Lambda\pi^-$	124, 66
$(\Xi^-\Omega^-) \rightarrow \Xi^-\Xi^-, \Xi\Xi\pi$	351, 212
$(\Omega^-\Omega^-) \rightarrow \Omega^-\Xi^-, \Omega^-\Xi\pi, \Omega^-\Lambda K^-$	351, 218, 63

Table 5: Multiply strange chiral solitons and the predicted energy release, Q, for their weak decays (assuming zero binding).

minimum dimension, and hence $I = 2$ states like $\Sigma^-\Sigma^-$ are unbound. The search for negatively charged stable dibaryons is as fundamental as that for the neutral H. It bears directly on the dynamics of baryon–baryon interactions at short distances, a region where the meson exchange picture breaks down, and a correct treatment of quark degrees of freedom becomes crucial. E864 can provide significant limits: if the $\Sigma^-\Sigma^-$ state exists, it should be produced with easily measurable cross section in Au-Au collisions at the AGS. The other objects in Table 5 require more strangeness production, with correspondingly smaller cross sections.

Systems with $A = 3, 4, 5$ and several units of strangeness are also predicted to be bound [47]. Attractive cases for E864 include $\Sigma^-\Sigma^- n(I = 5/2,\ J = 1/2)$ and $\Xi nn(I = 3/2,\ J = 1/2)$. Again, one can show that these objects are not bound by long range forces (single pion exchange plus second order pion tensor interactions), so their existence would be a dramatic indication of significant attraction in the short-range interaction.

The weak decays of these objects have not been estimated. For $H \rightarrow \Sigma^- p$ weak decay, Donoghue *et al.* find a lifetime significantly longer than that of the Λ, because the enhanced $\{8\}$ weak interaction, responsible for the $\Delta I = 1/2$ rule, does not enter for a s-wave decay (the $\{1\} \rightarrow \{27\}$, $\Delta T = 3/2$ transition dominates) [44]. Similar effects may occur for some of the other $A = 2$ systems. For instance, the $\Omega^-\Omega^-$ bound state is a member of the $\{28\}$-plet of SU(3), while $\Xi\Omega$ states occur for $\{28\}$ and $\{35\}$. Thus in some cases, the weak lifetimes could be sufficiently long ($\tau > 10$ ns or so) for the particles to be detected by E864, even if the state is bound by less than the Q value shown in Table 5.

2.6 Antinuclei

The rates for antimatter production in high energy nucleus–nucleus collisions are of fundamental interest for several reasons. The yield of antiprotons ($\bar{p}$'s) is a sensitive probe of the space–time evolution of the baryon density, since $\bar{p}$'s, once created, can be strongly absorbed when they encounter a baryon, due to the annihilation reaction $N\bar{N}$ → mesons. There is now considerable data on $\bar{p}$ production from AGS experiments E802, E814 and E858 [48, 11, 22]. However, there is as yet no quantitative theoretical understanding of these data. In fact, there is considerable uncertainty concerning the mechanism for antimatter production. Gavin *et al.* argue that the $\bar{p}/p$ ratio is *suppressed* in heavy ion collisions, relative to the ratio seen in p-p collisions [49], whereas Ellis *et al.* suggest a $\bar{p}$ enhancement [50], based on a Skyrme-type model where the nucleon is identified as a topological soliton. In the approach of Gavin *et al.*, the suppression arises due to $\bar{p}$ annihilation with co–moving baryons, and for high energy central collisions, we have

$$(\frac{dN_p}{dy})/(\frac{dN_p}{dy}) \approx \frac{\bar{n}(t_0)}{n(t_0)}(\frac{t_0}{t_F})^{\beta}$$

where t_0 is a formation time for $\bar{p}$'s, t_F is the freezeout time, $\bar{n}(t_0)$ and $n(t_0)$ are the densities of $\bar{p}$ and p in the central region at $t = t_0$, and

$$\beta = \frac{\langle \nu\sigma_{NN} \rangle}{\pi R_A^2}\frac{dN_B}{dy}$$

Here $\langle \nu\sigma_{NN} \rangle$ is the averaged $\bar{N}N$ annihilation cross section, R_A is the projectile radius and dN_B/dy is the rapidity density of baryonic charge. The degree of suppression of the $\bar{p}/p$ ratio thus depends strongly on the formation time t_0. If a quark-gluon plasma is formed, an hadronic picture based on $\bar{N}$ absorption in a medium no longer applies. Ellis *et al.* regard the hadronization of a plasma droplet in terms of the formation of domains in which the quark–antiquark condensate $\langle q\bar{q} \rangle$ assumes independent values. If the orientations of $\langle q\bar{q} \rangle$ in adjacent domains are mismatched, "topological defects" may form, which are interpreted as baryons or antibaryons. This approach can lead to strong deviations from chemical equilibrium as the hadronization process unfolds, and an enhanced production of $\bar{p}$'s at levels which exceed the rate expected from an equilibrium Boltzmann distribution.

We mentioned the approaches of Gavin *et al.* and Ellis *et al.* to illustrate the diversity of theoretical predictions regarding $\bar{p}$ production. In fact, in heavy ion central collisions, the $\bar{p}$ is produced in a dense hadronic environment, not in a free space N-N collision, and a central theoretical challenge is how to include the effects of the medium on the production and propagation of antimatter.

The high sensitivity of E864 will permit us to extend the study of antimatter production beyond $\bar{p}$'s, to antideuterons ($\bar{d}$) and probably also $^3\overline{\mathrm{H}}$ and $^3\overline{\mathrm{He}}$. The measurement of composite antinuclear systems will shed light on a new set of theoretical questions. For instance, the production rates for the $\bar{d}$ and heavier antinuclei will be extremely sensitive to the space-time evolution of hadron densities during the collision process, through reactions like $\bar{d}N \leftrightarrow \bar{N} + \pi's$ and $\pi\bar{d} \leftrightarrow \bar{N}\bar{N}$, by which $\bar{d}$'s are created and destroyed. The free space rates for these processes are identical to measured cross sections for $\bar{p}d \rightarrow N + \pi's$ and $\pi d \leftrightarrow NN$, as follows from the CPT theorem. Will one be able to explain $\bar{d}$ cross sections in a hadronic cascade picture at AGS energies, with the above free space cross sections as input? Does one need to include additional effects of the dense medium, say by using density and temperature dependent effective cross sections $\sigma(\rho, T)$? Does a simple coalescence model apply to $\bar{d}, \bar{t} \ldots$ production? What is the influence of $\bar{p}$ formation time on the rate for antinucleus production? If the $\bar{p}$'s do not form until they are in a region of low density, one might expect a suppression of the $\bar{d}$ rate.

In p-p and p-nucleus collisions at high energies, $\bar{d}$ production seems to be consistent with a coalescence model. However, preliminary results from E858 [22], based on two $\bar{d}$ events, indicate that the $\bar{d}/\bar{p}$ ratio in Si–Au collisions at 14.6 GeV/A is an order of magnitude less than expected based on the coalescence model (with a coalescence probability obtained by fitting the observed d/p ratio). However, one should recall that deuteron production is the result of coalescence of pre-existing nucleons, while $\bar{d}$ formation requires that two antinucleons be produced in the collision, so the space-time dynamics of d and $\bar{d}$ formation are likely to be quite different.

In the coalescence model, the rate of $\bar{A}$ production is proportional to the Ath power of the $\bar{p}$ yield. This rule works for light nucleus cross sections at BEVALAC energies [21], and will soon be tested for d, t, ^{3}He and possibly α formation at AGS energies. However, it is not at all clear that this simple power law applies to $\bar{A}$ yields, since other dynamical mechanisms come into play, for instance formation time and strong annihilation. It has also been suggested that enhanced rates for $\bar{A}$ formation may provide a signature that the system evolved through an intermediate quark-gluon phase [51]. This results from an increased antiquark content in the plasma.

We now provide some rough estimates of the yields for antinucleus production. In the thermal coalescence model [25] discussed earlier in connection with strangelet production, we find

$$N(\bar{d})/N(\bar{p}) \approx 2.8P; \quad P = \rho_p \lambda_T^3$$

where ρ_p is the proton density at freezeout and λ_T is the thermal wavelength. Adjusting the penalty factor P to reproduce the E858 preliminary value of order 2×10^{-5}

for the $\bar{d}/\bar{p}$ ratio in Si–Au collisions, and extrapolating from Si–Au to the Au–Au case, assuming N_p increases by a factor of 3 (based on FRITIOF estimates), we estimate

$$N(\overline{^3\mathrm{H}}) \approx 2 \times 10^{-11}$$

per interaction. This is at the limit of sensitivity of E864. One could also assume that antinuclei are produced from a hadronic fireball in thermal and chemical equilibrium [52]; this gives yields per interaction in the range

$$N(\overline{^3\mathrm{H}}) \sim 5 \times 10^{-9} \quad \text{to} \quad 10^{-10}$$

This is presumably an upper limit, since it is unlikely that $\overline{^3\mathrm{H}}$ can be considered to be in chemical equilibrium. Thus it is clear that the high sensitivity of E864 is necessary in order to explore antinuclei heavier than the $\bar{d}$. Based on these crude estimates, the rate for $\bar{\alpha}$ will be too small to measure in E864 (or any other proposed experiment). However, there may be dramatic surprises (an enhancement due to formation of plasma droplets?) so a search is warranted.

2.7 Light Nuclei

Amongst the known nuclear species we expect to detect in E864 are d, t, ^{3}He, α, ^{6}He, and ^{8}He. Since we are studying central rapidities, these are most likely produced by coalescence rather than fragmentation, although this will be a matter for detailed study. Coalescence models and thermodynamic models both make testable predictions for the yields, rapidity distributions, and transverse momentum distributions of these products [53]. We note that the large acceptance of the design means that the rapidity and transverse momentum distributions are collected simultaneously. If we take the production models outlined in above as a rough guide, we estimate that for Au–Au collisions at 11.7 GeV/c per nucleon, that the yield of ^{8}He is about 3×10^{-1} per central collision or about 3×10^{-5} per interaction. Since experiment E864 is designed for a sensitivity better than 10^{-10} per interaction, the list of light nuclei noted above and heavier systems as well should be within our range. Our above estimates indicate that nuclei formed by coalescence up to $A = 14$ or so should be detectable by E864. The measurement of the production systematics for different species should allow a wide variety of tests of various models. We note that in almost any model, the yields of these composites are sensitive to the phase space densities of the "ingredients" at the freezeout stage of the collision. That is, the yields depend on the overlap in both momentum and configuration space. Thus the kind of information gained is rather different from that gained by measuring the spectra of "elementary" particles and is similar in nature to that gained by Hanbury-Brown–Twiss analyses.

The BEVALAC experiments at 0.4 – 2 GeV/A taught us that the coalescence model is very successful in correlating the production cross sections of light nuclei in heavy ion collisions. Does the coalescence description apply to Au–Au collisions at 11.7 GeV/A? E864 will provide an answer to this question; if "yes," the analysis of the data will enable us to extract coalescence probabilities. In the context of the thermodynamic model, we can then extract freezeout temperatures, and compare these with values obtained in the BEVALAC energy regime. We anticipate that coalescence probabilities will decrease with increasing energy (temperature). This remains to be established. The results would stimulate the further development of a microscopic theory of the coalescence probability, which takes account of the relativistic nature of the "fireball" expansion in high energy heavy ion collisions [43].

The abundances of light nuclei produced in Au–Au collisions are interesting in their own right as tests of dynamical models of heavy ion reactions. In addition, the rates for the production of light nuclei serve as an important calibration for the strangelet search. In the coalescence picture developed above, the production rates for multiply strange composite objects are related to the yield for the non-strange cluster of the same baryon number A. Thus, at least within a coalescence framework, we can attach a significance to the absence of a strangelet signal in E864, if this is indeed the case.

An interesting question is the following: Are there any manifestations, in the yields of light nuclei, of the intermediate state of hot, dense matter? Even in the absence of a quark–gluon plasma, the density and temperature prevailing during this transient intermediate state are expected to be higher at AGS than at BEVALAC energies. In the thermal model, rates for nuclear clusters depend only on the (ρ, T) values at freezeout, i.e., a rather late stage in the reaction process. It is important to provide data to test this picture in detail at AGS energies: this is one of the bread-and-butter tasks of E864. The main discovery potential of E864 lies in the search for strangelets and other unanticipated new particles. However, one must not lose sight of the fact that E864 will definitely measure the abundances of a number of light nuclei and antinuclei which are known to be stable against strong decay, providing strong constraints on models of collision dynamics. Finally, we mention that E864 can also explore the edge of the region of stability for light nuclear isotopes, particularly the neutron rich regime. For example, ^{4}He, ^{6}He, ^{8}He are known to be stable against strong neutron emission, but ^{10}He is thought to be unstable against strong decay. Searches for ^{10}He in lower energy heavy ion reactions were unsuccessful [54], lending support to this conclusion. Our rough estimates give $N({}^{10}\mathrm{He})/N_\alpha \approx 10^{-6}$, so ^{10}He would be measurable by E864, if it were stable. Among $Z = 3$ isotopes, ^{11}Li is known to be stable against strong decay (lifetime 8.5 ms), but ^{10,12,13}Li are not. All stable Li isotopes with $A \leq 14$ should be measurable in E864; the relative abundances of ^{6,7,8,9}Li will provide a test of the notion of a constant penalty factor P for the addition of a neutron to a cluster, which was a key assumption in our estimates of strangelet formation rates.

3 Experimental Method

3.1 General Strategy

The goal of E864 is to study particle production in heavy ion collisions at AGS energies using the heaviest beams available so as to maximize the chance of producing new heavy objects. Our approach is to use a mass spectrometer characterized by:

- High rate capability
- Large acceptance
- Excellent resolution
- Very low background rates achieved through redundant measurements

The apparatus is designed to have good acceptance in the central rapidity region and large acceptance in transverse momentum. A minimum production angle of 15 mr is required for a track to enter the detector. This minimum angle below the beam line is chosen to avoid most of the flux produced in the more common peripheral interactions. This will allow a broad search for new exotic states and a high sensitivity study of known particles.

The basic experimental approach is to utilize an open geometry spectrometer (see Fig. 5) built of three scintillation counter hodoscopes, three stations of straw tube wire tracking chambers and a tower geometry calorimeter which will be constructed with lead and scintillating fibers (longitudinal spaghetti design).

Each hodoscope counter will be viewed by two phototubes (one at each end) and each phototube will have an ADC and a TDC. Thus a particle traversing a hodoscope counter will have its horizontal position measured (via the location of the counter), its vertical position measured (via the time difference between the top and bottom tube), its time of arrival and its charge (via the pulse height). A new idea in the experimental design is that of insisting that candidate charged tracks form good tracks in space <u>and</u> in time. That is, the same "hits" in the hodoscope arrays must make good fits to a straight line in space (x,z and y,z) and to a straight line in time (t,z). The hits in the successive hodoscopes and in the calorimeter must slip relative to a velocity of light particle by the correct amount. The timing resolution of the hodoscopes is good enough (< 200 ps) so that the slip between each hodoscope plane is significant relative to the accuracy in the measurement of the time difference between planes for velocities of interest.

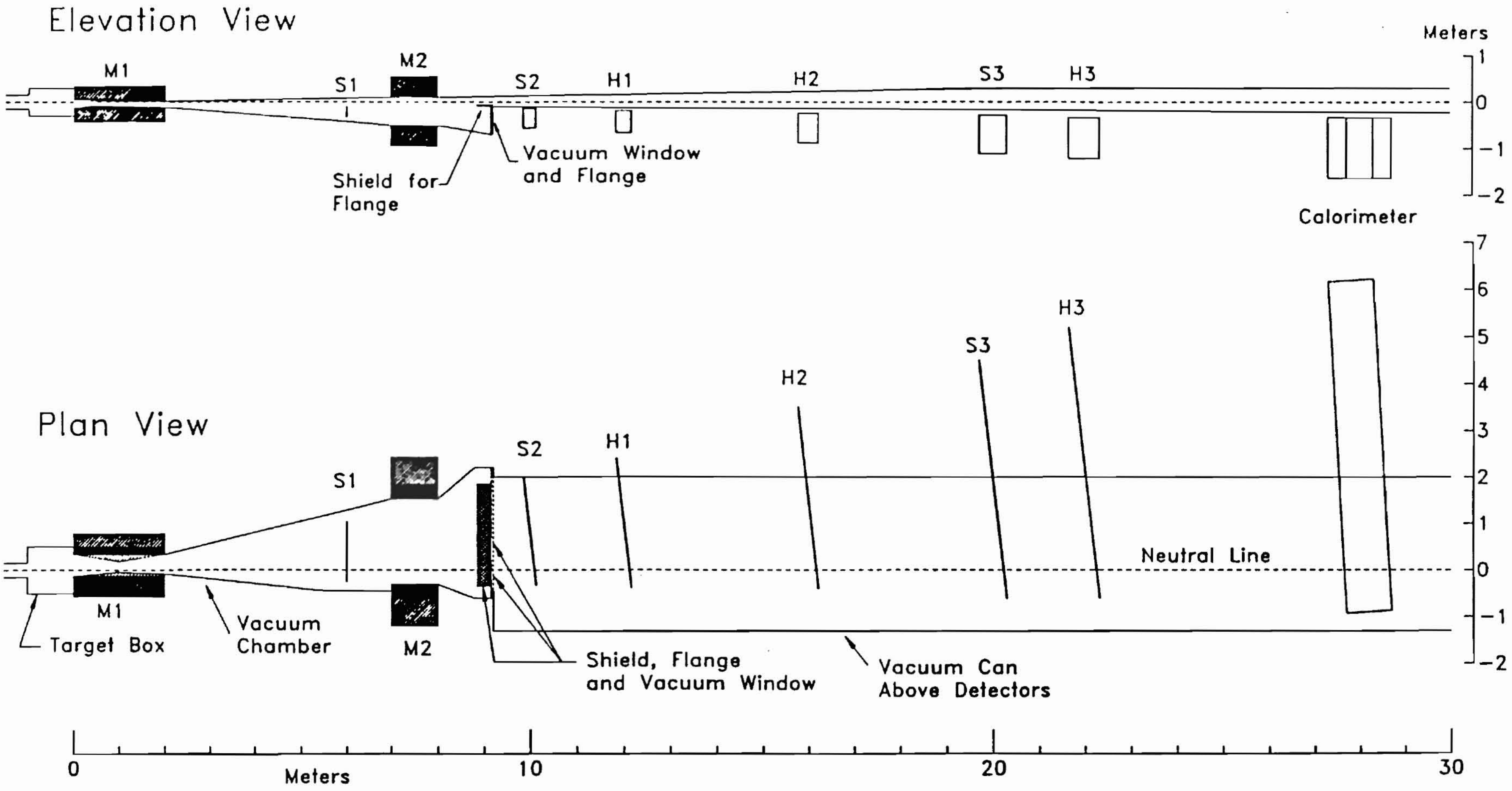

Figure 5: Detector Layout. Plan and elevation views are shown for the detectors. For clarity, sections at the neutral line are shown for the magnets, collimators and vacuum chamber. M1 and M2 are the dipole spectrometer magnets; H1, H2, H3 are scintillation counter hodoscopes; S1, S2, S3 are straw tube arrays.

Three arrays of straw tube wire tracking chambers will be used to provide precision tracking information for charged tracks. The improved spatial resolution over the hodoscopes aids in rejecting background. Additionally, the first station between the two spectrometer magnets provides a powerful check on whether a track originated at the interaction target.

For charged particles reconstructed in the spectrometer, the calorimeter will provide a confirming measurement. For neutrals the energy and time of flight measured in the calorimeter provide the only mass measurement. The calorimeter can also provide a selective high mass trigger - the "late energy" trigger discussed below.

Central interactions will be selected by a small, appropriately segmented, scintillation and/or Cerenkov counter array which also supplies a timing signal. The pseudo rapidity range over which the multiplicity is measured is chosen so that the multiplicity trigger is a good selector of centrality in the collision.

We plan to couple the apparatus to a relatively high rate data acquisition (DA) system which can record up to 4000 events per AGS beam spill. When used with just a multiplicity trigger this system will provide very large samples of minimum bias data. When used with the more selective late energy trigger we will achieve the desired sensitivity for high mass states.

E791 is 1600 Long words (32 bit) per event

The apparatus designed for E864 is also a basis for future experiments with even higher sensitivity since the incident beam for the experiment (10^7 ions per sec.) is a factor of 100 below the maximum that should be available at the AGS. One can also use a thicker target to generate an interaction rate up to 200 times that required for E864. As one learns how to deal with higher rates the sensitivity can be increased.

The use of a large acceptance (open) design has a number of advantages which favor it over the small acceptance spectrometer approach. Among these are:

10% Target?

- High sensitivity at modest beam rates. We require (instantaneous) beam rates of 1.0×10^7 ions per second.
- A number of related measurements and searches can proceed simultaneously.
- Correlation studies can be carried out.
- Considerable "growth" potential. Because the beam rate and target thickness are modest, they could be increased when the trigger and/or the DA system is improved.
- The large acceptance design is the most "open" to possible surprises in the rapidity or transverse momentum behaviour of the detected particles.

The major drawbacks of the open geometry design are the possible vulnerability to backgrounds from the target and the cost of the required high granularity detector. Our simulations show that the combination of timing and spatial resolution of the proposed hodoscope system coupled with the spatial resolution of the wire tracking system and the spatial, energy and time resolution of the calorimeter are sufficient to reject backgrounds at the required level.

We believe that the principal backgrounds will come from processes which produce a real track which has direction and velocity in the range of interest. This could arise for example, from a Λ^0 which travels through a large part of the magnetic field before decaying, or from a secondary interaction in the first straw planes or vacuum window creating a slow proton or pion which travels through the rest of the apparatus. Such background tracks are all singly charged so that the major problem would occur for Z=1 particles. Since we wish to reach the highest sensitivity for the charged particle searches, we believe that the greatest challenge by far will be to achieve adequate background rejection for charge +1 states. We have carried out major detailed Monte Carlo simulations for backgrounds to the charge +1 states which will be described below. We will also present the results of calculations and analysis for backgrounds to neutral searches.

3.2 Detector Design and Performance

Below we will discuss the design considerations of the various detector systems. The layout of the detector is shown in Fig. 5.

3.2.1 Magnets, Collimators and Vacuum Chamber

As indicated in Fig. 5 we will use a two magnet spectrometer. In earlier designs of this experiment we investigated a single magnet spectrometer but we found that certain backgrounds could be suppressed only by using two magnets with some separation between them. For a single magnet spectrometer, if the magnet is too short decays (particularly Λ^0) become a serious background. We concluded that we would need a magnet at least 4m long to adequately suppress the background due to Λ^0 decay. At a lower level, but still sufficient to compromise the desired sensitivity, interactions in the first detector leading to tracks in the apparatus which did not come from the target will produce a background. These (and Λ^0 decays) are highly suppressed by the calorimeter. However, just lengthening the first magnet does little to suppress the background due to interactions occurring in the first detector (which in a single magnet system is downstream of the magnet). A second magnet needs to be placed sufficiently far downstream that the particles of interest are sufficiently separated from the beam and peripheral products to allow a tracking chamber to be placed upstream of the second magnet. This gives a check on the assumption that tracks of interest come from the target.

Figure 6 shows the two magnets in plan and elevation view. The first magnet is a standard AGS 18D72 dipole. The second is a large aperture dipole which is available at SLAC. Also shown is the collimation in the first magnet, the tracking chamber (S1), and some shielding downstream of the second magnet. The collimator in the first magnet is designed to shield the pole tips and coils of the second magnet but still give full acceptance for the downstream detectors. The upstream end of this collimator will be modified as we refine the interaction trigger and beam design. We have studied the collimation in the first magnet by using GEANT to fully track all interaction products from particles entering the collimator. We find that with a suitable shape the increase in hits in the charged particle detectors is modest ($< 30\%$). There is a significant increase in the number of particles entering the calorimeter (about a factor of 2), but almost all of the increase is from very low energy photons ($< 10MeV$) which should have little effect on the performance of the calorimeter.

The vacuum chamber is designed so that the beam and most of the peripheral interaction products remain in vacuum through the length of the experiment. Since we plan to run with several different values of magnetic field in the spectrometer magnets, the beam downstream of the magnets will have several different trajectories. This necessitates having a rather large vacuum chamber downstream of the magnets. We have found that allowing some of the produced peripheral protons to intersect the vertical walls of vacuum chamber does not produce any significant flux in the detectors. This is because of the somewhat unfavorable geometry for such interactions to produce secondaries in the right direction and also because we will include a shielding layer between the vacuum chamber and the detectors. We have run simulations with 2.5cm of lead at the bottom of the vacuum chamber. However, the bottom wall of the vacuum chamber which will be one to two inches of steel may also provide adequate shielding.

Since we do not wish to place all the detectors inside the vacuum chamber, there must be a vacuum window. As discussed below, we believe we can operate the first tracking chamber in the vacuum. This means that the vacuum window will be just downstream of the second magnet. This window adds some material in the particles' path and has been included in our analysis of potential background. A more serious problem for the successful operation of the detectors is the flange required to support the vacuum window. This flange will represent several centimeters of aluminum or steel which is enough material to provide a substantial target for particles impinging

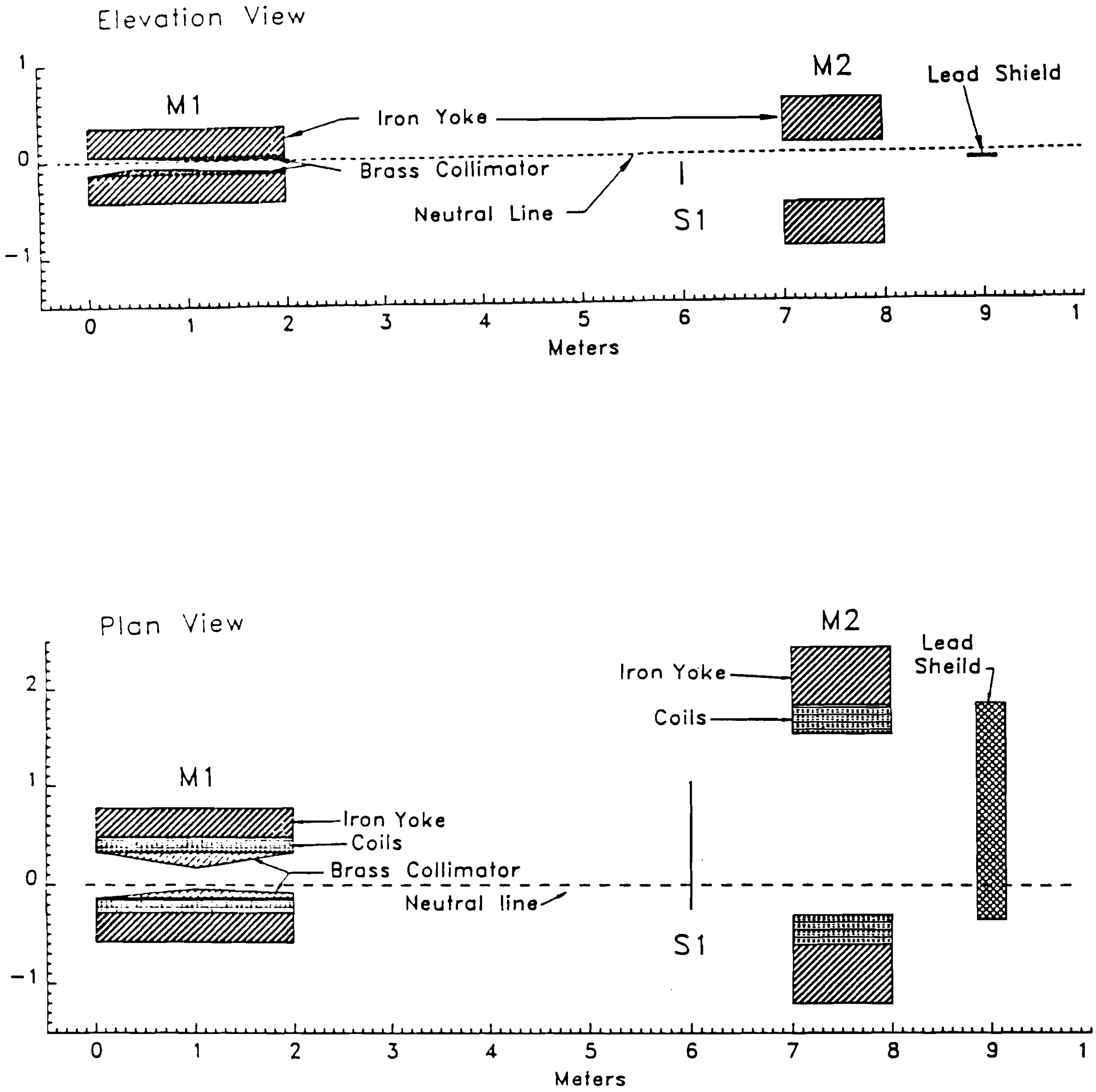

Figure 6: Magnets, collimation and shielding of vacuum flange - plan and elevation view.

Table 6: Dimensions and location of Scintillator Hodoscopes

Array	Number of counters	Longitudinal Position (0m=target)	Nearest edge to neutral line (vertical)	Size (vert. x horiz.)
H1	256	12.0m	0.1805m	0.48 x 2.80m
H2	256	16.0m	0.2410m	0.64 x 3.92m
H3	256	22.0m	0.3300m	0.88 x 5.84m

on the flange, but not enough material to stop or significantly scatter the secondaries produced in the flange. GEANT simulations show that the presence of such a vacuum flange significantly increases the multiplicities in the detectors downstream due to interactions in the flange. We have found that placing a shielding plug of dense material just upstream of the flange can stop or sufficiently scatter the secondaries so that very little additional flux enters the downstream detectors. In particular, a lead shield 30cm in the beam direction, 3.5cm vertical and long enough horizontally to completely shadow the section of the vacuum flange toward the beam is adequate. Figure 7 shows an elevation view of a typical Au-Au collision fully tracked through the apparatus with all secondaries from shielding interactions included. The plot is highly anamorphic, hence the deceptive appearance of many very wide angle tracks emerging from the shields. One can see that an appropriately sized and placed shield plug upstream of the vacuum flange not only shields the downstream detectors, but in combination with the bottom shield plate on the vacuum chamber creates a "quiet zone" just under the vacuum chamber. This is quite useful in providing a place for light pipes, phototubes, bases, cables and other detector services which will be required.

3.2.2 Hodoscope Design Considerations

The hodoscope arrays are the heart of the tracking and background rejection for charged particles. Figure 8 shows a section of the first hodoscope array. Table 6 lists the location, dimensions and number of counters in each hodoscope. By using the timing information from the top and bottom phototubes on a counter, a space point and a time point is obtained for each hit as well as pulse height (charge) information. In analyzing Monte Carlo simulated data from the hodoscope arrays,

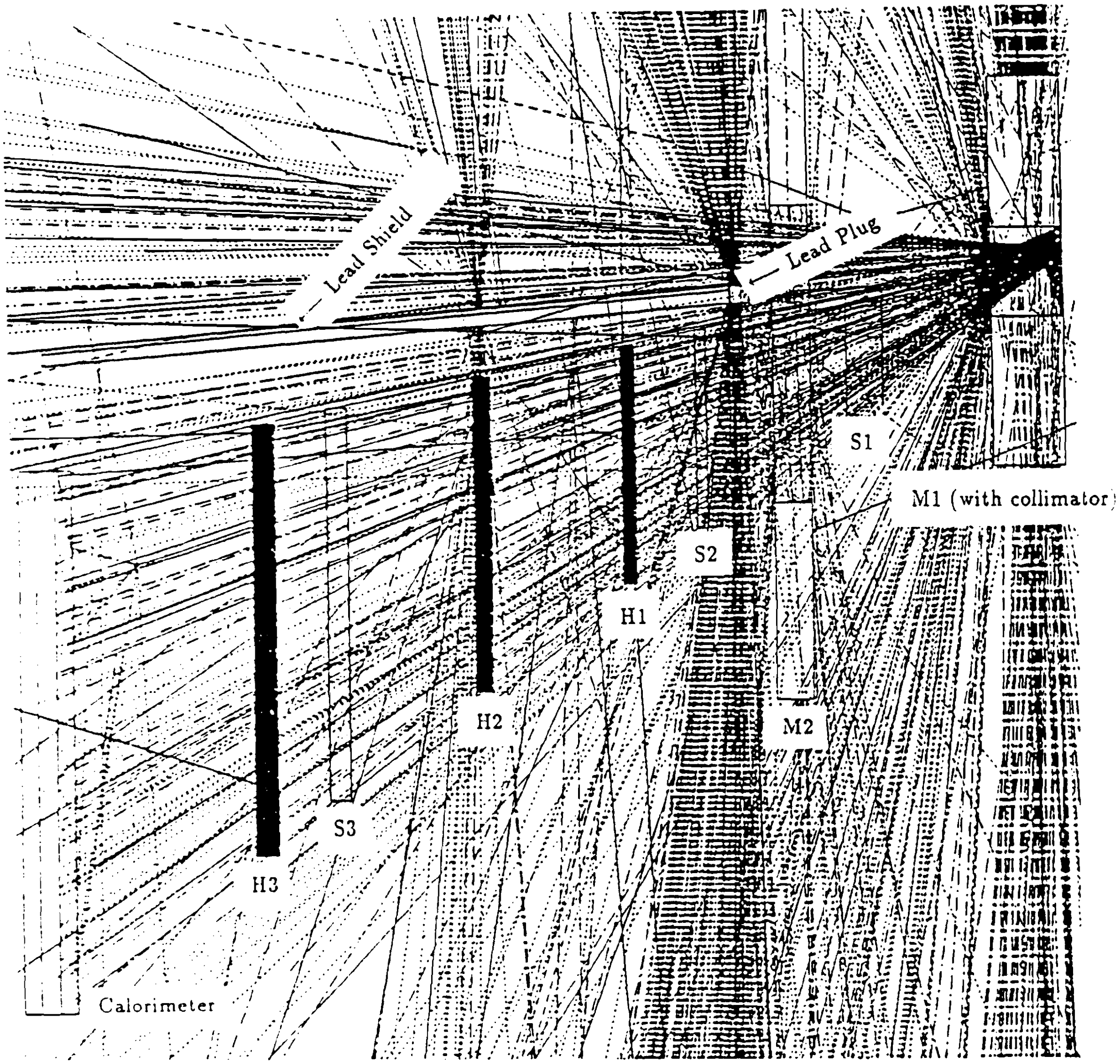

Figure 7: GEANT simulation of Au-Au collision including all tracks from collimation, shielding, vacuum flange - elevation view. Dashed and dotted tracks are neutrals. Tracks are not drawn inside iron or shielding.

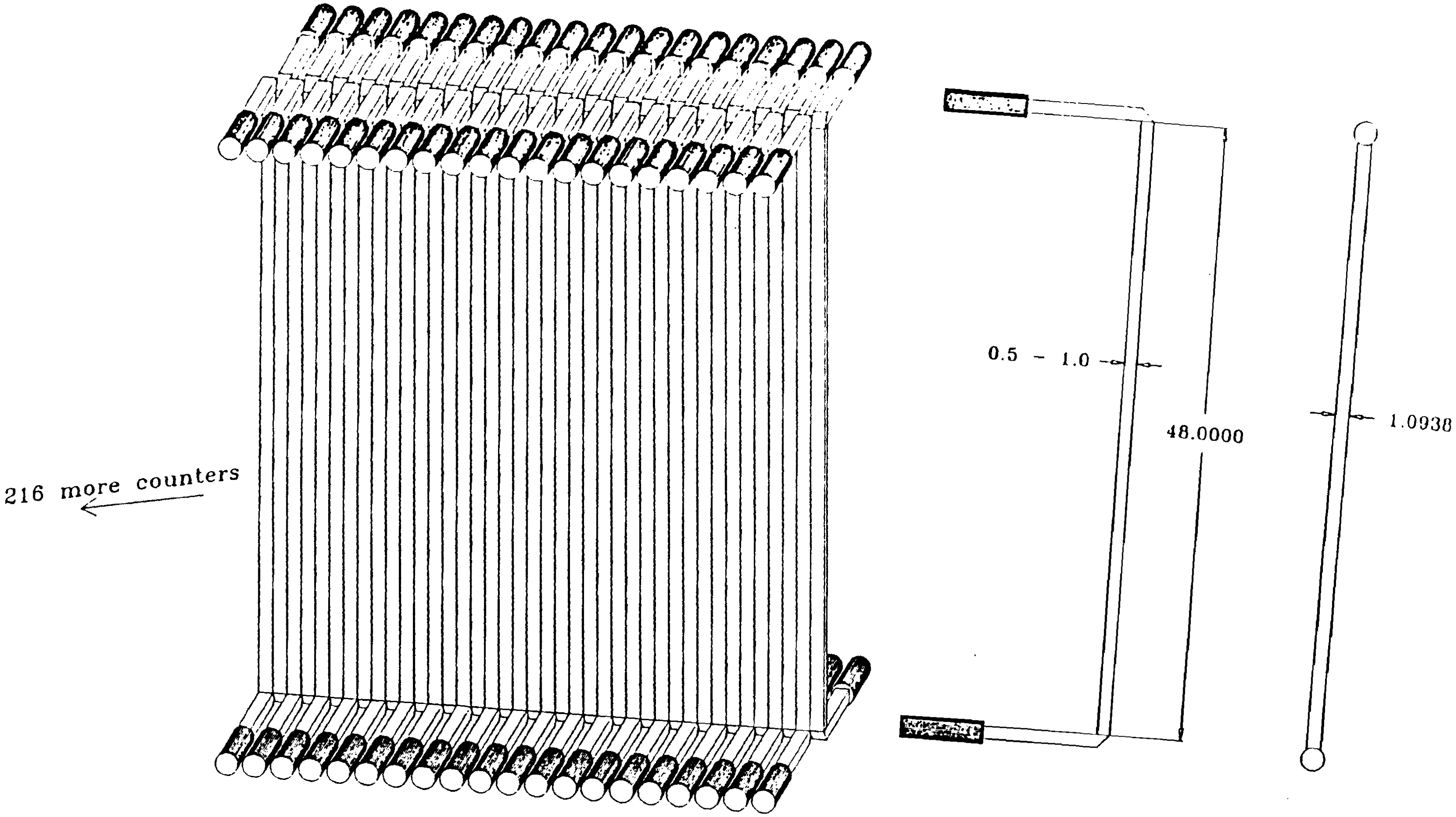

Figure 8: Detail of part of first hodoscope array. (Dimensions are in cm.)

we find that the pattern recognition is simplified due to the three-dimensional space point information. We also find that once a track is found in the scintillators there is a high probability that it will be confirmed in the other detectors.

The granularity of the hodoscope arrays is chosen to minimize losses due to multiple hits in a single counter. We note that our Monte Carlo studies show there is an optimum granularity. If the arrays are too coarse then many tracks are lost because of multiple tracks hitting a single counter. If the arrays are very fine, many tracks are lost because of a track crossing between two adjacent counters in an array and giving incorrect pulse height information and poor timing information in either counter. We have rotated the hodoscope arrays about the vertical so that they are perpendicular to the average trajectory so as to minimize this loss. Although the density of particles across the arrays is not uniform, we plan to run with several different magnetic field settings in the spectrometer which puts the peak density at several different places in the arrays. Our Monte Carlo studies do not show any significant gain by varying the counter sizes across an array, which would also lead to some added complexity of fabrication.

The thickness of the hodoscope counters will be approximately 1 cm, but it would be desirable to minimize this consistent with adequate timing and pulse height resolution. A further complication is the limited space available on the side of the arrays nearest the beam because of the vacuum chamber. This will probably necessitate using nearly right angle light pipes at this end of each counter. An aluminized surface will give a small loss of light, but should not affect the performance of the counters. R&D on the design of the scintillators to study these questions as well as aiding in selection of material and phototubes is under way and will be described below.

In our design calculations we have assumed it is realistic to achieve 0.2 ns RMS timing resolution in the longest hodoscope scintillators (H3 is 0.88m). We note that E802 has obtained 0.075 ns in a basically similar hodoscope [55]. Our test results, which are summarized later in this document, also indicate that this performance is achievable. The vertical resolution of the hodoscope counters is important for pattern recognition and helps in rejecting background. The vertical resolution we expect from the timing difference between the top and bottom tubes is 2.6 cm RMS. This is consistent with experience in E814 where the timing resolution was 0.4 ns and the vertical position resolution was about 5 cm RMS.

The spacing of the hodoscope planes has been set to give a significant measurement of the time lag, relative to $v = c$ particle, between successive planes. For central gold on lead collisions the center of mass rapidity is 1.59 (for gold beam ions with 11.7 GeV/c per nucleon). This gives a time lag in the 4.0 m between H1 and H2 of

Table 7: Dimensions and Locations of Straw Tubes Planes.

Array	Number of chan.	Longitudinal Position (0m=target)	Nearest edge to neutral line (vertical)	Size (vert. x horiz.)	Tube diam.
S1	1920	6.0m	0.0975m	0.225 x 1.28m	4 mm
S2	3510	10.0m	0.1422m	0.416 x 2.34m	4 mm
S3	3858	20.0m	0.2900m	0.820 x 5.13m	8 mm

1.16 ns or about 6 standard deviations. For a rapidity of 2.5, the time lag between planes is .181 ns, about one standard deviation. The time lag from the target to the first hodoscope is 3.0 times this, the time lag from the first hodoscope to the third hodoscope is 2.5 times, and the time lag from the target to the calorimeter is 6.9 times greater. Thus the system will work effectively for rapidities up to about 1.0 above the center of mass rapidity.

To avoid being confused by albedo from particles hitting the calorimeter, the slowest particles of interest traversing the system determine the spacing between the calorimeter and the third hodoscope. We have chosen a spacing of 5.5 m which corresponds to a round trip flight time for a $v = c$ particle of 36.7 ns. This is to be compared with a transit time from the target to H3 of 36.5 ns for a particle with rapidity of 0.806, which corresponds to 0.5 below the center of mass rapidity of a collision of a beam iodine ion (12.2 GeV/c per nucleon) with a lead target (the slowest center of mass system likely to be used).

3.2.3 Straw Tube Plane Design Considerations

The deployment of the straw tube arrays is shown in Fig. 5 and the sizes and locations of each array are given in Table 7. Each array contains six planes, two with vertical wires, two with wires at $+20^o$ to vertical and two with wires at -20^o to vertical. The first two arrays will use 4 mm diameter tubes and do not require any timing information. The last array can use 8 mm tubes and crude timing information (to approximate the resolution of 4 mm tubes with no timing information). The tube sizes are chosen based on considerations of maximum drift times and occupancy.

The choice of straw tubes over other types of wire tracking chambers is motivated by several considerations. Straw tubes are one of the fastest gas detectors [56, 57] when an appropriate gas is used. Although the amount of material in the particle path is somewhat more than an equivalent PWC or drift chamber array, the downstream system already has scintillation counter arrays whose thickness considerably exceeds that of a straw tube array. For the upstream array (S1), either the chamber must withstand vacuum or one must put in a break in the vacuum chamber. Either option for a conventional PWC or drift chamber adds considerable material in the particle path. Since straw tubes have been demonstrated to operate at three atmospheres overpressure, we believe S1 can be placed inside the vacuum chamber. The straw tubes have the additional advantage that the straws largely support the wire tension so that no large frame is required. This is particularly important on the side of the chambers nearest the beam where a conventional PWC or drift chamber frame would not fit.

The straw tubes perform several functions. The downstream arrays (S2,S3) confirm the charged tracks found in the scintillator hodoscopes and provide greatly improved vertical resolution for pointing back to the target. They also provide increased horizontal resolution which translates into increased mass resolution. All of these help in rejecting background. For example, Fig. 9 shows a mass spectrum for a singly charged 12 GeV particle reconstructed using only the hodoscope arrays. Figure 10 shows the same spectrum using the straw tubes as well. Using the straw tubes, the mass resolution ($\Delta M/M$ RMS) is 3.2% or better for all states studied in our Monte Carlo simulations.

The upstream chamber (S1) plays a key role in rejecting background for high mass charge 1 states due to interactions in S1, S2, and the vacuum window. We have found a major source of background which can fake a centrally produced high mass state is due to interactions in the first detector(s). Typically a central rapidity neutron interacts in the first detector producing a forward proton. The proton then has the center-of-mass velocity, and since it came from a similar velocity neutron it tracks back in time to the interaction at the target. Since the momentum is reconstructed assuming the track originated in the target, the track will appear to have a high rigidity and thus a high mass because it was not bent by the first magnet. These events can be rejected by using the calorimeter because insufficient energy is deposited to confirm the apparent high rigidity. However, at some level overlapping particles in the calorimeter combined with upward fluctuations in the energy measurement in the calorimeter can conspire with this type of background to fake a high mass particle. If the track in question did not come from the target, however, it will not reconstruct to a valid point in straw tube array S1. Thus, by giving a second check on the momentum, S1 adds significant further background rejection. A high mass background event can now occur only if all of the following occur in the same event:

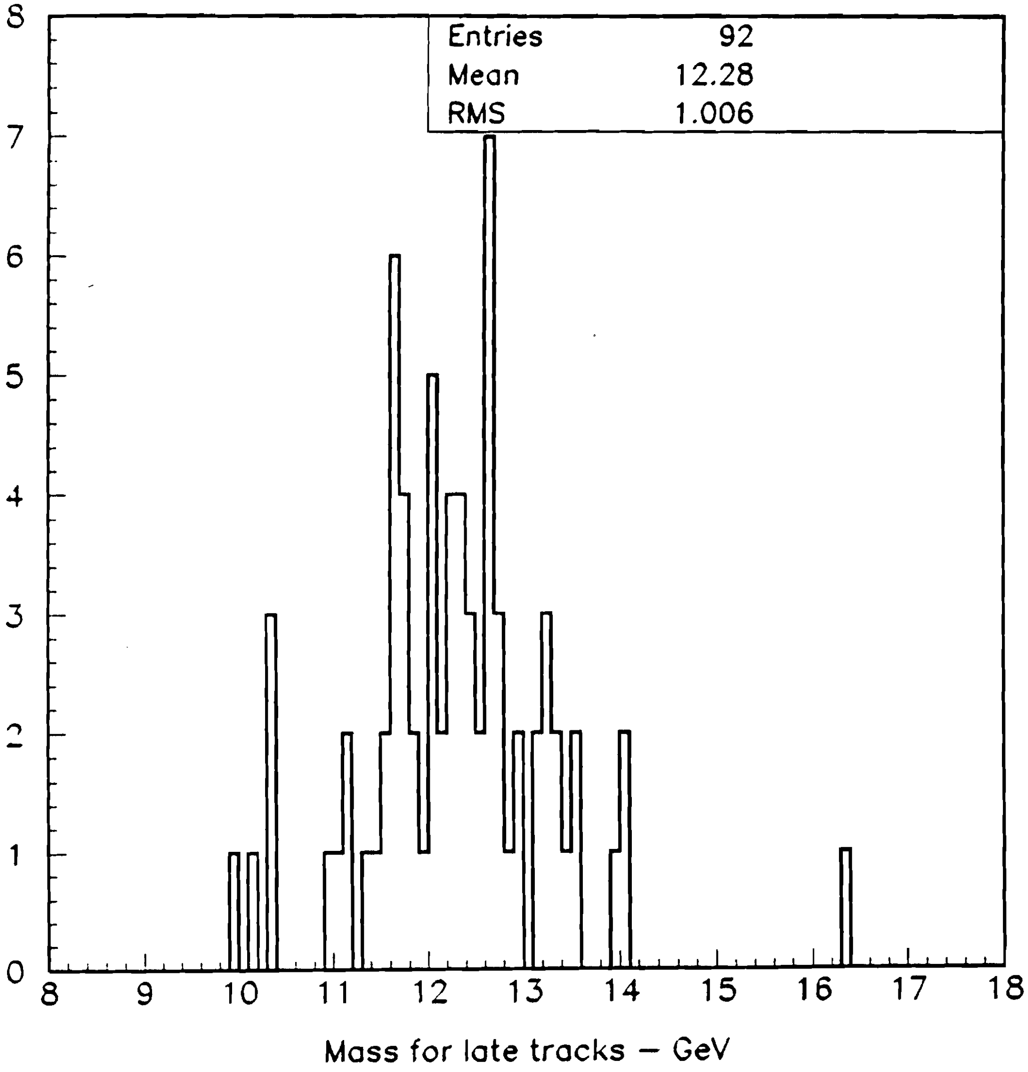

Figure 9: Mass spectrum for singly charged 12 GeV particle reconstructed using time of flight and momentum measured using only the hodoscope arrays.

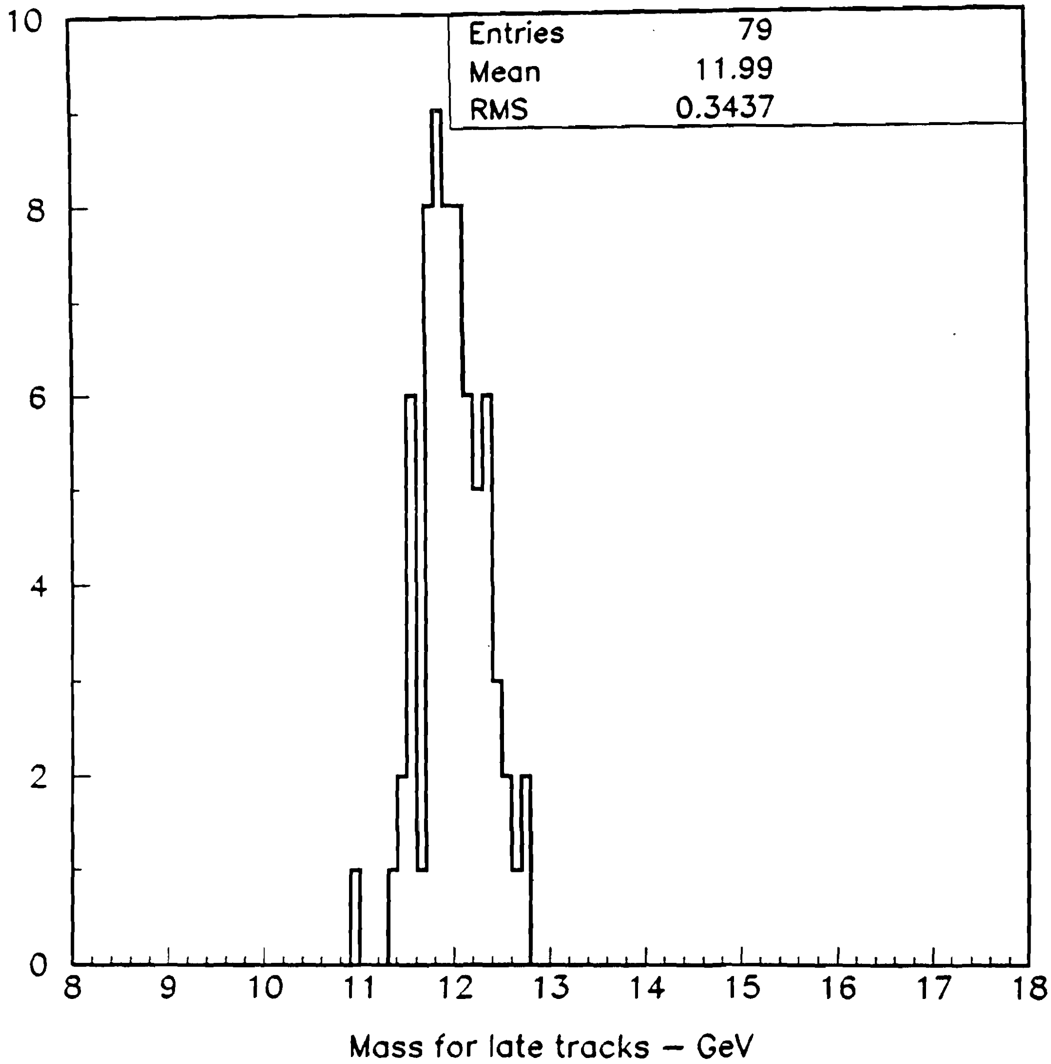

Figure 10: Mass spectrum for singly charged 12 GeV particle reconstructed using time of flight and momentum measured using the hodoscope arrays and the downstream straw tube planes.

- a central rapidity neutron interacts in S1, S2, or the vacuum window and sends a proton in the right direction to look like a high rigidity particle from the target;
- the candidate track overlaps in the calorimeter with other undetected (neutral) particles to produce the correct apparent energy in the calorimeter in the correct place and time (the calorimeter will have time of flight information);
- the candidate track, when extrapolated back to S1 using the apparent high rigidity, points to a good (accidental) hit in S1.

As will be discussed below, our Monte Carlo studies show that the probability of such a multiple overlap is well below the desired sensitivity.

3.2.4 Calorimeter

We propose to use the "longitudinal spaghetti design" which consists of scintillating fibers in a lead matrix, oriented so that the fibers are approximately along the beam direction. We propose an array of modules each 10cm x 10cm by 1m long (5.3 interaction lengths). The array will be 1.3m vertical by 7.2m horizontal. This will cover the active area of the upstream detectors plus allowing a one-module "catcher" layer on all sides. Each module will have an ADC, a TDC, and, for the 770 modules in the fiducial region, instrumentation for the "late energy trigger" discussed below.

The longitudinal fiber calorimeter, which has been invented for proposed experiments at the SSC and LHC high energy colliders, has many advantages over older designs. As Wigmans has shown, it is possible to have a compensated calorimeter with lead and scintillator instead of expensive uranium and scintillator [58]. The use of scintillating fibers rather than scintillating plates and wave shifters to transmit the light to the phototube promises subnanosecond timing performance. Additionally a virtually seamless tower geometry calorimeter can be constructed. There are no cracks for wavelength shifter, light pipes, PMT's, etc. This is especially valuable in an experiment where high sensitivity is sought since even rare background processes involving cracks may be important.

A number of groups are involved in the development of these calorimeters for high energy collider and other applications. We have benefited from discussions with some of these [59, 60, 58, 12] and are continuing to learn more about the work which has been done and is ongoing.

The expected energy resolution of the E864 calorimeter is $.30/\sqrt{E}$ – $.40/\sqrt{E}$. The timing accuracy of the calorimeter is crucial for experiments searching for neutral objects, but is less critical for the charged particle measurements and searches. However, the availability of timing information is still very useful in achieving good background rejection for the charged particle searches. We believe that the longitudinal spaghetti design is capable of subnanosecond resolution [58] and we have assumed in the discussion of the trigger system that the time resolution is as good as 0.5 ns. It may well be that better time resolution is possible. This would be useful although not essential for off line rejection of background events.

The simulations we have carried out and the expected rejection of the calorimeter for background, as well as the R&D and prototype status and plans are discussed below.

3.3 Trigger and Data Acquisition

The purpose of the trigger in the proposed experiment is to reduce the data rate to an acceptable level for the data acquisition (DA) system to record. This means that the necessary trigger rejection is coupled to the performance of the DA system. We have used our experience in Brookhaven experiment E814 and Fermilab E791 as well as Monte Carlo simulations to develop our trigger and data acquisition design.

Because the average central event contains several rapidity central neutrons and protons within our acceptance it is difficult to devise a selective trigger for centrally produced particles whose calorimetric energy deposition is less than about 5 GeV. On the other hand, the greatest requirements for sensitivity occur for systems which do deposit sufficient energy in the calorimeter to allow a selective trigger. These include strangelet searches and antimatter measurements except for $\bar{p}$.

These considerations have led us to choose a combination trigger and DA system which provides more than adequate sensitivity in a minimum bias trigger for the low energy deposit systems, and the maximum sensitivity for the high energy deposit systems with a trigger incorporating late energy deposits. These are referred to as the multiplicity trigger and the late energy trigger, respectively.

3.3.1 Multiplicity Trigger

This trigger will require a signal from the multiplicity array near the target which indicates that the event was within the most central 10% of all interactions. It will also provide the time strobe for the DA system and signals from the same counters with lower thresholds will be used to help detect second interactions within our time window. As discussed above, for low mass states the multiplicity trigger will be the only requirement. With a beam of 10^7 ions per pulse and a 10% interaction length target, such triggers occur at a rate of 10^5 per second. The DA system described below is based on the system used in Fermilab E791 and will be capable of recording 4000 events per AGS spill with 20% deadtime. Clearly, for runs using only the multiplicity trigger, the beam intensity and/or target length can be reduced.

The sensitivity of such running is substantial. For example, in a 100 hour run, assuming an AGS duty cycle of 0.2, 2.88×10^8 events will be recorded. For almost all the processes of interest the acceptance of the E864 apparatus is between 10% and 20%, so that the one event level sensitivity is between 1.7×10^{-8} and 3.5×10^{-8} per central event. These sensitivities are substantial on the scale of the expected yields. For example, H^0 dibaryon yields have been estimated as 10^{-2} to 10^{-3} per central event for Si-Au collisions. [42, 43] The production rate is expected to be even higher in Au-Au collisions.

3.3.2 Late Energy Trigger

For the rarest events it is not possible to reach the desired level of sensitivity without a more selective trigger. In our experiment the observation of late energy deposition in the calorimeter provides a powerful trigger element if the threshold on the deposited energy is sufficiently large. Fortunately, this is the case for the rarest events of interest (strangelets, $\bar{d}$, $\bar{t}$, and the heavier nuclear systems). Here late refers to a time of flight longer by at least 2.5 ns at the calorimeter relative to a velocity of light particle. This corresponds to a rapidity cutoff of 2.16 or 0.57 above the center of mass rapidity.

A complete GEANT simulation of central Au-Au collisions at 11.7 Gev/c per nucleon from HIJET shows that no particles in 500 events deposited more than 3.9 GeV in the calorimeter. The mean number of late particles is 6.9 per central event. The distribution across the calorimeter is nearly uniform. Figure 11 shows the the spatial distribution at the calorimeter of all the late hits in 100 central events. Figure 12 shows the distribution of deposited energies for late tracks for 100 central events. In the figure there is one histogram entry per track.

The simplest way to implement the late energy trigger is to require at least one calorimeter tower to have an energy greater than some minimum and a late time. If we were to work with analog sums of 9 tower groups, which would do a better job of estimating the total energy deposit of the late particle, we would have a serious problem of inefficiency due to vetoing by prompt energy leaking into the group. We have chosen a threshold for the timing discriminator of 0.33 GeV and an energy threshold of 3.3 GeV in a single tower. Using the GEANT/HIJET distributions and the average shape for the spatial distributions of hadronic showers in the SPACAL

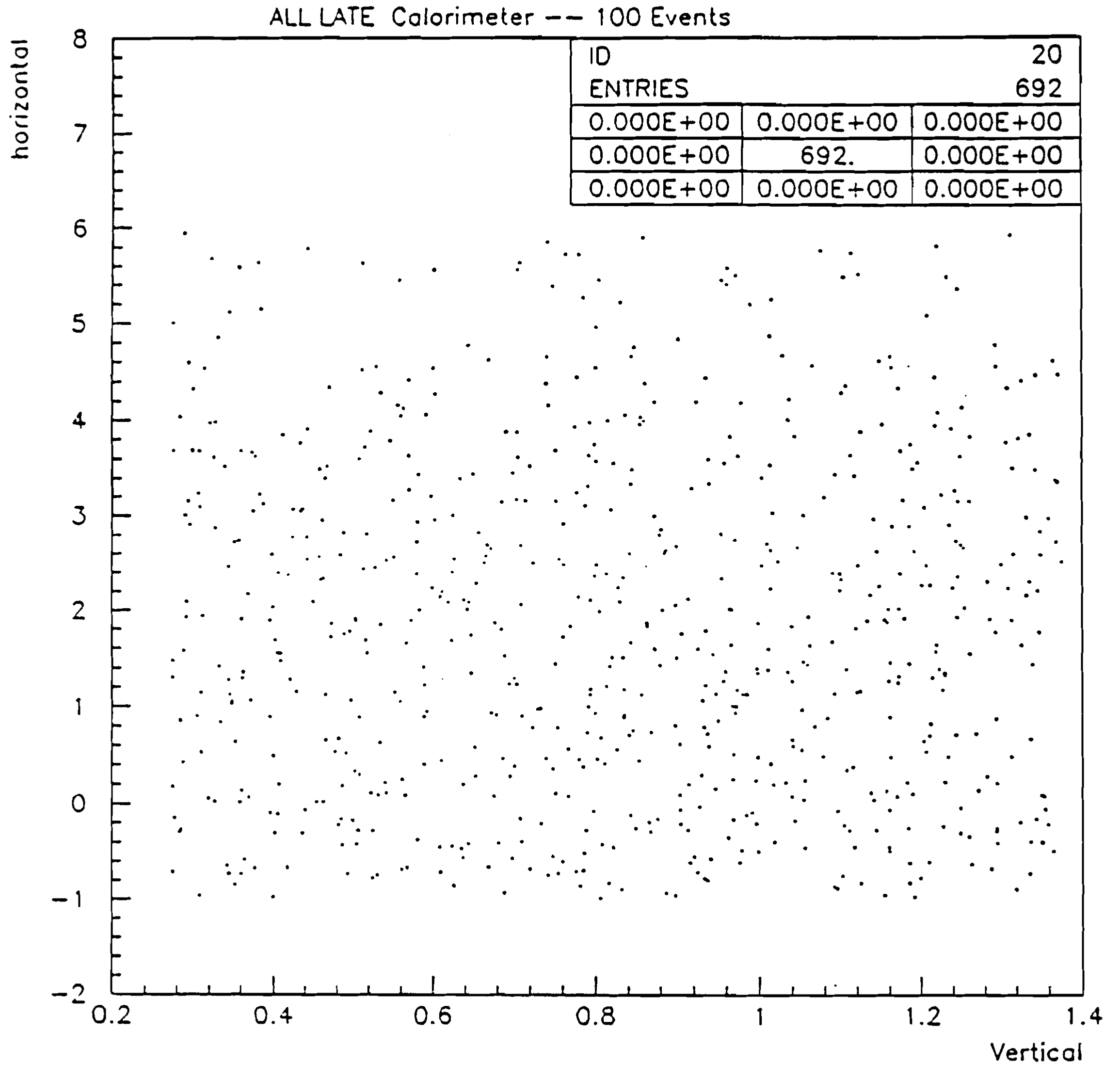

Figure 11: The spatial distribution of late hits in the calorimeter for 100 events. (Scales are in meters.)

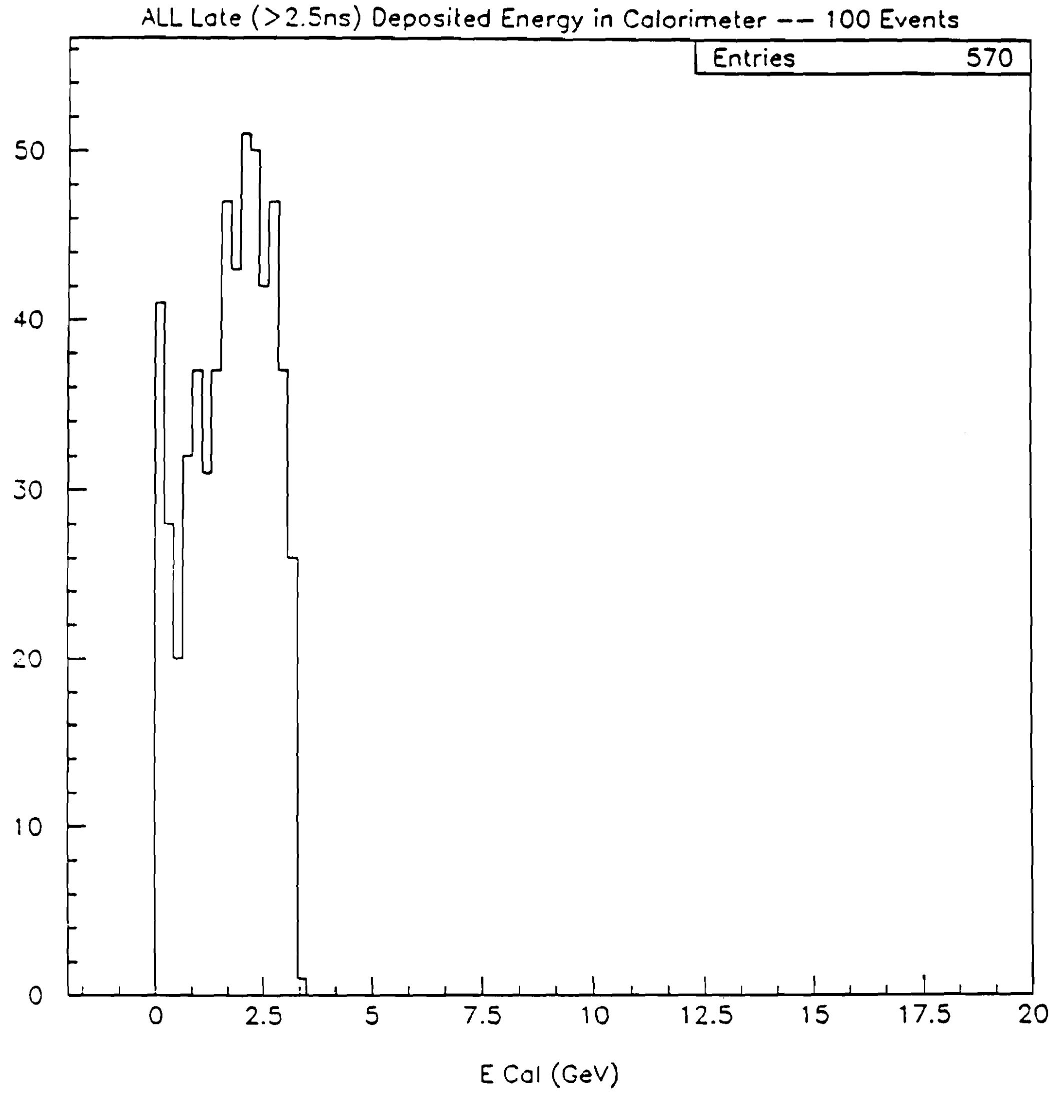

Figure 12: Distribution of energies for late tracks for 100 central events. There is one histogram entry per track.

prototype [61], we have estimated that the false trigger rate is less than 1% per central event. The late trigger efficiency is included in the shower finding efficiency calculated in the section on calorimeter analysis.

It is known that HIJET does not produce nuclear fragments, so an additional study was carried out to calculate the effect of centrally produced deuterons on the late energy trigger. A coalescence estimate of central deuteron production was made and the acceptance of the spectrometer and the late energy trigger for these deuterons calculated using GEANT and CALSIM to simulate the showers in the calorimeter. From this estimate we conclude that 0.34 central deuterons per event could pass a late energy trigger with a simple threshold requirement of 3.3 GeV in the late tower. Figure 13 shows the energy in the peak tower in a shower vs. arrival time of the particle at the calorimeter for a 10 GeV strangelet and for centrally produced deuterons. The width of the bands includes shower fluctuations as well as position variation across a tower. The bands are clearly separated, but there is no single energy cut which will cleanly discriminate between them. A "conceptual" circuit, which is essentially a discriminator with a time varying threshold, is also shown in Fig. 13. The line between the bands is the threshold curve for such a circuit with the constants shown. By using these discriminators on the calorimeter we can cleanly reject low mass states while maintaining high efficiency for high masses.

Finally, it should be noted that the late energy trigger will include the multiplicity requirement from the counters near the target.

With these requirements, the late energy trigger will provide at least an additional trigger rejection factor of 100. A factor of 50 is needed to achieve the desired sensitivities.

3.3.3 Data Acquisition System

As discussed above, the difficulty of making a low mass trigger due to the presence of central neutrons and protons in the apparatus makes it desirable to have a data acquisition (DA) system capable of recording about 4000 events per spill. To achieve this we have considered a system similar to but smaller than the one used in Fermilab E791 [62].

The Fermilab system is capable of acquiring data at a rate of 25Mb/sec during the beam spill and recording data at an average rate of 10Mb/sec continuously. To acquire 4000 events per spill in the proposed experiment we need to acquire data at 16Mb/sec during the spill and record at an average rate of 4Mb/sec. The lower data rate and the much shorter accelerator cycle (4 sec vs 60 sec) means we can use a small part of the Fermilab 791 system to achieve the desired rate.

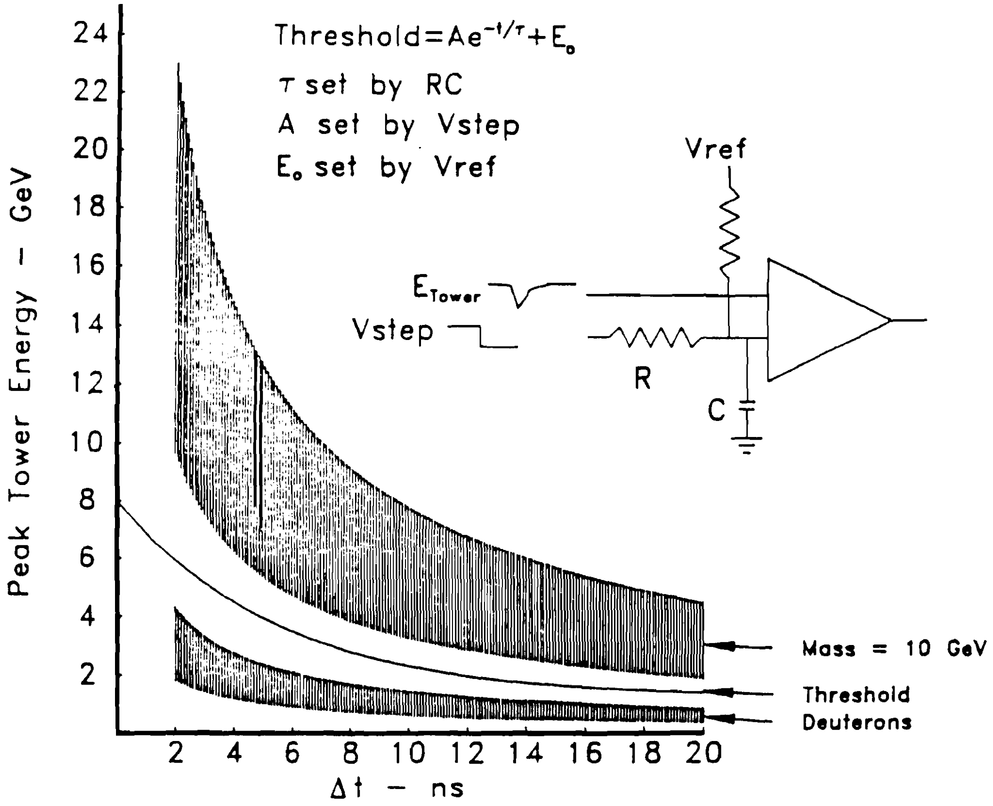

Figure 13: Energy in the peak tower in a shower vs. arrival time of the particle at the calorimeter for a 10 GeV strangelet and for centrally produced deuterons.

The advantages of this system are:

- high data rate
- easily expandable
- easy to add Level III processing for trigger, monitoring, or data formatting and compression
- excellent failure rollover characteristics
- relatively low cost.

The use of such a system will allow a relatively open trigger to be used for the low mass states. This has the additional advantage of providing a large minimum bias data sample. The parallelism of the system has the additional advantage that the failure of a single component usually will still allow data taking to continue with a slightly reduced throughput.

We will give the details of the Fermilab system below, however specific implementation may change as the technology continues to evolve. The system described below is currently in use and therefore we have firm numbers for both performance and cost.

3.3.3.1 Details of the DA system Data from the digitizers (ADC's, TDC's) are read out into event FIFO buffers(EFB) through as many parallel paths as needed to achieve the required throughput (see Fig. 14). The CAMAC and FASTBUS crates are read out through Fermilab SCC's (smart CAMAC controller) and FSCC's (FASTBUS smart crate controllers). The CAMAC controller is currently available commercially and it is expected that the FASTBUS controller will also be produced commercially. These controllers have a Motorola 68000 series processor and local memory. They are programed to execute the required series of CAMAC (FASTBUS) commands to read and clear modules in the crate and transfer the data out through a front panel connector to the EFB in response to a trigger signal. The output can be daisy chained so that several crates can be read into one EFB.

The EFB's contain event fragments which must then be assembled into events. This is done by ACP-I processors in VME crates. A simple interface card (Event Buffer Interface or EBI) connects the EFB's to the ACP's through the VME back plane. Enough ACP's are used in each crate to accomplish the required processing at the desired rate. In each crate, one processor acts as a "boss" and directs the actions of the other processors. The other processors are either reading data from the EFB's, processing the data (formatting, checking for readout errors, etc.) or waiting. The boss processors and the pass through logic in the EBI's cause the VME crates to act like a barrel switch so that each crate is always reading from an EFB, and in a given crate, the ACP that is currently gathering data scans from one EFB to the next to pick up all the fragments of a given event.

Once a given processor has formatted a block of data (typically several events), it notifies the boss processor which notifies the tape controller (MTC). The tape controllers are commercial units (Ciprico) which have scatter/gather capability and can interface up to 4 Exabyte 8mm drives each. The required recording speed is achieved by running drives in parallel.

The ACP processors not only format the data, but also check for errors, maintain and report error summaries and build requested occupancy and frequency histograms. They also could be programmed to do Level III trigger calculations.

An additional module in each VME crate (BVI) provides an interface to the host computer. (For Fermilab E791 a VAX 11/780 is used. Any processor which can communicate with the VME crates can be used as a host.) The host computer downloads the ACP programs and all user requests for histograms and error reports and receives the reports and histograms back from the processors. A final module in each crate (VRM) provides a visual display for crate monitoring. The host computer also communicates with the SCC's and FSCC's via an ether net link.

The full Fermilab system has 6 VME crates. The front end architecture and two of the VME crates are shown in Fig. 14. For the required performance in E864, only two VME crates with the hatched modules in Fig. 14 are needed.

3.3.3.2 Cost of DA system. Since the system shown in Fig. 14 is fully operational at Fermilab, we have complete cost information. The costs of the various components are listed in Table 8. The cost of the CAMAC and FASTBUS controllers are included with the cost of the crates in the experiment cost summary.

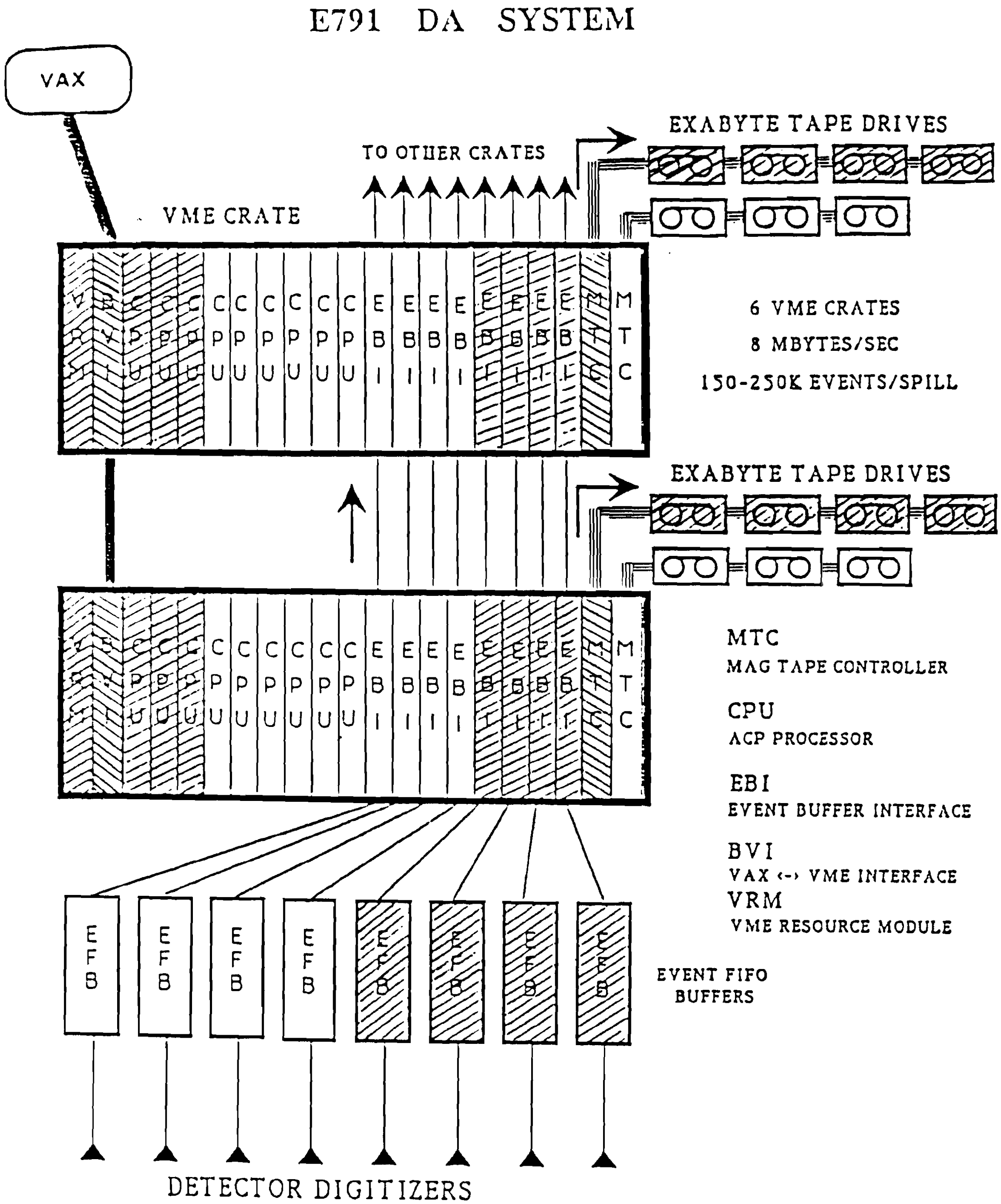

Figure 14: Fermilab E791 DA System. The hatched modules make a sufficient system for E864 to run at 4000 events per spill.

Table 8: Cost of DA System

Item	Unit Cost	Quantity	Cost
EFB	$3000	4	$12000
EFB Crate	$1500	1	$1500
EFB Monitor	$1200	1	$1200
Powered VME Crate	$1500	2	$3000
VRM	$500	2	$1000
BVI	$1700	2	$3400
ACP-I	$1300	6	$7800
EBI	$300	8	$2400
MTC	$1150	2	$2300
Subtotal			$34300
Exabyte 8mm drives (dual density)	$4500	8	$36000
Spares			$6000
TOTAL			$76300

4 Backgrounds, Efficiencies and Analysis

4.1 Overview

Below we will discuss the various Monte Carlo simulations used to evaluate the efficiency and sensitivity of this experiment. Since one goal of the Monte Carlo effort is to provide a realistic simulation of the response of the various detectors, the output of the Monte Carlo also provides a basis for developing analysis techniques. We discuss our experience in analyzing the Monte Carlo data and results of calculations of other possible backgrounds.

As mentioned earlier, for charged particles the charge +1 systems are the most challenging in terms of achieving the desired sensitivity, hence the discussions of charged particle background below will focus on these states. For neutral particles, the low mass states are most challenging due to background from neutrons. The discussion of the results of calculations and analysis for backgrounds to neutral states will focus on detecting the H^0-dibaryon.

4.2 Monte Carlo Simulations

Since it is impossible to completely simulate running the apparatus at the desired level of sensitivity (i.e. generate and completely track 10^{11} to 10^{12} events) we have concentrated on simulating likely background processes.

Various parts of the simulation are separately generated and the results stored in libraries. Information from the libraries is then combined to make complete events of the type needed to study a particular feature of the experiment. To illustrate the limitations of computing power, Table 9 lists the computing time required for some of the steps described below.

Figure 15 shows the relationship of the various simulations used. The simulations were used for two different areas of study. First, we calculate the acceptance of the apparatus for processes of interest and the efficiency for finding tracks of interest in the presence of the rest of the interaction products, including all secondaries, tertiaries, etc. from decays and interactions in the detectors, collimators, magnet pole tips and other surrounding material. Second, we investigate the level at which various background processes can fake an interesting high mass state. Several paths are used to achieve the desired results.

For general studies of the detector performance, we used two event generators. The package HIJET was used to generate Au-Au collisions at 11.71 GeV/nucleon. A

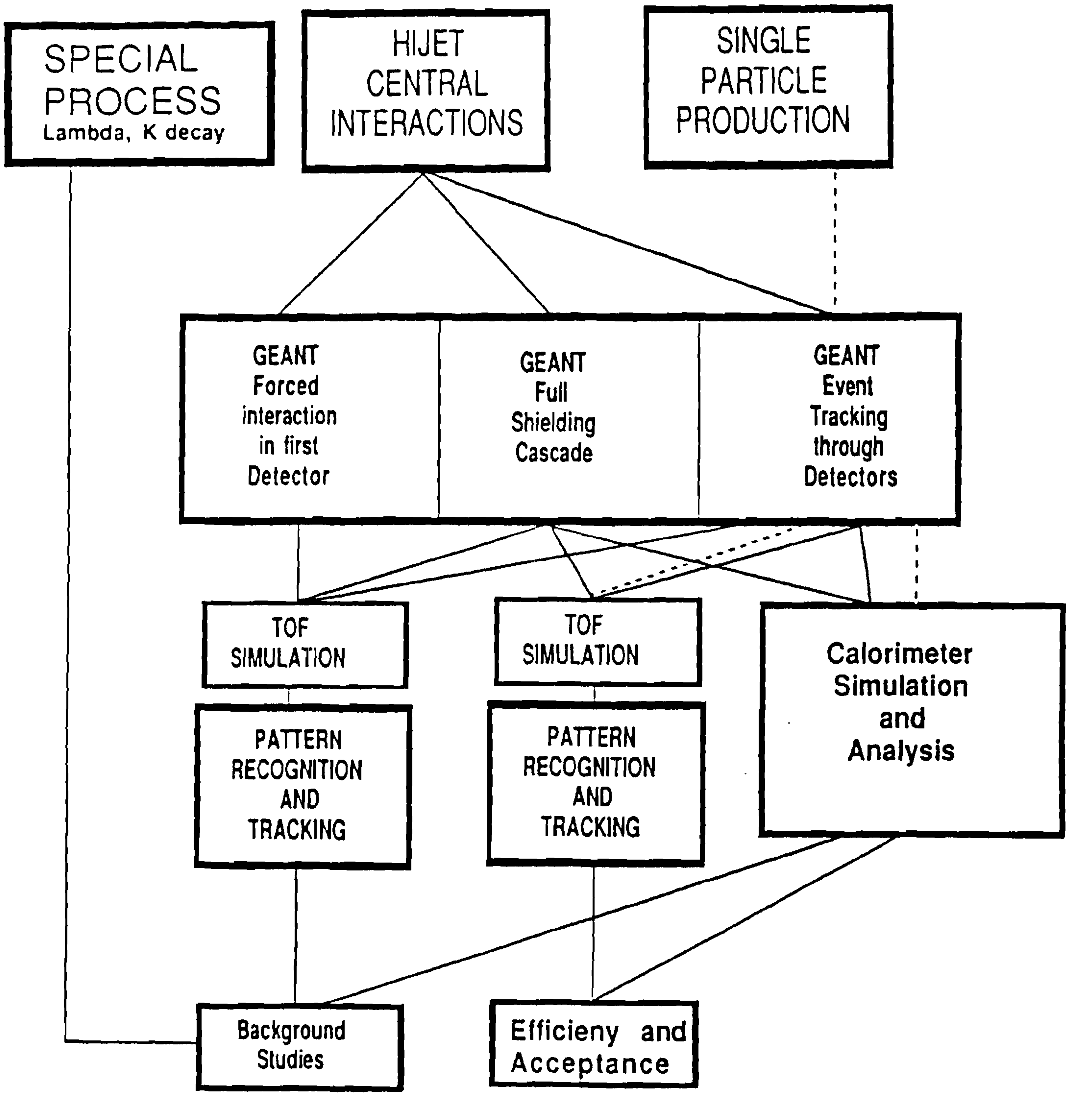

Figure 15: Chart of steps used in Monte Carlo Simulations.

Table 9: Typical computing time required for various Monte Carlo steps (1 VUP-second corresponds to 1 CPU second on a Vax 11/780).

Process	CPU Time
Generate HIJET Central Au-Au collision	100 VUP×second
Track Hijet Central	35 VUP×second
Track Hijet Central with full shielding showers	5400 VUP×second
TOF simulation	20 VUP×second

separate single particle generator, described below, was used to generate various specific states of interest. The particle types and four-vectors for each event were stored in event libraries.

The event libraries were then processed by the CERN package GEANT. GEANT was used for several different types of processing. First, events could have all tracks traced through the detectors with all secondary processes (decays, interactions, etc.) involving detectors and surrounding air included. In this mode, interactions in the magnet iron, collimators and shielding are not simulated. Tracks entering these materials are lost. The detector hits were stored in "hit banks," and grouped together and stored in event hit libraries. Both HIJET (central collision) events and single particle events were processed in this way.

Another library was formed using HIJET events as above, except that tracks entering the the collimators or pole tips were followed through the full shower process. In this library, only hits due to tracks from interactions in the shielding were kept. This "shielding hit" library was generated separately because tracing showers takes a large amount of computer time, so far fewer events of this type could be simulated.

Libraries were also made in which only events were used if a secondary interaction occurred in a specified detector or in the vacuum window and a charged particle from this interaction traversed the rest of the apparatus. Only the hits from the interaction product traversing the rest of the apparatus were saved in the library. This library is used to construct events with enhanced background.

Finally, hit banks from the various libraries were merged to form the desired type of event. For example, to fully simulate a Au-Au collision in which a charge +1, mass 12 exotic was produced, the hit banks for an event from the central collision library, the hit banks from the shielding hits library and the hit banks from the appropriate single particle library are merged. The resulting event is then stored again in another library.

At this point the processing of the Monte Carlo data was separated into two independent paths - one for the tracking system and one for the calorimeter. This reflects the assumption that the efficiencies and background rejection of these detector systems are independent and can be calculated separately.

Two post processors for the GEANT output were used to complete the detector simulation. The program CALSIM was used to make libraries of showers in the calorimeter which were then matched with the impact information from GEANT to form showers in the calorimeter. For the hodoscopes, the energy loss in the hodoscope counters from GEANT (the energy deposition, its position and time for each hit in a counter) was used to simulate the pulse at each phototube and derive a time and pulse height signal. Charged particle hits in the straw tubes were digitized with the appropriate granularity.

Finally, analysis programs were used to analyze the data from the calorimeter or tracking system and the results used to calculate efficiencies or background rejections. Details of the simulations and analysis are given below.

4.2.1 HIJET/GEANT Simulations

As indicated above, we used HIJET to simulate Au-Au interactions. The parameter CENTRA was set to 5 for most of our studies. This selects the central few percent of the cross section, which is expected to correspond to events selected by our multiplicity trigger. In addition, HIJET includes secondary interactions, the nucleon Fermi momentum distribution, and uses a Wood-Saxon nucleon potential. The rescattering parameter was set to 3.25, which reproduces existing AGS multiplicity data.

For single particle production we used the following model:

$$\frac{d^2N}{dydP_t} = aP_te^{-\alpha P_t-(y-y_{cm})^2/2\sigma_y^2}$$

where:

$$\alpha = \frac{2.0}{< P_t >}$$

$$< P_t > = .6\sqrt{A} \; in \; Gev/c$$

$$\sigma_y = .5$$

with cutoffs:

$$\max P_t \;=\; 5 < P_t >$$

$$y \text{ within } y_{cm} \pm 3\sigma_y$$

GEANT is used to track particles produced by either generator through the apparatus. All physics processes were turned on in GEANT; these include Gaussian multiple scattering, decays, hadronic interactions, Compton scattering, pair production, and positron annihilation. Energy loss with Landau fluctuations including δ-ray production is used to compute the energy deposited in the tracking detectors. The arrival time for each energy deposition is also calculated. All interactions in the collimators, magnet pole tips, vacuum chamber walls, etc. were simulated for the shielding hits library. Finally, standard GEANT momentum cutoffs were used. Studies showed that the results did not change if the momentum cutoffs were lowered.

The output from GEANT was stored in the form of "hits banks" for each detector for each event. The hits files have x, y, z, TOF, ΔE for each particle which deposits energy in a detector.

To give a feeling for the nature of the events from the simulation we show a typical event. Figure 16 shows the spectrometer magnets, collimator, part of the vacuum chamber, and the detectors as described in GEANT. In Fig. 17 a typical central Au-Au interaction is shown overlaid on the detector. One can see that interactions in the detectors and air are included. In Fig. 18 tracks from the collimators and other non-detector material are included. One should note that these figures are highly anamorphic - hence the appearance of very wide angle tracks from the shielding is somewhat deceiving. Dotted or dashed lines represent neutral particles and particle trajectories are not drawn inside the magnet iron or shielding. Figure 19 shows the longitudinal origin of all proton and neutron tracks which produced hits in any detector from GEANT tracing a sample of HIJET central Au-Au collisions. (Tracks from shielding interactions are not included in this plot.) There are a total of 3.88 x 10^6 tracks in the histogram. Almost 2/3 of these tracks come from the interaction target. The remaining 1/3 come from decays and interactions in the detectors, vacuum window and air downstream of the vacuum window. All these processes are included in our simulations.

Table 10 gives the average number of hits in the detectors for various types of events. As noted in the section on "Magnets, Collimators and Vacuum Chamber" there is

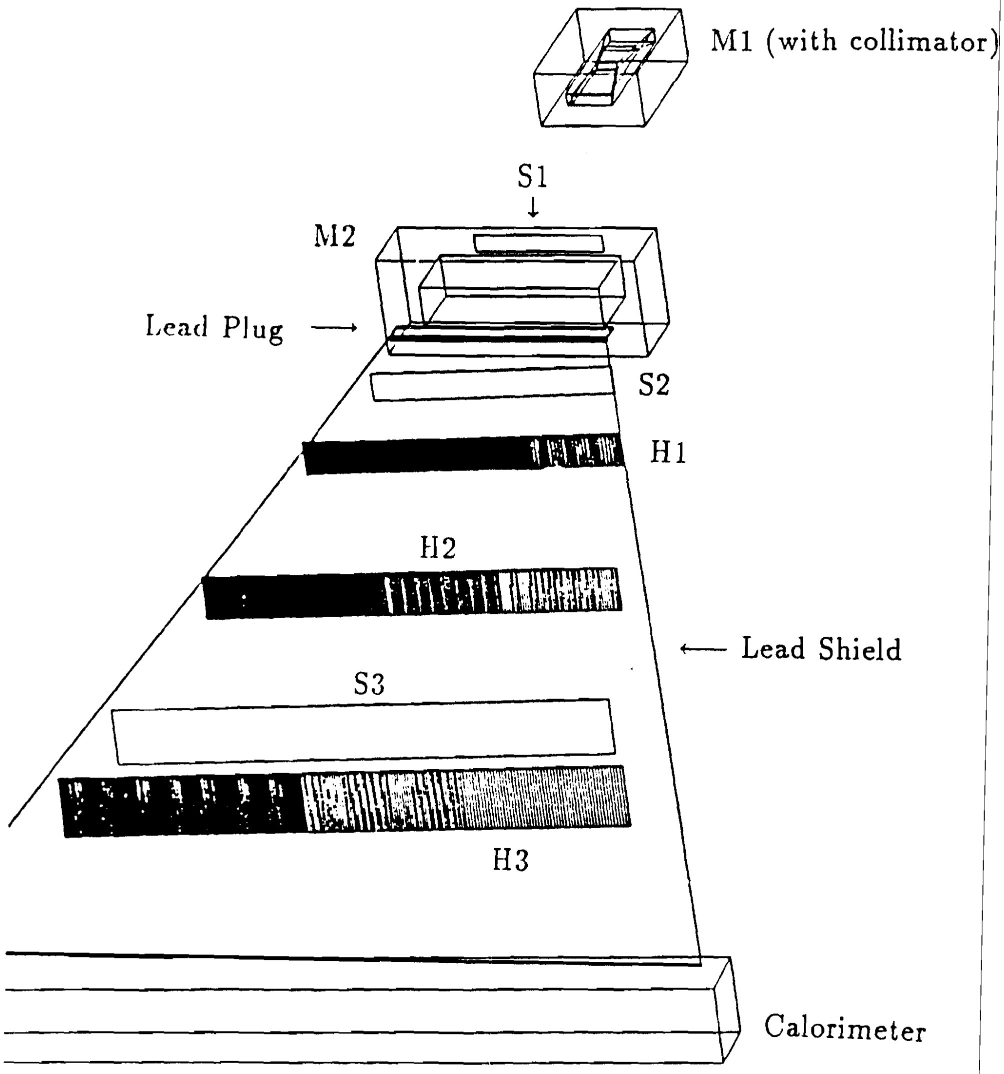

Figure 16: E864 Apparatus as entered into GEANT.

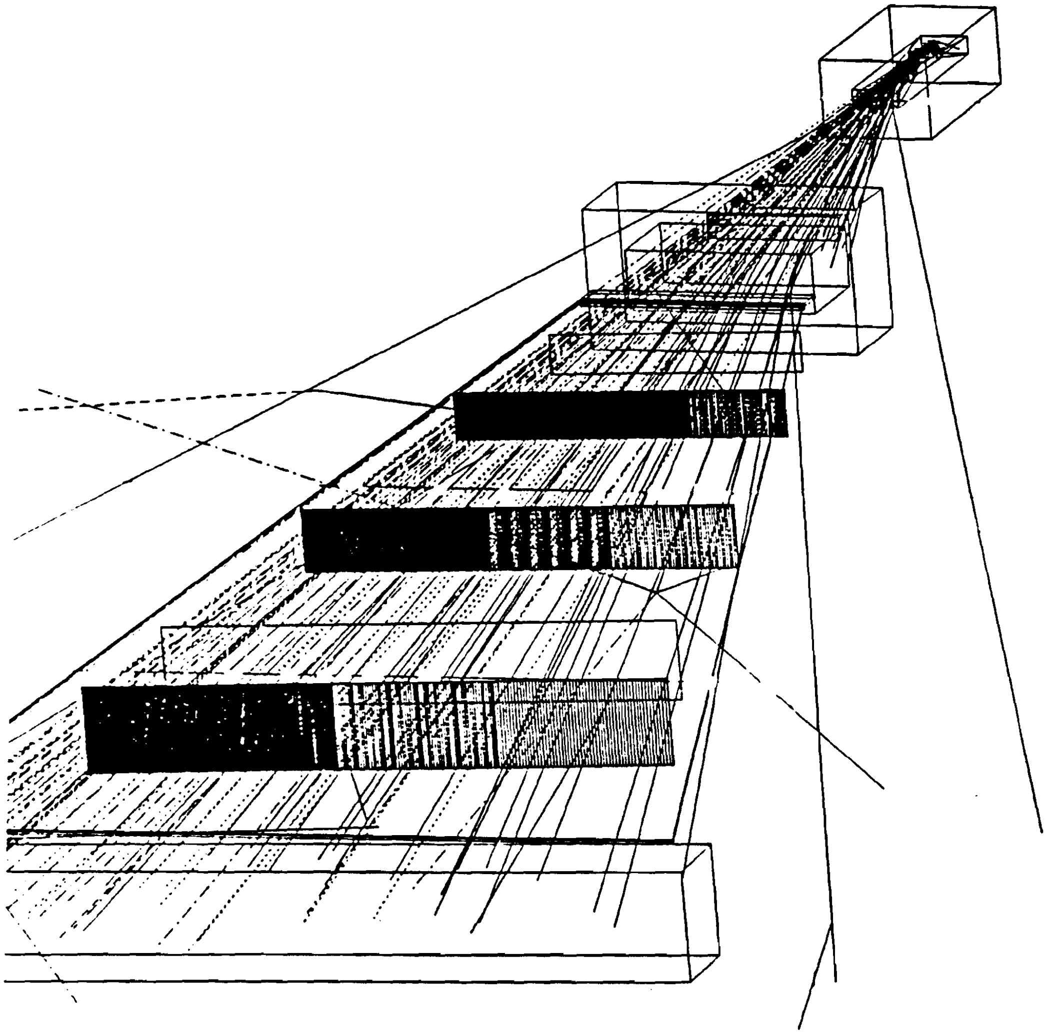

Figure 17: Typical central Au-Au interaction tracked by GEANT through the E864 Apparatus. Dashed or dotted lines are neutral particles.

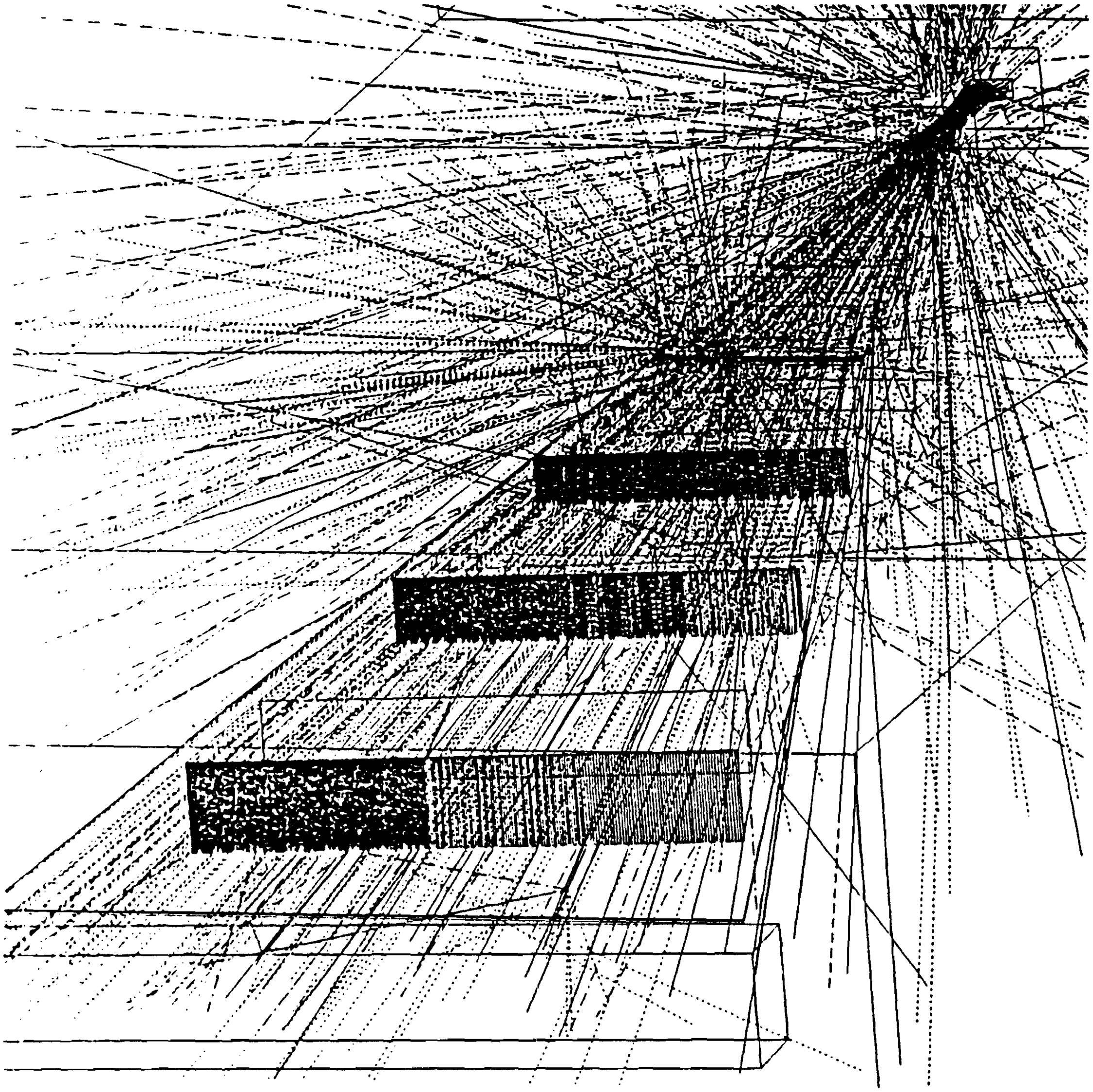

Figure 18: Central Au-Au interaction with tracks from shielding included. Dashed or dotted lines are neutral particles

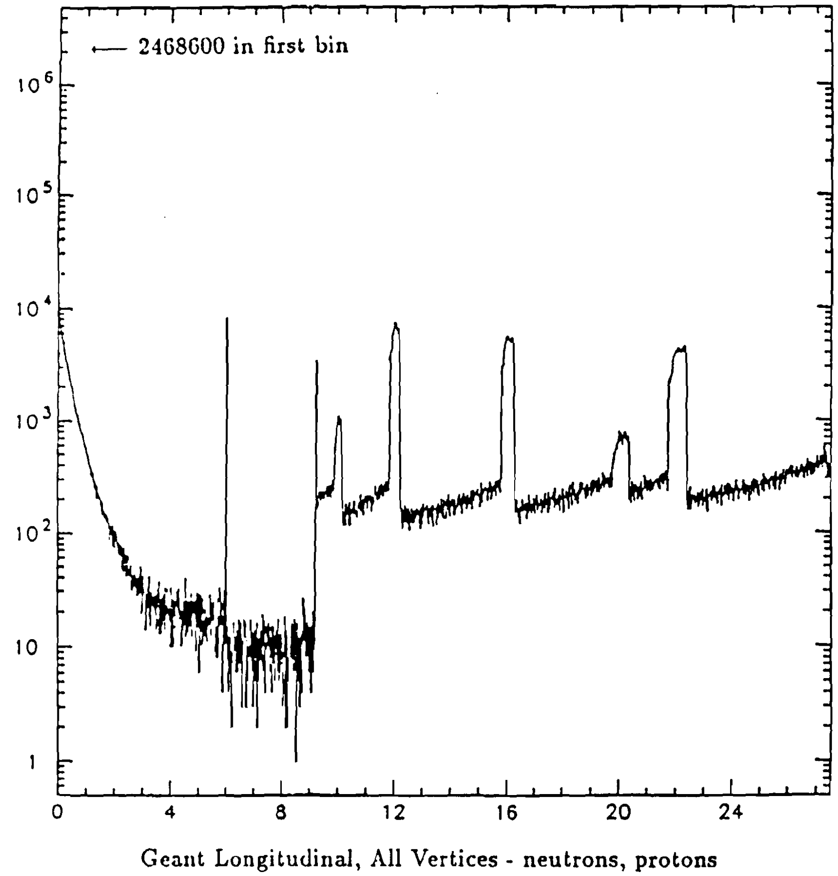

Figure 19: Longitudinal origin of all proton and neutron tracks which produced hits in any detector from GEANT tracing a sample of HIJET central Au-Au collisions. (Horizontal scale is meters from target.)

Table 10: Average hit multiplicities for central events in the E864 detectors with and without extra track from showers in the shielding.(Parentheses show RMS spreads.)

Detector	Central no shower	Central full shower
H1	11.5 (3.8)	14.8 (4.3)
H2	11.0 (3.4)	13.8 (4.4)
H3	11.1 (3.5)	14.5 (4.0)
S1	11.5 (3.3)	11.7 (3.1)
S2	10.5 (3.1)	19.6 (6.2)
S3	10.7 (3.6)	13.3 (4.0)
CAL	48 (7.3)	85 (18)

a significant increase in the number of particles entering the calorimeter (about a factor of 2) due to the interactions in the collimators and shielding, but almost all of the increase is from very low energy photons which should have little effect on the performance of the calorimeter.

4.2.2 Time of Flight Simulation

Incorrectly measured time of flight can result in tracks which are incorrectly assigned a large mass. In particular, any late tail in the resolution function will translate into a high mass tail. To study the time of flight resolution we have written a detailed simulation of the physical processes in the scintillator. This program uses the information from the GEANT hits banks described above to produce a simulated TDC and ADC value for each phototube. The energy loss, time and vertical position of all hits in a given counter are combined using geometry information (location and length of the counter, length of the light pipe) to simulate pulses from the photomultipliers at the top and bottom of each struck counter. A discriminator threshold is applied to get the time for each photomultiplier and the number of photoelectrons is added to get the pulse height. The GEANT hits file is then rewritten with the time and pulse height for each struck phototube included.

The timing is simulated by using each energy deposit in the scintillator to generate photons which are traced in time to the photocathode of the photomultiplier where photoelectrons are produced. Each photoelectron is added into an array which represents 50 psec time slices around the relevant time. After all energy deposits are processed, a transformation is applied to the array to represent dispersion in the photomultiplier and cable. The resulting array is then scanned to find the first crossing of the discriminator threshold. This value is then smeared randomly according to a gaussian to represent noise and other unaccounted effects. The final result is recorded as the TDC value for the photomultiplier. The number of photoelectrons is summed and recorded as the pulse height. We do not smear the pulse height since the width and shape of the pulse height distribution is expected to be totally dominated by Landau fluctuations which are included in the GEANT simulation.

The following processes are used in the simulation:

- A Poisson distribution for the number of photoelectrons. The mean is calculated by normalizing the energy deposit from GEANT to 85 photoelectrons for the average minimum ionizing charge 1 particle at 50cm from the end of the counter. An attenuation length of 110cm is used. This represents about one third the number of photoelectrons expected from a 1cm thick counter.

- Geometric dispersion (Fig. 20). Photon paths are generated randomly in direction and the flight time to the photocathode is calculated and added to the time from GEANT.

- Photon production - a double exponential is used. The first exponential represents the primary (UV) scintillation in the polyvinyltoluene matrix which pumps the fluors. The fluors then decay with a second exponential time constant to give the visible light (see Fig. 21). The time constants used are τ_1=0.5ns and τ_2=1.5ns. These and the attenuation length of 110cm are typical of fast plastic scintillators such as Bicron 418 or Pilot-U.

- Electronics - A double exponential pulse shaping is used to represent the dispersion in the phototube and cable.

- Discriminator - a fixed threshold is applied at about 10% of the average minimum ionizing pulse height.

- Everything else - the discriminator crossing time is randomly smeared according to a gaussian with width of about 220psec. (This is adjusted to give a resolution for the mean time in H3 of 200 psec, which is the design goal.)

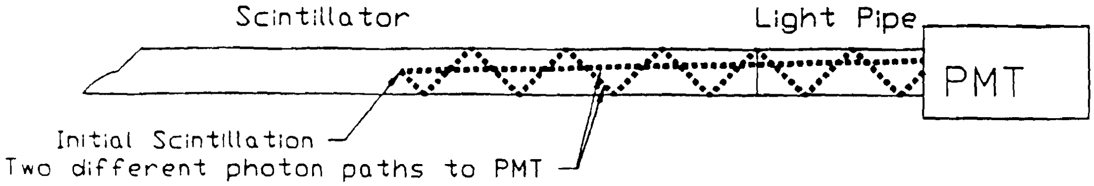

Figure 20: Geometric dispersion of light pulse in scintillation counters. The flight time to the photocathode for each photon is calculated for the time of flight simulation.

Figure 22 shows the simulated pulses for four successive hits in H1. Figure 23 shows a typical distribution of times for 100000 particles striking the center of one counter. The solid curve is the best fit Gaussian. The distribution clearly has a late tail.

4.3 Tracking Analysis of Monte Carlo Data

As discussed above, the GEANT hit banks were treated as data and analyzed to study acceptance, efficiencies and background processes.

4.3.1 Tracking Analysis Pattern Recognition

First, a calibration process was carried out to obtain slewing constants for the scintillator timing. Figure 24 shows the mean time vs pulse height for one of the hodoscopes. A polynomial is fitted to this distribution and used to correct the mean time. The top and bottom photomultiplier times are used to calculate both the mean time and the time difference, which gives the vertical position. The pulse heights are used for the slewing correction and to calculate the geometric mean pulse height, which is normalized to minimum ionizing (charge 1) and then used to assign a charge to the particle causing the hit. The charges are assigned according

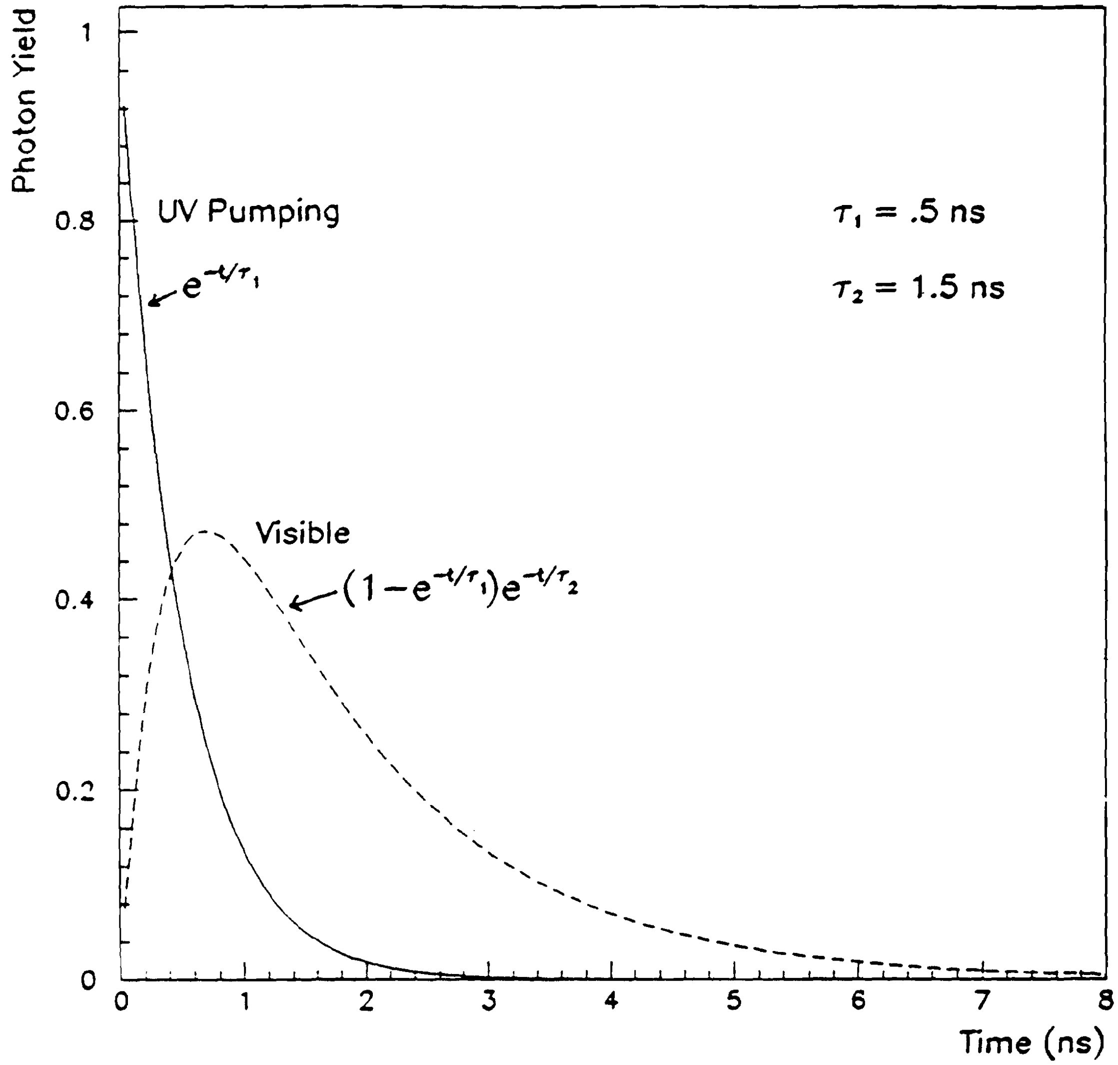

Figure 21: Photon production in the scintillators is taken to be a double exponential.

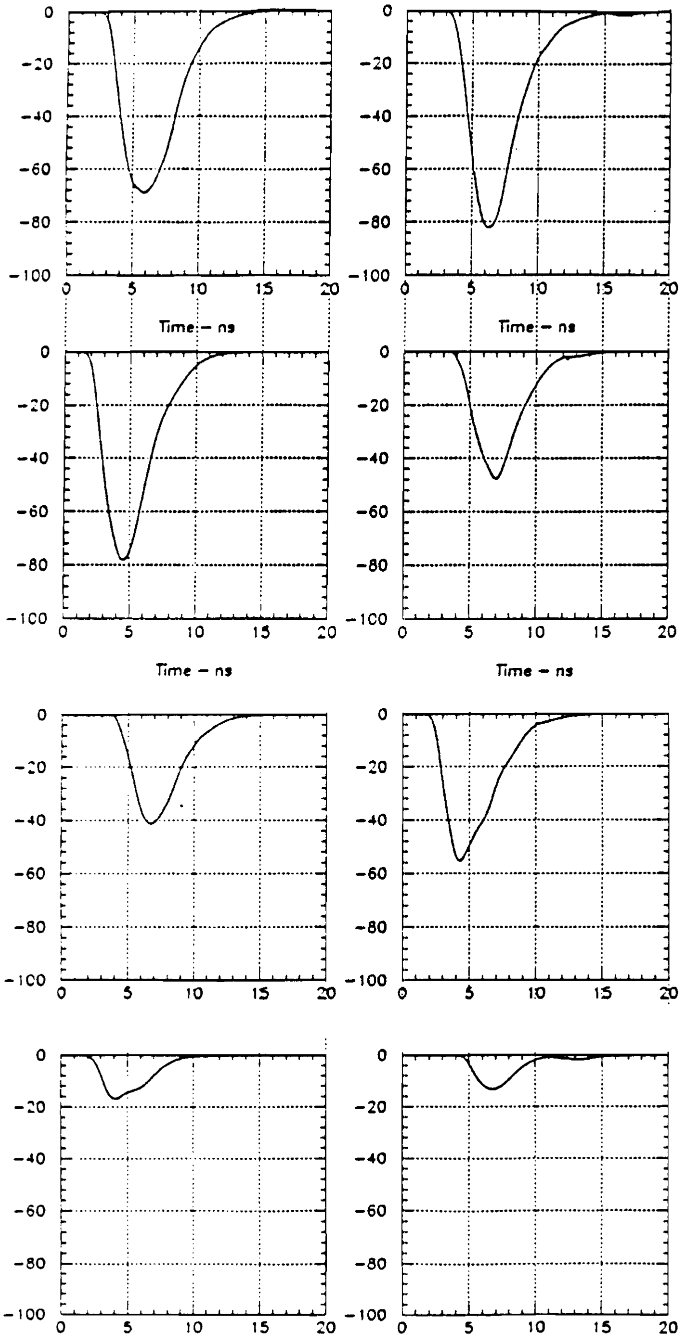

Figure 22: Simulated pulse shapes for four successive hits in H1. The left and right plots are for the top and bottom phototubes.

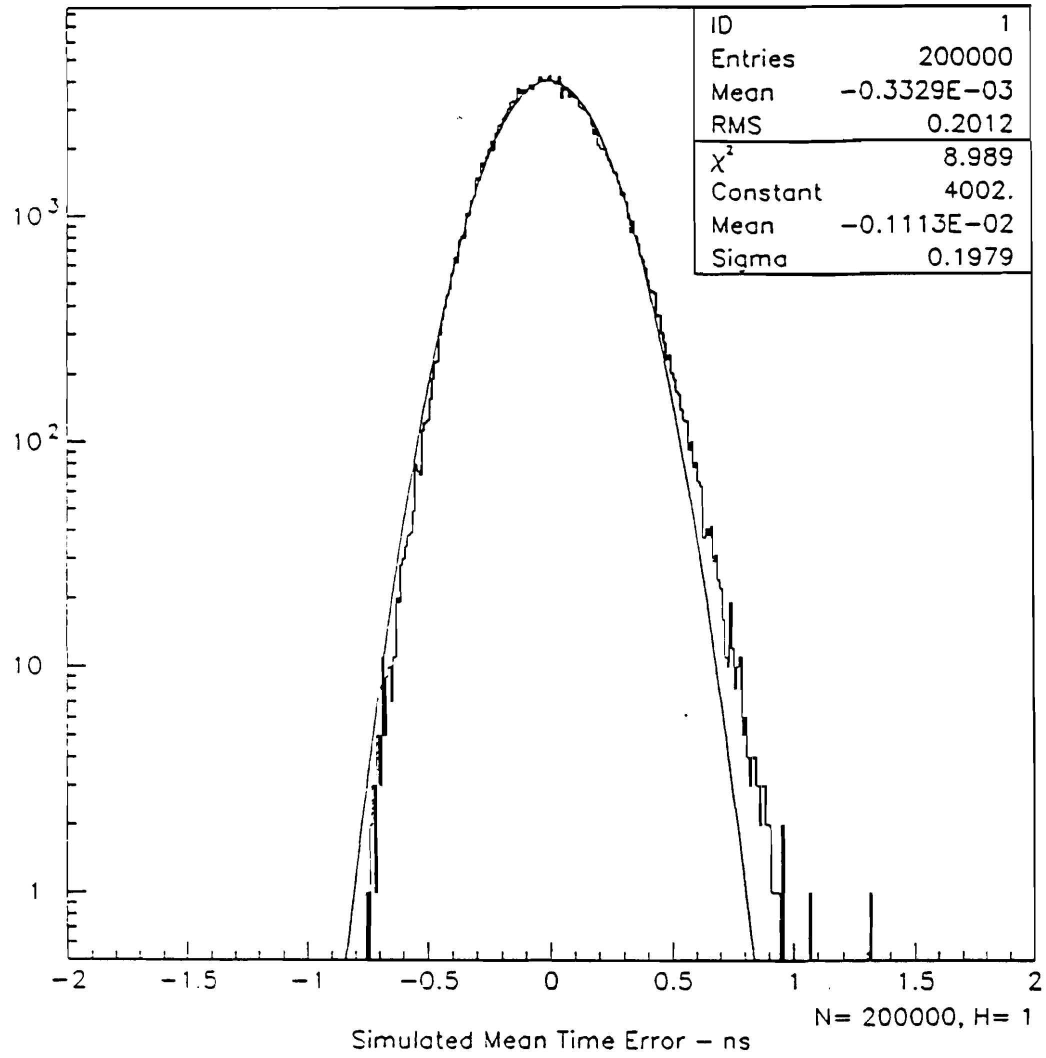

Figure 23: Typical distribution of times for 200000 particles striking the center of one counter. The solid curve is the best fit Gaussian.

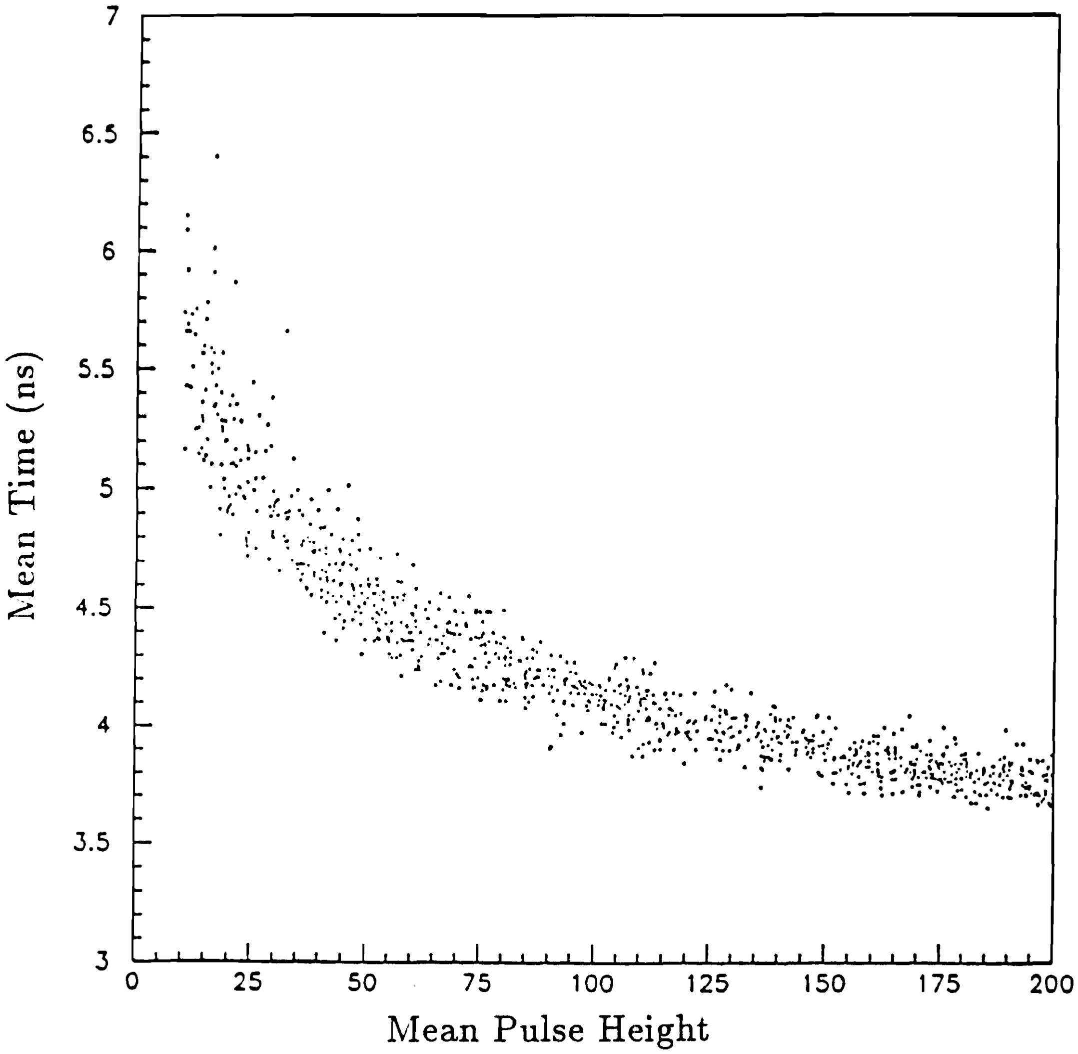

Figure 24: Mean time vs. pulse height (arbitrary units) from scintillation counter simulation. The slewing which is clearly visible is corrected in the analysis.

Table 11: Scintillator pulse height values used to assign charges in analyzing Monte Carlo data. Pulse heights are normalized to charge 1.

Pulse Height Range	0.75 or less	0.75 - 3.5	3.5 - 7.5	7.5 - 14.	14.0 or greater
Charge Assigned	0	1	2	3	4

to Table 11.

Pattern recognition then begins with the hodoscopes since, as discussed above, the hodoscopes provide a large amount of correlated information. For our Monte Carlo studies we reconstructed every track passing the cuts described below. In fact the only interesting tracks are those with velocities considerably less than the speed of light (β <0.973). In the analysis of data from the experiment we will impose time cuts on the hodoscope tracks before trying to fully reconstruct tracks. Since on average there are less than two tracks per event passing the "late time" cut, this will greatly reduce the computing time required for pattern recognition.

The pattern recognition proceeds by the following steps:

1. Find Hodoscope tracks. Find sets of hodoscope hits in H1,H2,H3 which have the same assigned charge, fit a line (within appropriate errors) in the horizontal, vertical and time dimensions. Cut on vertical and time projection to target.
2. Find confirming hits in all views in the downstream straw tube arrays (S2,S3).
3. Refit the horizontal and vertical track parameters using the straw tube information and cut again on the vertical projection to the target.
4. Do preliminary kinematics. Calculate rigidity from charge, angle and position of downstream track assuming the track emanated from the target. Project

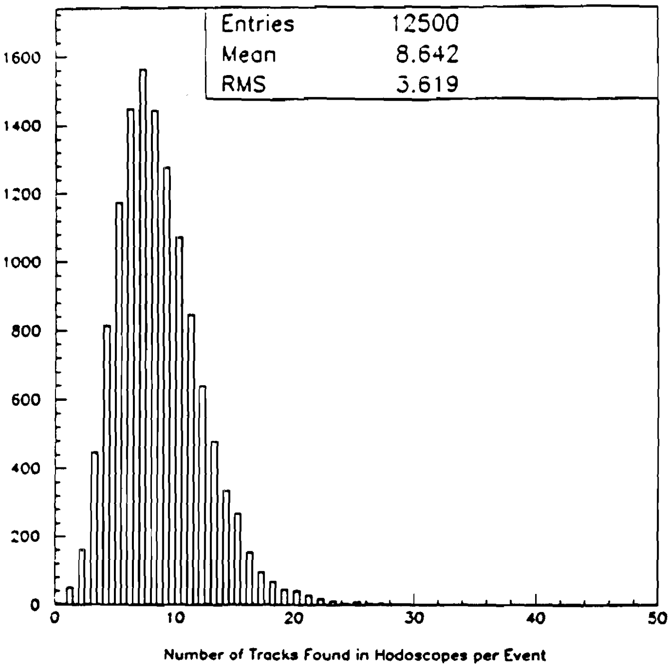

Figure 25: Reconstructed tracks found in the scintillator hodoscopes per event.

back upstream through second magnet (M2) and find confirming hit in all views in straw tube array S1.

5. Fit velocity and cut on $0.701 < \beta < 0.973$ (covering the rapidity range of interest).

6. Calculate rigidity and mass. If the mass is greater than $1.5\mathrm{GeV}/c^2$, (i.e. not a proton or lighter particle) use the velocity and a mass of 0.938 (proton mass) to calculate a rigidity R^*. Use R^* to track the downstream track segment back through the second magnet to S1. If a confirming hit is found in S1 the candidate is considered ambiguous with a conventional explanation (proton track not from target interaction) and is rejected.

Figure 25 shows the number of reconstructed tracks found in the scintillator hodoscopes per event using the cuts described above. Figure 26 shows the number of tracks per event with confirming hits found in the downstream straw tube arrays, and Fig. 27 shows the number of tracks per event with confirming hits in the upstream straw tube array. The means are shown on each histogram. The similarity of the means indicates that tracks found in the scintillators have a high probability of being good tracks confirmed in the other detectors.

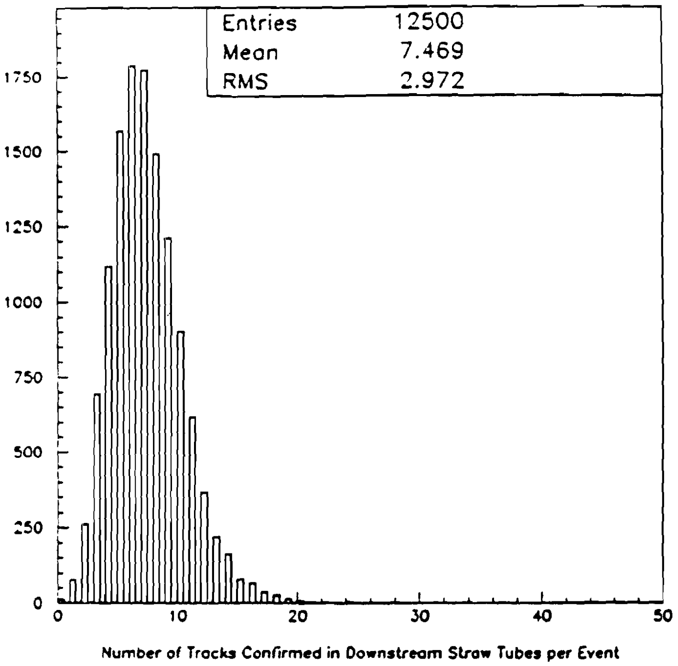

Figure 26: Number of tracks per event with confirming hits found in the downstream straw tube arrays.

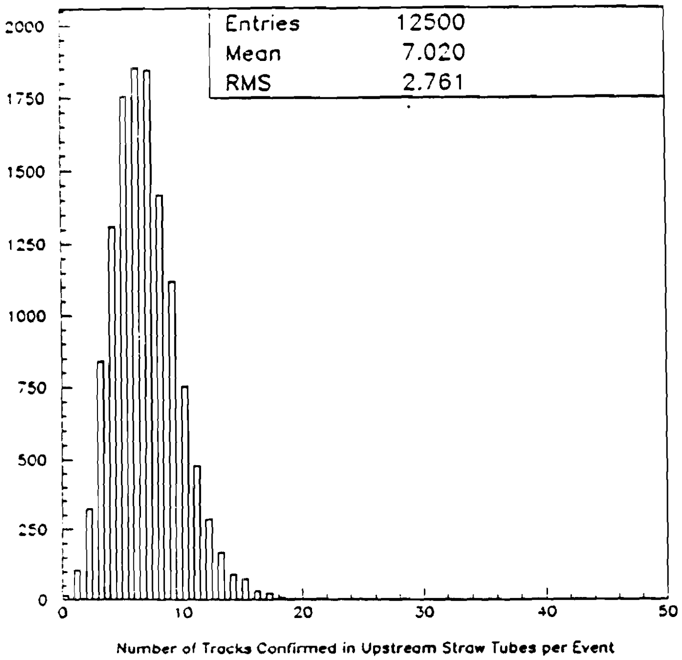

Figure 27: Number of tracks per event with confirming hits in the upstream straw tube array.

4.3.2 Single Particle Acceptance, Efficiency and Resolution

To calculate the net acceptance and efficiency for finding particles of interest we merged GEANT output for full central Au-Au collisions with shielding hits and with single particle events in which the species of interest was generated according to the model described above. Thus we can estimate not only the probability that the interesting particle makes it through the apparatus, but also the probability of finding the track in the presence of the other tracks in the event and tracks from interactions in the surrounding material.

Runs of this type were carried out for a few thousand each of several of the interesting species at the appropriate settings of the spectrometer magnets. Figure 28 shows the reconstructed mass spectrum for a charge +1 mass 12 GeV/c^2 object. Some central protons are accepted by the detector and appear in the plot along with the higher mass peak. Figure 29 shows the same plot with an expanded scale along with a Gaussian fit to the peak. The parameters of the fit are given on the plot. Table 12 gives the mass resolution, geometric acceptance and track reconstruction efficiency for several species covering the range of Z/A of interest at each of the magnetic field settings we plan to use. Also shown is the product of the acceptance times efficiency and the spectrometer magnetic field used. Both spectrometer magnets are set to the same field for all runs. The geometric acceptance of the apparatus is characterized by the acceptance in rigidity parallel and perpendicular to the incident beam direction ($R_{||}$ and $R_{\perp}$). Table 13 gives the acceptance in percent as a function of $R_{||}$ and $R_{\perp}$ for the spectrometer field set to +1.5T (positive strangelet search). For reference, a 10 GeV/c^2 strangelet at center of mass rapidity for 11.7 GeV/c Au-Au collisions has rigidity 25 GeV/c and average $P_{\perp}$ of 1.9 GeV/c according to our model. As an example, Table 14 shows the acceptance as a function of P_t and rapidity for a 10 GeV charge +1 strangelet with the spectrometer field set to +1.5T.

We have varied the parameters ($< P_t >$, σ_y) in the single particle generator over a reasonable range and have found the acceptance to be relatively insensitive to the details of the model. For example, varying $< P_t >$ from 0.5 to 0.9 changes the acceptance by from 10 to 30% depending on the charge and mass of the state considered.

A comment is in order regarding the overall tracking efficiency. In order to achieve very high background rejection redundant measurements are used. One must then require that every detector have the correct signal to form a good track. This means that, for example, if two particles strike a single hodoscope counter the vertical position measured by that counter will be incorrect, and will not match the straw tube hits. Both tracks will then be lost. We accept this inefficiency in

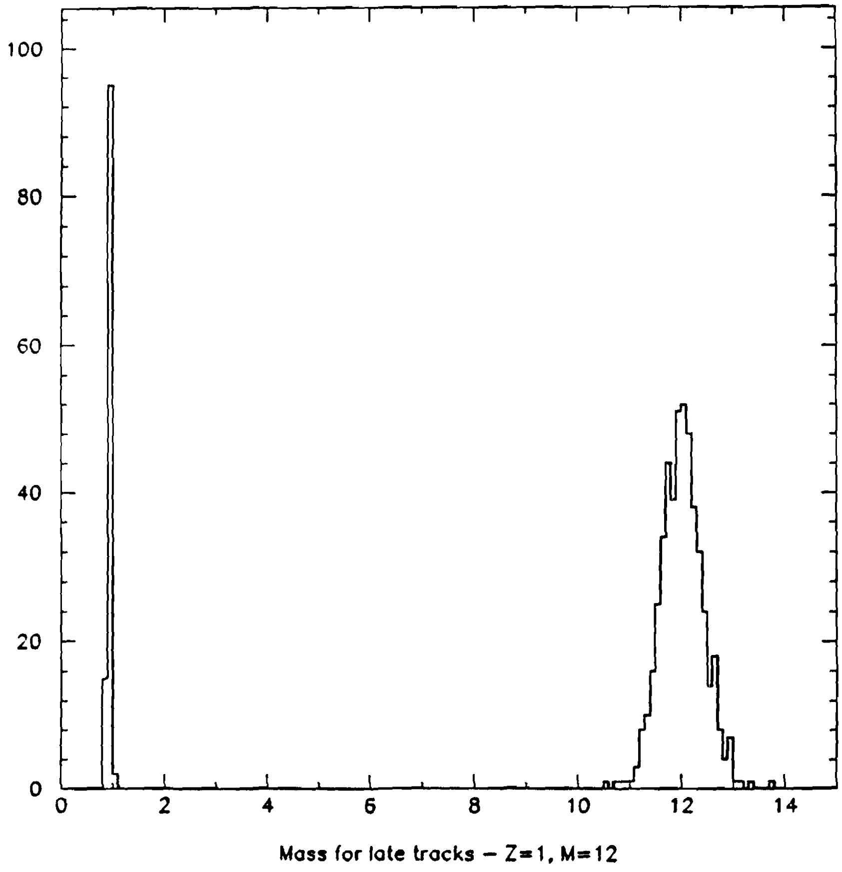

Figure 28: Reconstructed mass (GeV/c^2) spectrum for events with a charge +1 mass 12 GeV/c^2 object.

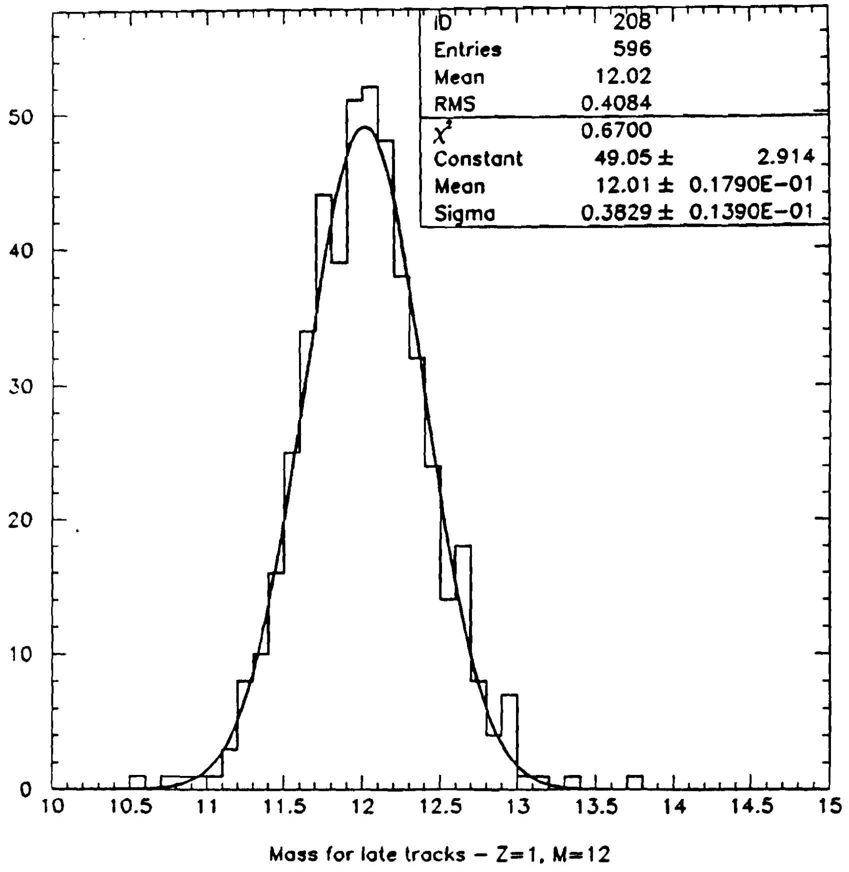

Figure 29: Reconstructed mass (GeV/c^2)spectrum for a charge +1 mass 12 GeV/c^2 object. Solid curve is a Gaussian fit to the peak.

Table 12: Summary of Single Particle Acceptance and Tracking Efficiency

Particle	Mass (Gev)	$\frac{\delta M}{M}$	Magnetic Field (T)	Acceptance	Tracking Efficiency	Acceptance × Efficiency
Z=1, M=12	12.0	0.032	+1.5	16.0 %	69 %	11.0%
Z=2, M=12	12.0	0.021	+1.5	15.7 %	67 %	10.5%
Z=3, M=12	12.0	0.019	+1.5	15.3 %	60 %	9.2%
^{3}He	2.82	0.027	+0.75	8.9 %	42 %	3.7%
^{8}He	7.48	0.022	+0.75	14.3 %	65 %	9.3%
$\overline{^3He}$	2.82	0.026	-0.75	8.9 %	38 %	3.4%
$\bar{t}$	2.82	0.026	-0.75	10.3 %	55 %	5.7%
$\Sigma^-\Sigma^-$	2.16	0.031	-0.45	8.1 %	36 %	2.9%
$\Omega^-\Omega^-$	2.92	0.030	-0.45	10.3 %	56 %	5.7%

order to achieve high background rejection. As discussed above, we have studied the optimization of scintillation counter sizes to minimize such losses. For more abundant species, where the highest background rejection is not required, one can be less stringent than requiring every detector to have the correct signal. Also, as a possible upgrade, we could add multi-hit capability to the digitizers. We have not assumed either of these however in calculating the efficiencies given in Table 12.

For neutral particles, we use the same single particle model to calculate the geometric acceptance. The efficiency for finding showers in the calorimeter will be discussed below. Table 15 gives the geometric acceptance for neutral particles for several masses over the range of interest.

4.3.3 Charged Particle Backgrounds

As mentioned earlier the most challenging requirement for background rejection is for charge +1 high mass states, since this is where we wish to achieve the highest sensitivity, and where the background rates will be highest. Below we give the results of a Monte Carlo study of the dominant backgrounds for these states.

Our first test of the rejection power of the tracking system design was simply to run

Table 13: Acceptance in percent as a function of parallel and perpendicular rigidity

						3	4	4	5
					2	4	5	5	6
					4	4	5	6	7
				3	4	5	6	8	10
			1	4	6	6	9	12	19
			3	6	7	10	18	27	34
		2	5	8	14	27	34	35	32
		5	11	25	34	33	29	26	22
	6	22	31	28	22	16	9	4	1
5	18	11	5	1					

$R_{perpendicular}$ GeV: 8, 6, 4, 2, 0

0, 20, 40, 60, 80 $R_{parallel}$ GeV

Table 14: Acceptance in percent for a 10 GeV charge +1 strangelet. The center of mass rapidity for Au-Pb collisions is 1.59

rapidity	0.2	0.4	0.6	0.8	1.0	1.2	1.4	1.6	1.8	2.0	2.2	2.4	2.6	2.8	3.0	3.2
P_t (GeV)																
0.4		9	40	36	31	25	15									
0.6			7	33	38	34	29	23	13							
0.8				12	33	38	35	31	26	18						
1.0				7	15	36	38	35	31	26	18					
1.2				4	8	18	39	38	35	31	25	17				
1.4					7	9	22	39	37	34	29	23	14			
1.6					6	8	13	31	39	36	32	27	21	9		
1.8					5	7	9	18	37	37	35	30	25	17		
2.0					1	6	8	12	30	39	36	32	28	21	11	
2.2						6	7	9	19	37	37	34	30	25	17	
2.4						5	6	9	14	35	38	36	32	27	21	8
2.6						4	6	8	10	24	37	37	34	29	23	14
2.8							6	7	9	17	37	38	35	31	26	18
3.0							5	6	9	13	34	39	36	32	27	21
3.2							5	6	8	11	25	36	37	34	29	23
3.4							4	6	7	9	18	36	37	35	30	25
3.6							1	6	7	9	15	36	38	35	31	27
3.8								5	6	8	12	31	37	36	32	28

Table 15: Percent acceptance for neutral particles.

Mass - GeV/c^2	Percent acceptance
2.0	8.5
4.0	11.0
6.0	11.3
8.0	12.6
10.0	12.8
12.0	13.6
14.0	14.2

a large number of central Au-Au collisions (62,500) with the spectrometer field set for the positive strangelet search (+1.5T) and reconstruct all masses for tracks in the desired velocity range ($0.701 < \beta < 0.973$). This sample included all interactions in the detectors and air and had shielding hits overlaid as described above. When this sample was analysed as described above no masses outside the proton peak were found.

In studying this sample of events, we realized that if we loosen the requirements on the first straw tube array (S1) (i.e. do not require a confirming hit in S1) products from interactions in S1, S2, or the vacuum window could sometimes fake high mass objects. Thus if we could run enough simulated events we would find fake high mass events from interactions in S1, S2, or the vacuum window with a coincidental confirming hit in S1 due to some other track. This means that S1 is a possible single point failure for the tracking system. To study this background further we generated a sample of events in which we kept only those events with an interaction in a particular detector component. To further "distill" the sample we also required that the interaction send a charged track through the rest of the apparatus. This is precisely the process which, combined with a coincidental hit in S1, can fake a high mass track.

We note that to produce a fake high mass candidate the track must still have reasonable properties - it must point back to the interaction vertex vertically and in time, and must give a velocity in the desired range. Also, for all of these processes the track must point to a valid shower in the calorimeter having the correct position, time and energy. As discussed above, the calorimeter analysis is treated separately, leading to a background rejection factor which is independent of the rejection of the tracking system.

Table 16 summarizes the results of analyzing central events with interactions in S1, S2, and the vacuum window (125,000 each). The simulation included all GEANT physics processes, and the events have shielding hits overlaid. The first four rows in the table list the materials and thicknesses used for the three sources of interactions. The next row gives the fraction of all central interactions which produced a secondary interaction in the specified detector. The next row lists the fraction of these secondary interactions that gave a charged track which made it all the way to the calorimeter. Next we give the number of events generated (125,000 for each source) which, when divided by the two fractions above, gives the number of central interactions required to produce these events. Finally, since the central interactions represent about 10% of the total interaction cross section, we give the total number of interactions required to produce these events. We then list the number of high mass candidates (mass ≥ 10 GeV/c^2) found. This allows the tracking system rejection for background from these sources to be computed. As shown in the last two rows of the table, to achieve a rejection of $<9.7\text{x}10^{-12}$, or one fake candidate per 10^{11} interactions requires a rejection of 1/20000 for the calorimeter. The analysis given below in the section on the calorimeter analysis for charged particles indicates that for masses greater than 7.5 GeV/c^2 a rejection of 1/72000 should be possible for the calorimeter we propose.

Figure 30 shows the mass spectrum for all late tracks reconstructed in the above analysis. Note again that every event in this analysis was forced to have an interaction in S1, S2, or the vacuum window which sent a charged particle through the rest of the apparatus, so that for background analysis this sample represents 6.82×10^8 interactions. For the analysis above we have somewhat arbitrarily put a lower mass cutoff of 10 GeV/c^2. Looking at the mass spectrum, however, one can see that even going as low as 3 GeV/c^2 would not more than double the background.

We should note that even though the simulations described above indicate that the apparatus has the desired rejection, there are a number of possible improvements which can be implemented within the scope of the present design. One possible improvement in tracking is to have some track vector information between the two spectrometer magnets. This could be accomplished without adding any more channels simply by longitudinally separating the three coordinates of S1. Another improvement in the tracking analysis is to reject hits in S1 as confirming hits for high mass candidates if the hits are shared with another track. We believe improvements in the calorimeter shower algorithm are also possible and we will study this further using the output of the GEANT calorimeter simulation discussed below.

We illustrate the possible tracking improvements by showing one of the events from our simulation. This event has a candidate which was rejected as ambiguous with a proton that did not come from the target. Figure 31 shows a plan view of the hits in the detectors. The beam is from the left and the target and first magnet are off the page to the left. The scale at the bottom shows the distance from the target in meters. Only the useful field volume of the second magnet and the actual hits in the detectors are shown. Figure 32 shows the same event with the downstream track segments found by the analysis program. One track as indicated passes the velocity cut to be considered a late track ($\beta < 0.937$). Figure 33 shows the event with all tracks projected upstream to S1. The reconstructed mass for the late track using the downstream track segment is shown. Figure 34 shows an expanded view of the tracks at S1 with the late track indicated. The late track matches well with one of the hits in S1. (It also matches well in the other views.) This particular hit is shared with another track so that the late track would be rejected by the improvement suggested above. Figure 35 shows the projection of the late track using the measured time of flight but assuming a mass of 0.938 GeV/c^2. This assumption gives a projection which also matches a hit in S1 (in both views). Thus, this candidate is rejected as

Table 16: Summary of Background Due to Interactions in S1, S2 and Vacuum Window

Source	S1	S2	Vacuum Wind.
Material	Mylar+Ar	Mylar+Ar	Mylar
Thickness	0.048+2.4 cm	0.048+2.4 cm	0.05 cm
Interaction Lengths	7.78×10^{-4} $+1.0 \times 10^{-4}$	7.78×10^{-4} $+1.0 \times 10^{-4}$	8.1×10^{-4}
Radiation Lengths	1.67×10^{-3} $+4.0 \times 10^{-4}$	1.67×10^{-3} $+4.0 \times 10^{-4}$	1.74×10^{-3}
Fraction of Cent. Triggers Giving Interaction	3.17%	3.17%	3.5%
Fraction of Int. Giving Charged Track in Cal.	11.2%	24.1%	21.5%
Number of Int. with Charged Tracks in Cal.	125,000	125,000	125,000
Equiv. Number of Central Int.	3.52×10^{7}	1.64×10^{7}	1.66×10^{7}
Equiv. Number of Total Int.	3.52×10^{8}	1.64×10^{8}	1.66×10^{8}
Background events Found	1	0	1
Tracking Rejection	2.84×10^{-9}	6.06×10^{-9}	
Tracking Reject. /(accept. x effic.)	0.618×10^{-7}	1.32×10^{-7}	
Tracking Rej. all Three Sources	1.94×10^{-7}		
Calorimeter Rejection	$< (1/20000)$		
Total Rejection	$< 9.7 \times 10^{-12}$		

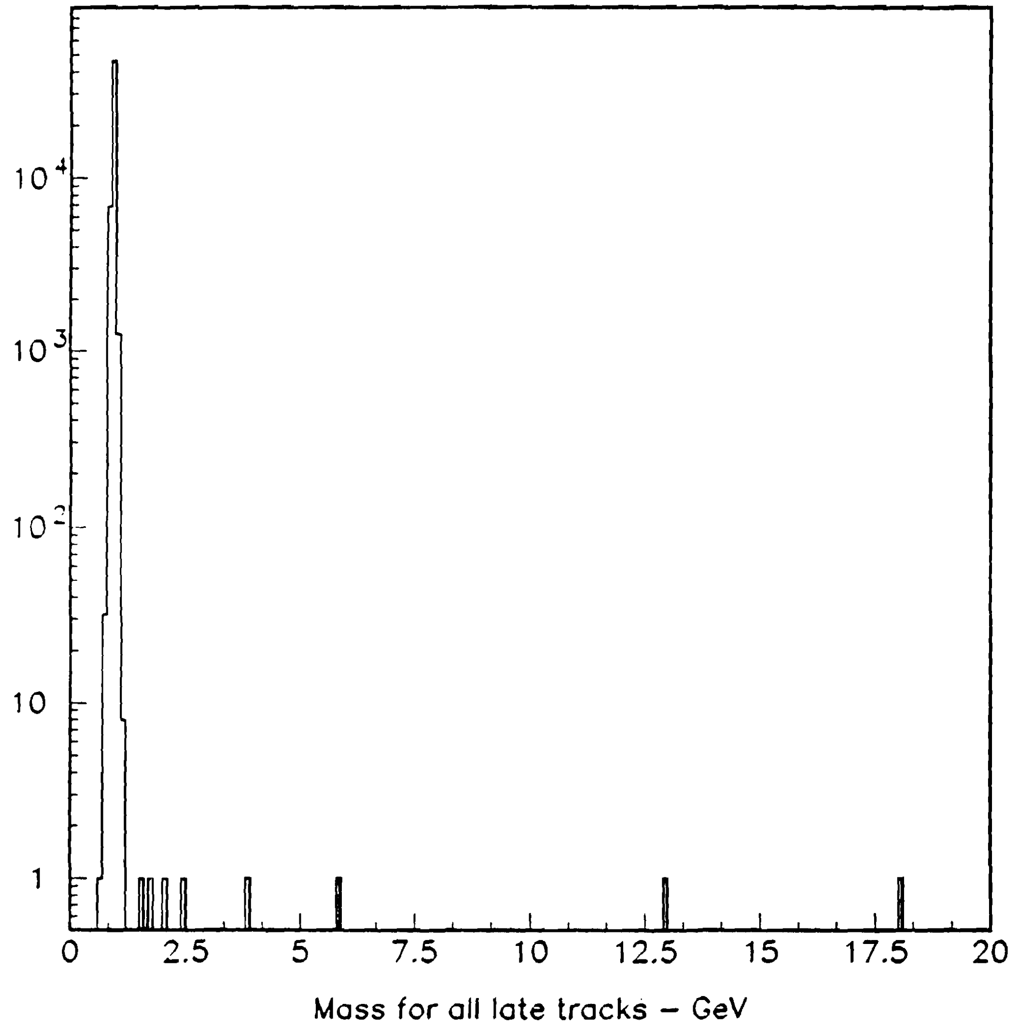

Figure 30: Mass spectrum for all late tracks reconstructed in the background analysis. Every event was forced to have an interaction in S1, S2 or the vacuum window which sent a charged particle through the rest of the apparatus.

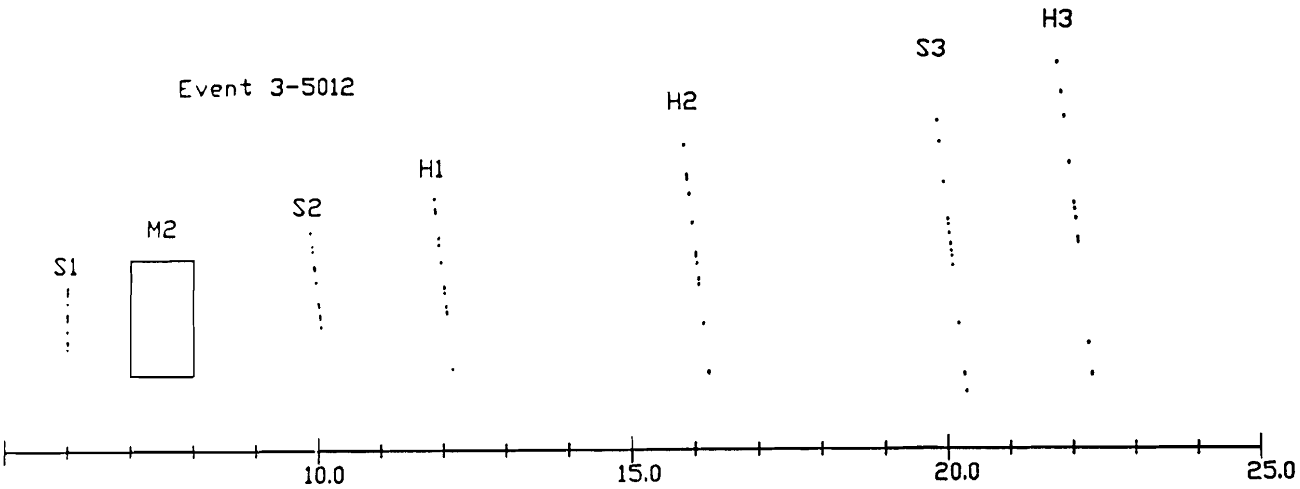

Figure 31: Plan view of Monte Carlo Event. Only active volume of second magnet and hits in detectors are shown. Scale shows distance to target in meters.

ambiguous.

4.4 Calorimeter Analysis and Simulation

4.4.1 Overview

The calorimeter is used as a means of reducing the background in the charged particle measurements and searches by providing confirming measurements of the position, time of flight and energy. Since the calorimeter can measure both time of flight (velocity) and energy it provides an independent measurement of mass. The mass resolution of charged particles is much more precisely determined with the tracking system than with the calorimeter. For neutral particles, the calorimeter provides the only measurement. The tracking system is used only to verify that the observed energy did not come from charged particles.

Below we will discuss the simulations and analysis we have carried out to calculate the efficiency of the calorimeter for detecting interesting states and also the rejection power of the calorimeter for background processes.

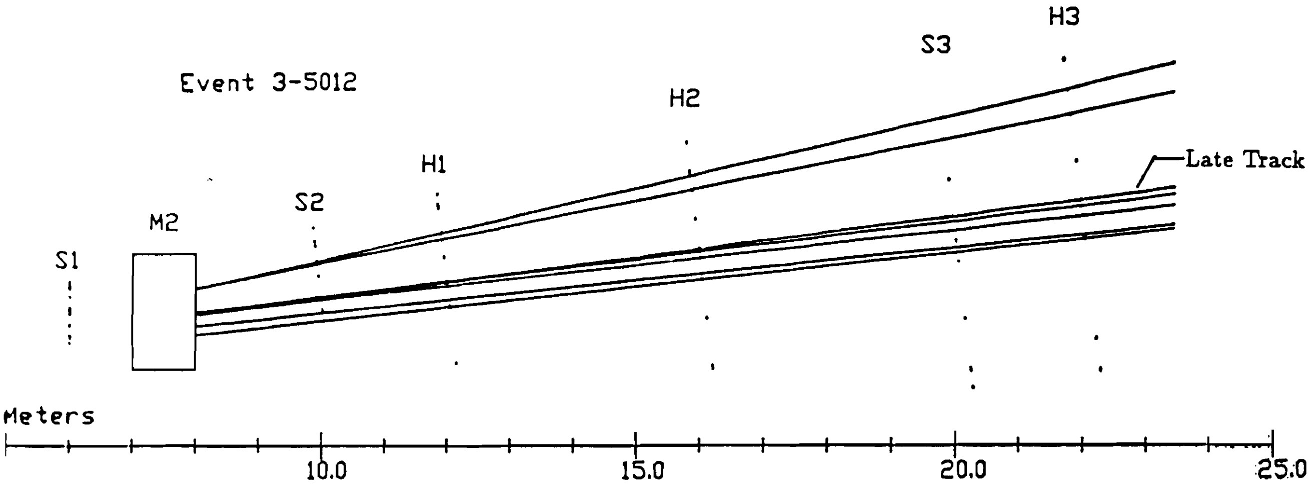

Figure 32: Monte Carlo event with reconstructed downstream track segments. Late track is indicated.

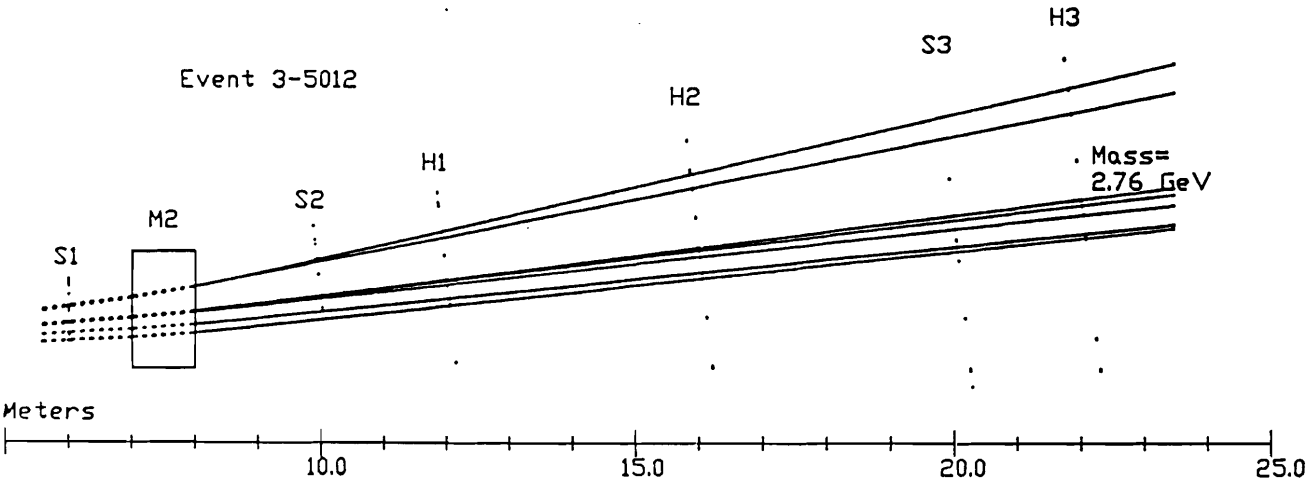

Figure 33: Monte Carlo event with track segments projected upstream through second magnet. Reconstructed mass is shown for late track.

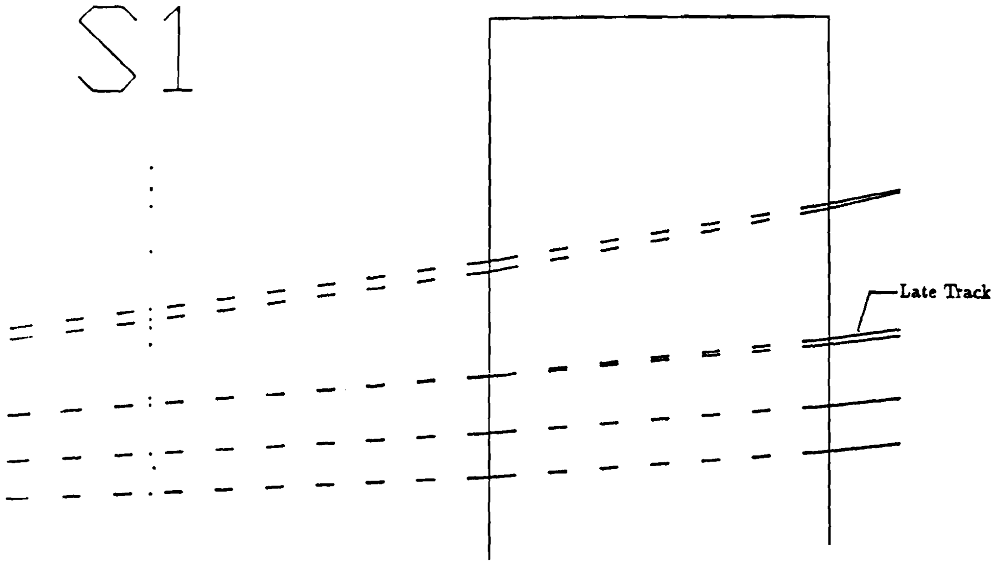

Figure 34: Expanded view of Monte Carlo event at first straw tube array (S1). Late track is indicated.

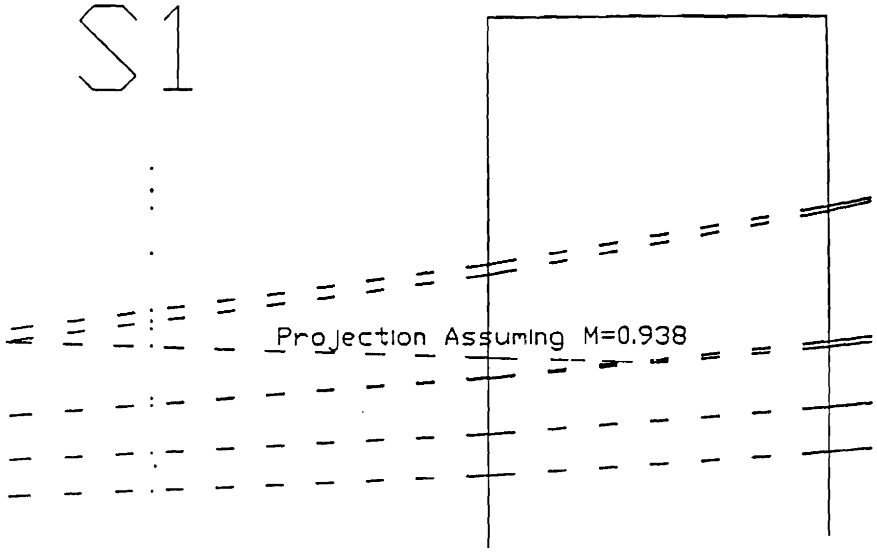

Figure 35: Monte Carlo event at S1 with late track projection assuming proton mass.

4.4.2 Calorimeter - Charged Particle Analysis

As discussed above the main background for the tracking system analysis for high mass states is from processes which result in a genuine slow track through most of the apparatus. For processes which produce a proton with the "right" kinematics to fake a strangelet we have shown above that the tracking system has a rejection of 1.94×10^{-7} per collision. To achieve the desired sensitivity for high masses the calorimeter must supply further rejection of better than 10^{-4}. Although this may seem to be an ambitious requirement for the calorimeter, one should observe that to fake a high mass particle, the apparent energy in the calorimeter which is matched with a fake high mass candidate found by the tracking system must be many times greater than the typical central nucleon energy. For example, in order to fall within our timing window such a background track must be necessarily "slow" ($\beta \leq .96$, corresponding to $y_{max} = y_{cm} + 0.5 = 1.8877$). Allowing for a maximum calorimeter timing error of 0.5 ns, the fastest accepted proton will deposit at most 2.4 GeV in the calorimeter. In contrast, a 10 GeV/c^2 strangelet with the same rapidity will deposit 24 GeV in the calorimeter. The job of the calorimeter is to distinguish, with high reliability, between these two possibilities. As might be expected, the dominant process which can cause the calorimeter to fail to make this discrimination is the accidental overlap of several neutrons, in spatial and temporal coincidence (to within the calorimeter resolution) with the tertiary proton track. We have performed a Monte Carlo study of the calorimeter rejection with the result that the calorimeter, as we propose to construct it, has more than adequate ability to reject such background. We have also used this simulation to calculate the efficiency for detecting calorimeter showers from high mass particles in the presence of full central events.

4.4.2.1 Simulations Since the most challenging charged particle search is for charge +1 objects, we simulate the apparatus with the spectrometer magnets set to +1.5T (positive strangelet search). To study the calorimeter, we begin with events generated as described above in the section on HIJET/GEANT. To measure the background rejection, 8000 full central collisions with particles from the shielding overlayed were used. To study the efficiency, 15 GeV/c^2 strangelets produced according to the single particle production model described above were overlayed on a small sample of these events. The impact point, time of flight and four vector of every particle striking the calorimeter was available.

The calorimeter response was simulated in two ways. First we used the measured (average) transverse shape of hadronic showers in the SPACAL calorimeter and an analytic expression for the longitudinal shower shape. These average distributions were used in a way that simulated some of the shower fluctuations about the average behavior. We do not discuss this in detail because the second approach is easier to explain and gave essentially the same results.

The second method used the program CALSIM to simulate showers in a simplified calorimeter geometry (transverse lead and scintillator plates with the correct volume ratio of 4 to 1, and with the 10 cm by 10 cm tower geometry we will use). In addition, the timing of the calorimeter signal at each phototube was calculated as if the scintillators were running in the beam direction. This simulation also made other simplifications such as ignoring energy deposit mechanisms other than fast particle energy loss and stopping protons. Thresholds for neutral particle tracking were 2.5 MeV for gammas and 10 MeV for neutrons. Energy deposits from particles below the tracking threshold account for 15% of the shower energy. The resulting simulation is certainly not adequate for designing calorimeters, but it should be quite adequate for evaluating the effects of resolution and fluctuations. The simulation showed a resolution of $\delta E/E \cong .4/\sqrt{E}$.

A library of 300 shower simulations (100 at each of three energies: 2.5 GeV, 5.0 GeV, and 10.0 GeV for the incident neutrons) was generated and used to calculate the calorimeter phototube signals from the entire array of particles in a HIJET/GEANT event striking the calorimeter. For any given hadron energy the nearest library energy was chosen and the library outputs were scaled to give the same total energy deposit as the given hadron would have done. Before using the signals in the analysis, the pulse heights were smeared by an additional 4%. This was done to lessen any effects due to the repeated use of the same showers from the library. It was assumed that the contributions to the signal of any tower due to more than one shower simply added linearly.

For each event we generated a set of tower energy deposits and a set of times (a "software" discriminator was attached to each tower and the time at which the phototube detected an energy deposit greater than .33 GeV was determined). The timing was accurately simulated, taking into account the propagation time of light in the scintillator, the arrival times of all the particles striking the tower, the velocities of the shower particles, etc. All the particles striking the calorimeter contributed to the set of tower energies and times.

4.4.2.2 Calorimeter Analysis In the analysis a fairly simple pattern recognition algorithm was used. The time of flight was taken as known because the real background track will be charged and will have its time of flight measured by the hodoscope system. The shower was rejected if any tower within 19.5 cm of the candidate impact point had a time outside of the correct time by ±1.0 ns. The shower was rejected if any tower neighboring the struck tower (the tower to which the candidate points) showed an energy deposit in excess of E_{cut} where

$$E_{cut} = E_{cen}(1.27 - .053r)$$

where r is the distance between the neighboring tower center and the hit location, and E_{cen} is the energy of the struck tower plus the energies of any neighboring towers within 1.5 cm of the hit location. The cluster energy was taken (for the surviving showers) as the sum of all the tower energies in towers that were within 19.5 cm of the hit location. This algorithm is rather crude (e.g. it does not make any detailed fit to the shower shape, or make use of available information on nearby showers), however it is adequate for the purpose of rejecting background for the charged particle search. As will be discussed below, this simple algorithm is not adequate for rejecting low mass backgrounds for neutral particle searches.

4.4.2.3 Single Particle Efficiency

The analysis has an efficiency for detecting real strangelets (or comparable particles) which is less than unity because the shower due to the strangelet may be overlapped by other showers. A Monte Carlo study of 15 GeV/c^2 strangelets overlayed on events with full central collisions shows that the analysis described above has an efficiency of 42% for identifying strangelet energy deposits.

The study also shows that the calculated energy deposit, as might be expected from the limitation to towers within 19.5 cm of the hit location, is about 2/3 of the true energy deposit.

4.4.2.4 Background Rejection

As discussed above, it is impossible to fully simulate the experiment at the desired level of sensitivity (i.e. generate and track 10^{12} interactions) therefore we study enhanced background processes. We have taken a sample of 8000 full central collisions including particles from interactions in the shielding and the detectors, all decays, etc. and processed them to simulate the calorimeter response.

To enhance the simulated background from interactions in the upstream detectors, each central rapidity neutron which strikes the calorimeter is taken as a potential strangelet candidate. The real background tracks are, of course, protons created by an upstream interaction, but our studies show that the troublesome protons have energies in the range of the neutron sample. So we imagine that each selected neutron is a background proton, and see how often we can reject it using the calorimeter.

For each such "candidate" the calorimeter signals were analyzed, as discussed above, and an energy deposit determined. The mass of the candidate was then calculated from the energy deposit and the time of flight. The mass error is totally dominated by the calorimeter energy resolution so we did not "smear" the time of flight. The resulting mass spectrum is shown in Fig. 36. The open squares show the reconstructed mass from calorimeter energy deposit and time of flight for 72,000 neutrons. Also shown as filled triangles is the reconstructed mass for 100 strangelets of mass 15 amu. We note that 42 strangelets survive the timing and shape cuts described above, and that the average calculated mass is 10 GeV (uncorrected for the energy outside the cluster size used in the analysis).

Figure 36 shows that the calorimeter analysis has a probability of 1/72,000 of assigning a mass greater than 5.0 GeV to a background track. Recalling that only 2/3 of the energy is inside the clusters used in this analysis, which is not corrected in Fig. 36, this corresponds to a true mass of 7.5 GeV.

4.4.2.5 Summary of Calorimeter Analysis for Charged Particles To summarize, the calorimeter rejection power for background tracks in the positive strangelet search is 1/72,000 or better, and the strangelet calorimeter analysis efficiency is 42%. These are adequate for the sensitivity goals of the positive strangelet search which is the most demanding of the charged particle studies in the experiment.

The analysis algorithm used is simpler than that which will be used in the actual experiment, but serves to give conservative limits to the calorimeter efficiency and rejection power. In the real analysis we will use the information provided by the hodoscope and wire chamber systems to help untangle the calorimeter pattern. Also, we will do a more elaborate fit to the calorimeter data to extract the pattern of energy deposits in the vicinity of the candidate hit.

It is perhaps worth mentioning that the excellent rejection power of the calorimeter is directly related to the simultaneous measurement of both the energy deposit and the time at which the deposit occurred in each tower. The good timing property of the spaghetti calorimeter design, along with its tower geometry, hermeticity, and good energy resolution, make it the overwhelmingly preferred choice for the E-864 calorimeter design.

4.4.3 Calorimeter Analysis, Neutral Particles

The calorimeter is the primary detector for the study of neutral particles. The flight times and energy deposits measured by the calorimeter are the basic data from which the masses of the incident particles are deduced. The hodoscopes and wire chambers will be used to identify charged particles incident on the calorimeter so that their signals will not be confused with those of neutrals.

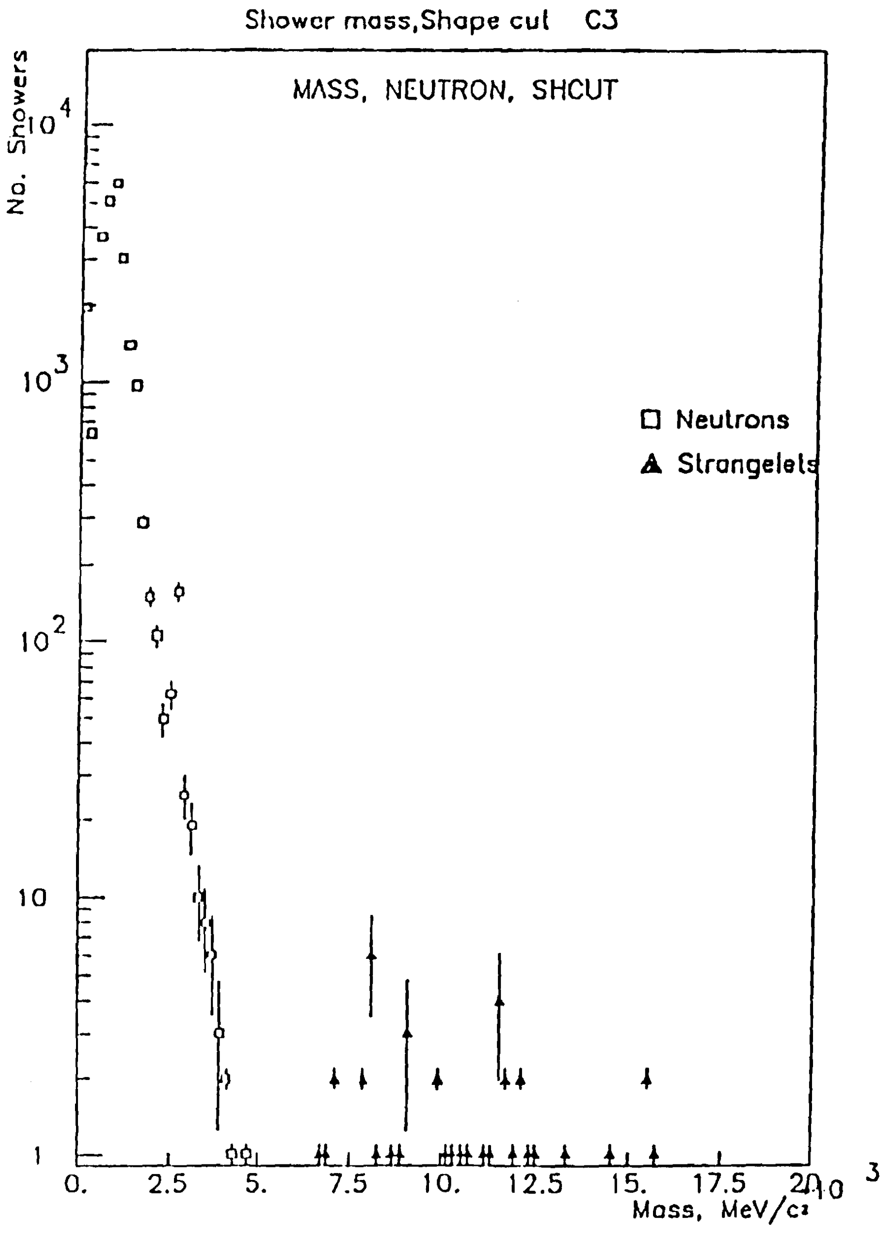

Figure 36: Mass spectra for 72,000 late neutrons (open squares) and 100 strangelets of mass 15 amu (dark triangles) as determined from calorimeter energy deposit and time of flight. See text for further details.

We have not yet carried out a fully detailed Monte Carlo simulation however we draw upon experience with the E814 calorimeters to understand what may be possible in E864. The E814 calorimeters have a tower geometry with transverse dimensions of 20 cm (horizontally) by 10 cm (vertically). The individual towers in E814's calorimeter do not have independent time measurements, although the sum of all 12 towers in each vertical stack have a time measurement with an r.m.s. error of about 1 ns. The timing is not used in the E814 cluster-finding analysis. By using the shower shapes two 14 ± 5 GeV neutrons can be distinguished if they strike the calorimeter more than 5 cm from one another. To do this, a program which uses a fast Monte Carlo as part of a chi-squared analysis of multi neutron hypotheses is necessary. In this analysis the best one neutron hypothesis (energy and impact point) is compared with the best two neutron hypothesis, etc.

In E864 the tower geometry, good resolution, hermeticity, and excellent time resolution of the spaghetti design are essential ingredients for the neutral particle studies. It will be important to use the best possible analysis techniques to identify showers caused by the accidental overlap of several neutrons which can simulate higher mass particles. The E864 calorimeter will have 10 cm by 10 cm towers. Each individual tower will have a time measurement with an expected r.m.s. error of 0.5 ns or less. The TDC's attached to each tower will be "single hit" TDC's. Thus, if two neutrons hit a given tower, only the time for fastest will be recorded. This results in the two overlapping neutron events displaying a lower mass, on the average, than two neutron masses.

The most challenging task for the calorimeter is to detect a possible signal from the H^o-dibaryon. Since the mass is expected to be slightly more than twice the neutron mass there will be background from the resolution tail of single neutrons and from overlapping double, triple, etc., neutrons. For possible higher mass states, the background problems become less severe as the mass increases. We focus the discussion below on the most difficult task of detecting the H^o.

We estimate the background to the H^o as follows. A sample of HIJET/GEANT central Au-Au collisions are traced through the tracking system to the calorimeter. These events include all physics processes and tracks from shielding interactions. From this sample of events we select all neutrons entering the calorimeter which were late ($\beta < 0.976$) but would still fall inside the ADC gates (TOF $<$ 142 ns). These neutrons are then analyzed using gaussian errors for the calorimeter energy and time of flight.

Single neutrons are analyzed under both the hypothesis that the calorimeter energy is deposited by a neutron and that it is deposited by an H^o. Figure 37 shows a scatter plot of the two mass hypotheses assuming an RMS energy resolution $\delta E/E =$

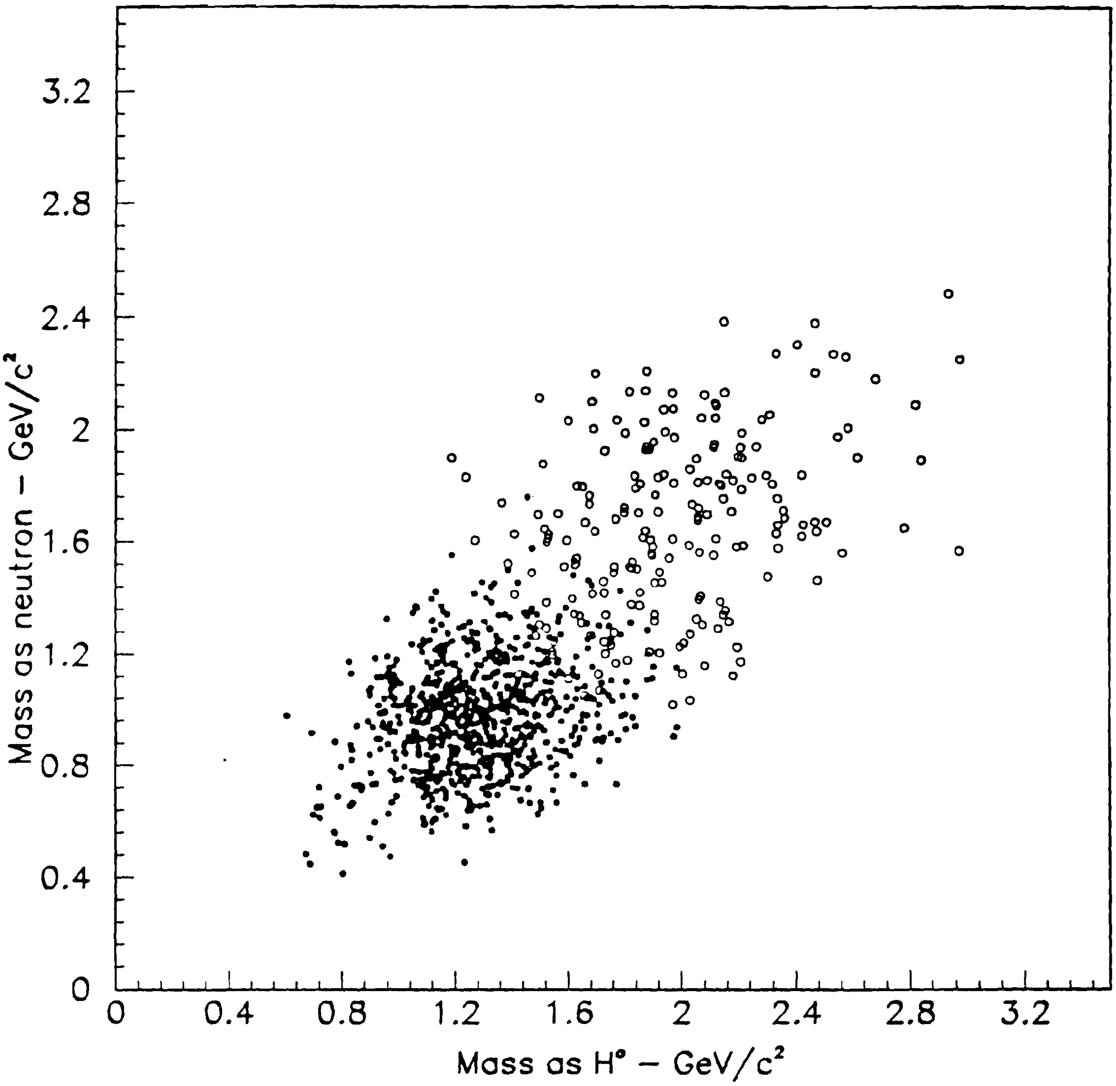

Figure 37: Scatter plot of reconstructed mass of particles interpreted as neutrons and as H°'s. Dots are for neutrons and open circles are H°'s

$0.4/\sqrt{E}$ and and RMS timing resolution of 0.5 ns. Also shown in Fig. 37 is a sample of H^o's (open circles) selected and reconstructed in the same manner. The H^o's are generated with a mass of 2 GeV/c^2 according to the single particle model described in the section on HIJET/GEANT. Although the scatter plot looks encouraging for detecting the H^o's, one must recall that the number of neutrons striking the calorimeter is about 7 per central event. The number of H^o's per central event is about 0.1(acceptance - see Table 15) $\times F_H$. F_H is the production rate of H^o's per central event and is expected to be 10^{-1} to 10^{-3}. From Fig. 37 one can see that the sum of the two mass hypotheses ($M_n + M_H$) will be an effective discriminator between neutrons and H^o's. Figure 38 shows a histogram of this quantity for single neutrons (solid) and H^o's (dashed). Clearly, to minimize background from single neutrons in the H^o region it is necessary to have excellent resolution and to minimize the high mass tail of the resolution. Figure 39 shows the expected apparent mass of neutrons reconstructed as H^o's as a function of time of flight (with time for a v=c particle subtracted). Also shown is the effect of adding one standard deviation to the time of flight or to the energy and the combined effect of both. As expected, for short times (velocity near c), the time of flight error dominates the mass resolution. For very slow particles, the shape of the curve brings the apparent mass closer to the H^o mass. We clearly can have better separation of H^o's and neutrons by eliminating early and late times. Figure 40 shows the apparent mass of neutrons reconstructed as H^o's as a function of time of flight. Figure 41 shows a histogram of the apparent mass of neutrons reconstructed as H^o's after applying the additional timing cut: $95.5 < \mathrm{TOF} < 110$ ns ($0.83 < \beta < 0.96$). About 80% of the H^o's pass these cuts which are clearly useful in reducing the high mass tail from the neutrons (compare Fig. 41 with the single neutron spectrum in Fig. 38).

We will give a quantitative estimate of the single neutron background below, but first we consider background from overlapping neutrons. We use the same sample of central collisions described above, but now select pairs of neutrons that fall within a certain distance of each other, or triplets of neutrons that fall within a certain distance from the energy weighted centroid of the triplet. In each of these cases the calorimeter energy for the pair or triplet is summed, and the time of flight of the earliest neutron is assigned to this energy (the DA system has single hit TDC's). This system is then reconstructed as above under both the assumption of a single neutron and an H^o. Figures 42 and 43 show the spectrum of the sum of the two mass hypotheses for pairs and triplets of neutrons using the timing cuts described for the single neutrons above.

To estimate the sensitivity we assume a 100 hour run using only the multiplicity trigger. Such a run will record 2.88×10^8 central collisions. We actually plan two such runs - one with positive magnetic field and one with negative field. The

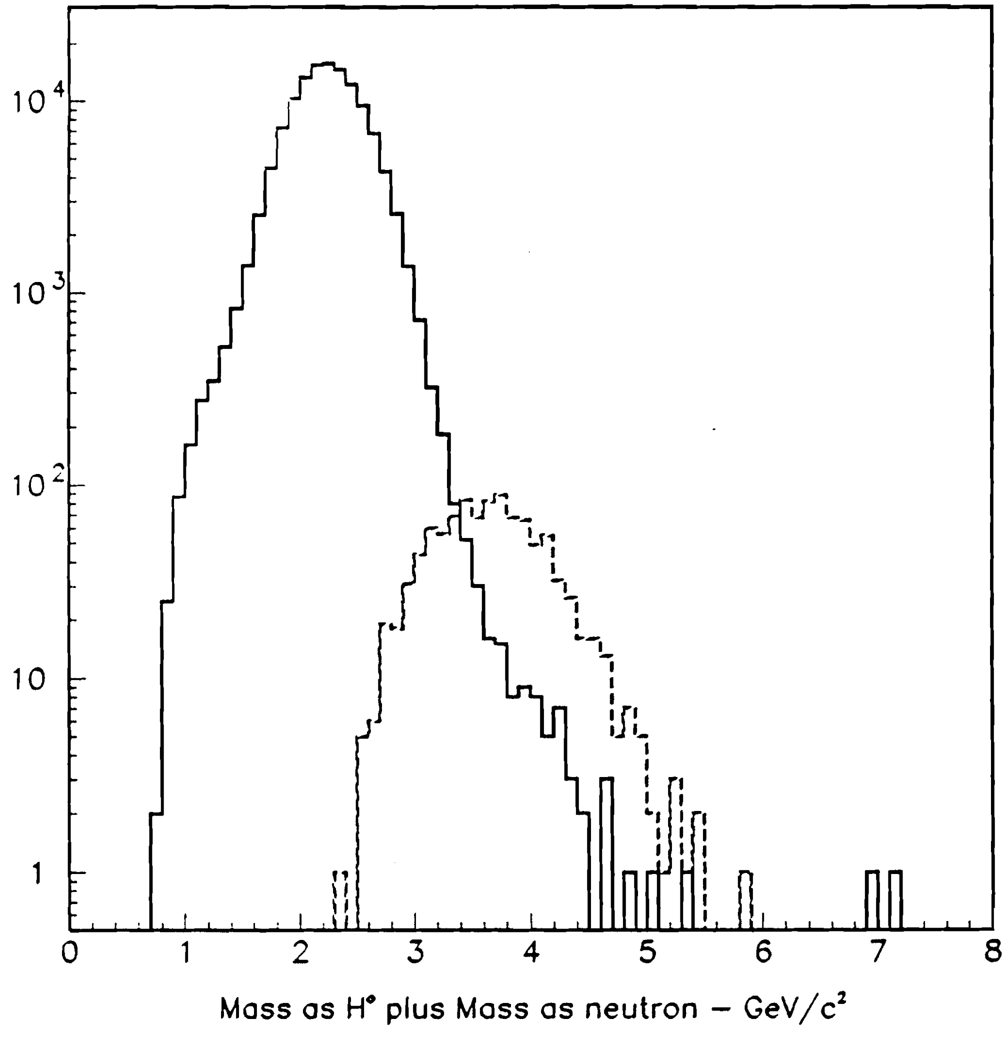

Figure 38: Histogram of sum of the two mass hypotheses (neutron and H°) for neutrons (solid) and H°'s (dashed).

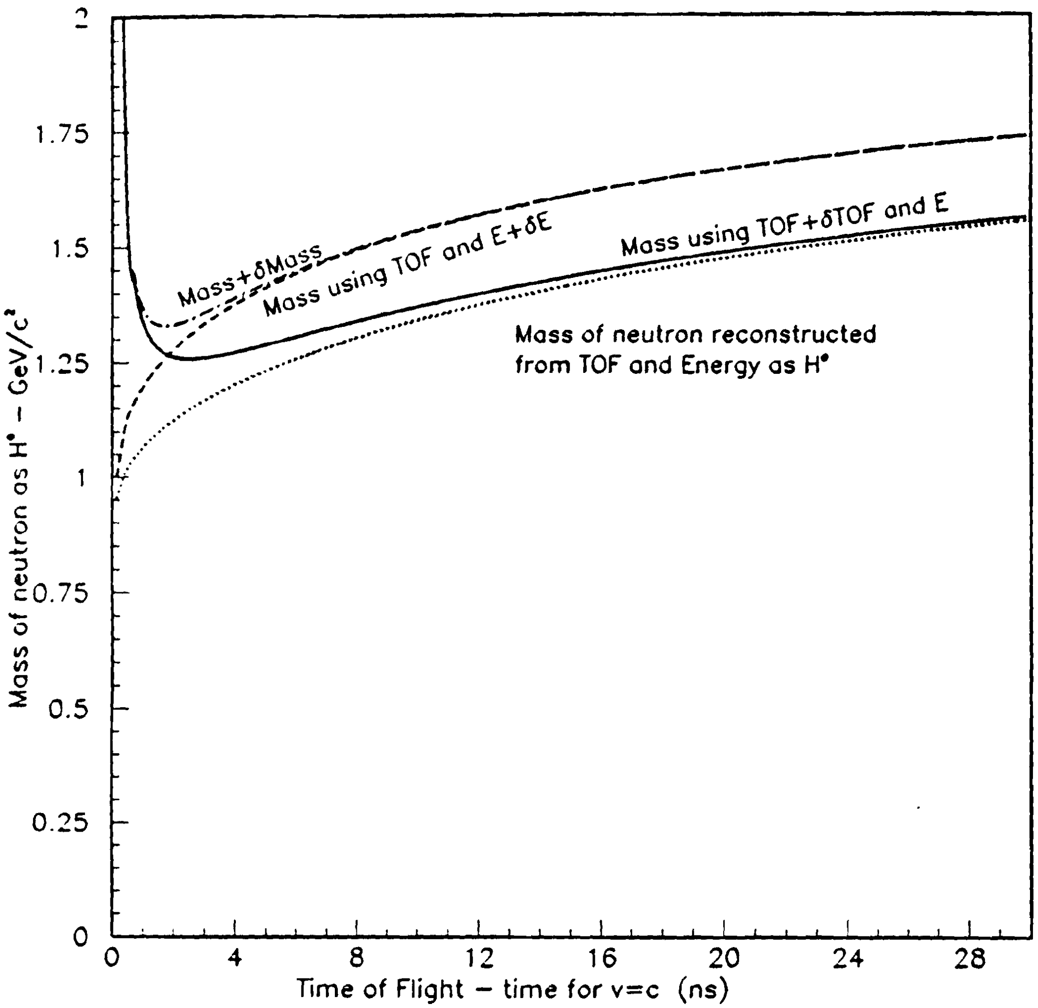

Figure 39: Expected apparent mass of neutrons reconstructed as H^o's as a function of time of flight. Time for a v=c particle is subtracted.

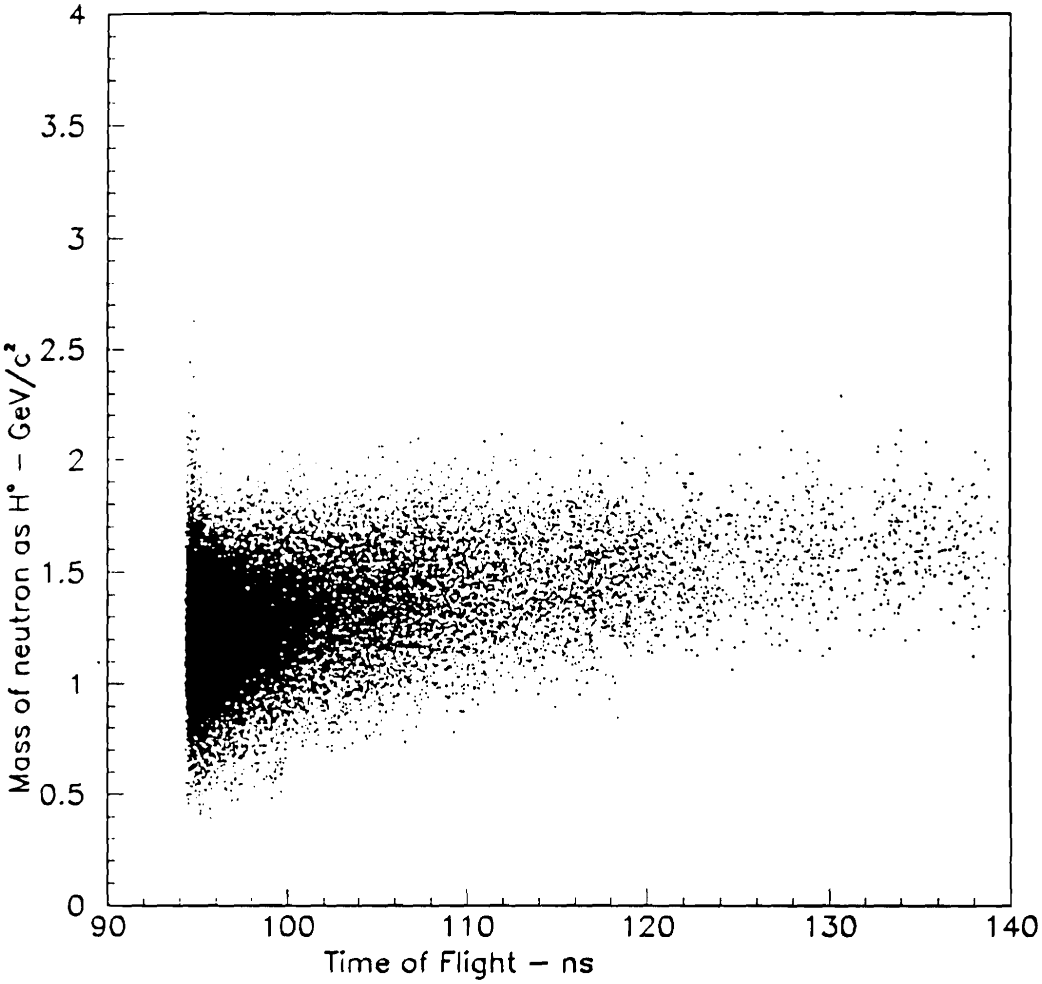

Figure 40: Scatter plot shows the apparent mass of neutrons reconstructed as H^o's vs time of flight.

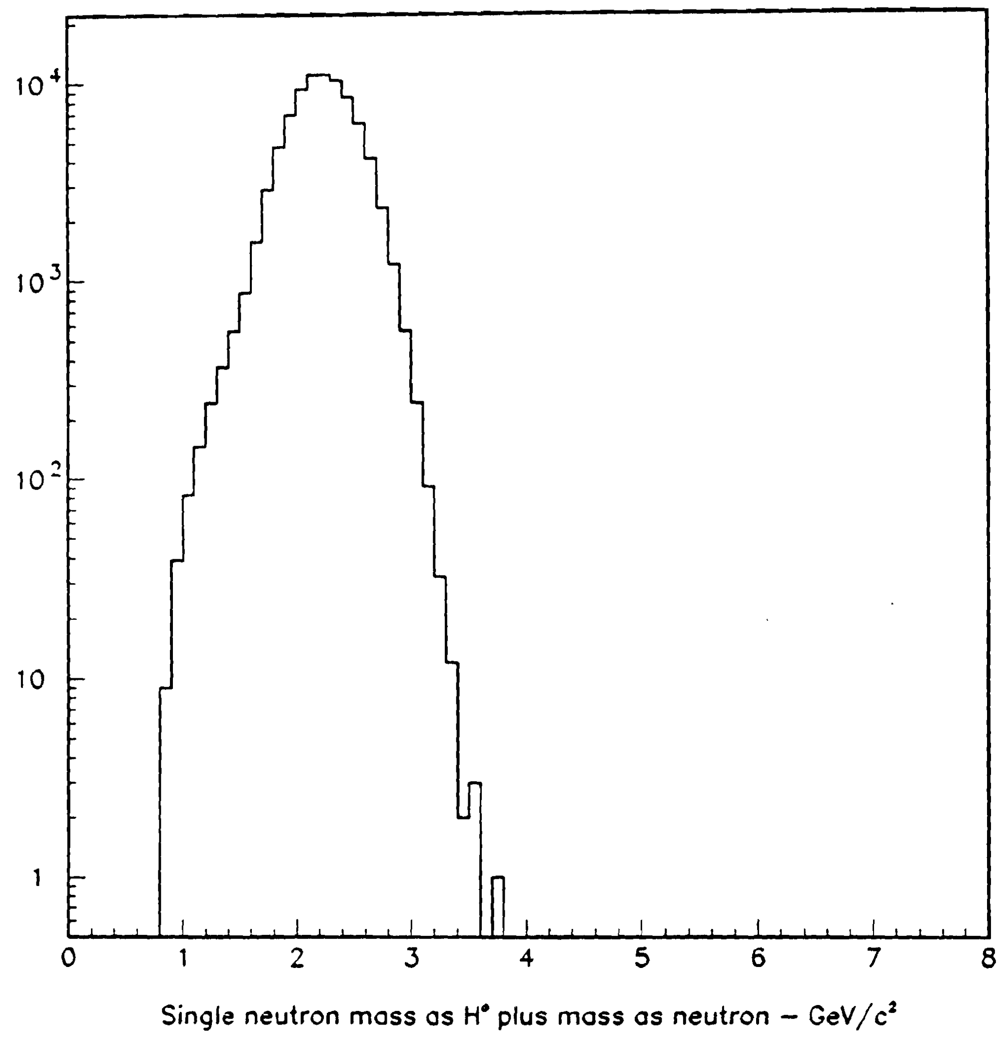

Figure 41: Histogram of the apparent mass of neutrons reconstructed as H°'s. with additional timing cuts.

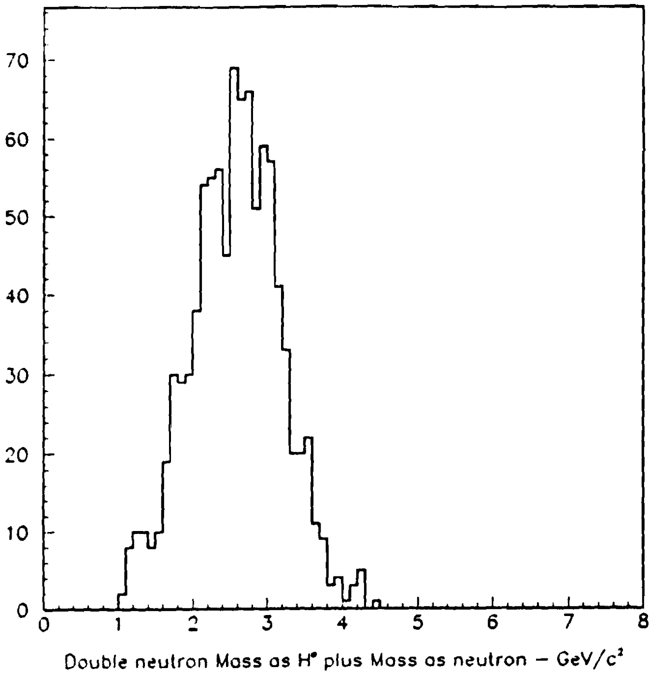

Figure 42: Sum of two mass hypotheses (neutron and H°) for two overlapping neutrons

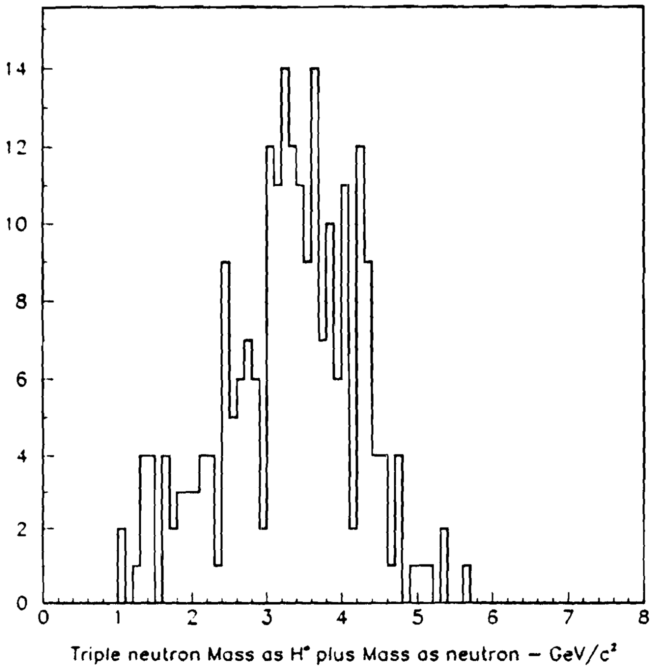

Figure 43: Sum of two mass hypotheses (neutron and H°) for three overlapping neutrons

Table 17: Numbers of events from various sources for a 100 hour run. Calorimeter energy resolution assumed to be $\delta E/E = 0.4/\sqrt{E}$.

Cut on sum of two mass hypotheses	single neutron	double neutron	triple neutron	H^o
no cut	4.48×10^{8}	1.77×10^{6}	21,500	$4.84\times10^{6} \times F_H$
>3.0 GeV/c^2	2.06×10^{6}	365,600	3172	$4.49\times10^{6} \times F_H$
>3.5 GeV/c^2	21500	53,330	1989	$2.94\times10^{6} \times F_H$
>4.0 GeV/c^2	< 5000	7526	1075	$9.34\times10^{5} \times F_H$

Table 18: Numbers of events from various sources for a 100 hour run. Calorimeter energy resolution assumed to be $\delta E/E = 0.3/\sqrt{E}$.

Cut on sum of two mass hypotheses	single neutron	double neutron	H^o
no cut	4.58×10^{8}	1.77×10^{6}	$4.84\times10^{6} \times F_H$
>3.0 GeV/c^2	3.66×10^{5}	322,600	$4.68\times10^{6} \times F_H$
>3.5 GeV/c^2	10,750	38,300	$3.04\times10^{6} \times F_H$
>4.0 GeV/c^2	< 5000	4946	$7.01\times10^{5} \times F_H$

acceptance for neutrals will be the same in each run. Table 17 shows the number of reconstructed neutral showers expected from each source (single neutron, double neutron, triple neutron and H^o) for several different cuts on the sum of the two mass hypotheses (neutron or H^o). The number of H^o's detected is a function of F_H, the production rate of H^o's per central event. The timing cuts described above are used to select these events. The number of double neutron events is calculated assuming that a 4 cm minimum distance is required to identify two neutrons as such and reject them. We have also included an efficiency of 42% for finding good showers which pass shape cuts. From Table 17 we conclude that a statistically significant excess of events ($> 5\sigma$) attributable to the H^o will be observed for H^o production rates as low as 10^{-3} per central event. Table 18 shows the results of the same analysis assuming a calorimeter energy resolution of $\delta E/E = 0.3/\sqrt{E}$. Under this assumption, the signal to noise is somewhat improved for the lowest cut on the summed mass hypotheses so that one would expect to see a statistically significant *mass peak* for H^o production rates as low as 10^{-3} per central event. We also note that our studies show that the triple neutron overlap background is not the dominant background source provided one can eliminate triple neutron clusters where the neutron falling furthest from the energy weighted centroid of the three is at least 10 cm from the centroid.

Another potential background source is due to antineutrons which could be produced in these events. The production rate of the H^o is expected to be comparable to the rate of antineutrons (based on antiproton production data obtained in E802 and E814 for 14.5 GeV Si ions on lead [48, 11]). Monte Carlo calculations presented in the original E864 proposal show that there is considerable overlap between H^o-dibaryons and antineutrons for a large fraction of the kinematic regime of interest. However, E864 will have very high statistics measurements of antiproton production. These measurements will characterize not only the antiproton spectra but also the detector response to antinucleons. With these data we should be able to adequately predict the shape and magnitude of the antineutron background. Given the expectation of similar rates for antineutrons and H^o-dibaryons and the high statistical power of the data sample, we should be able to carry out the H^o search even in the presence of significant antineutron background.

Several comments can be made about our sensitivity to the H^o:

- First, the study above assuming gaussian errors is certainly not adequate to demonstrate the level of rejection required. Particularly for the background due to the tail of single neutrons one must fully understand the resolution. As is described in a following section we are preparing a very detailed simulation of the calorimeter using GEANT. This will give a better estimate of the sensitivity for low mass neutrals, however a reliable estimate can only come from studying the actual calorimeter modules.

- The study above shows that the ability to detect the H^o is critically dependant on the calorimeter resolution. This particular physics goal will be compromised by reduced calorimeter performance.

- A significant part of the power of this experiment to detect the H^o comes from the very large event sample (Tables 17 and 18). With such high statistics, we can afford to use a variety of cuts to enhance the H^o signal. The high statistics also allows observation of a small signal on a large background.

- To maximize our sensitivity to the H^o we will have to use the most sophisticated calorimeter analysis and also have the best possible understanding of the performance of the calorimeter. Although the study presented above makes the simplistic assumption of gaussian errors which may lead to under estimating the background, it also does not take advantage of shape cuts (both in space and time) on the towers involved in a shower. Such cuts should help eliminate multi-particle showers.

For particles of higher mass, the background becomes lower due to the lower likelihood of more than three overlapping neutrons. There is also a greater likelihood of one of the background neutrons revealing a wrong time of flight. For particle masses of about 7 GeV/c^2, we expect that the calorimeter rejection will be comparable to that found in the analysis described for the charged particle case, i.e. a background rate of about 10^{-1} per central event. For masses greater than ≈ 7 GeV, the charged particle analysis ran out of statistics, but given our overlap picture, it is reasonable to expect the background to continue to fall as the mass of interest increases. Extrapolating the background spectrum found in the charged particle case indicates that the background drops by about a factor of 10 for each additional 1.5 baryon masses added. We reiterate that the calorimeter analysis used in the charged particle case was appreciably cruder than that which will be used for the neutral analysis.

4.5 Accidental Backgrounds: Multiple Interactions from Bunched Beam Particles

Beam particles interacting after a triggered event has satisfied the centrality requirement can fake a strangelet's signal if the second interaction occurs within the ADC's gates, and if energy is deposited at the correct position in the calorimeter.

At the trigger level this background can be sufficiently rejected with a simple trigger that utilizes the multiplicity detector with thresholds set much lower than those used to select central interactions; some multiple-beam interactions, however, will be recorded on tape. A conservative estimate of this probability follows. The probability $\mathcal{P}$ can be written as $\mathcal{P} = LF$, where L is the fraction of triggered events with an unvetoed late beam interaction, and F is the fraction of L events which deposit "strangelet-class" energy in the "right place" in the calorimeter.

$$L = (10^{6})(60 \times 10^{-9})(0.05) = 3 \times 10^{-3},$$

where the three terms are the interaction rate (int/sec), gate length (sec), and estimated veto inefficiency, respectively.

$$F = (6.2)(6.6 \times 10^{-4}) = 4.1 \times 10^{-3}.$$

The first term is the number of prompt protons and neutrons in the experimental acceptance per event for interactions which would fail to fire the low threshold multiplicity requirement. These prompt particles are the only abundant particles with "strangelet-class" energies (in the range 5-20 GeV). The second bracketed term is a geometrical factor which accounts for the overlap probability of the showers of a prompt particle from the second event and a candidate particle from the first (triggered) event. The showers are considered to overlap if their centroids fall within 2.5σ of one another, where the standard deviation of the shower centroid is taken from SPACAL data.

The probability of the entire process is therefore $\mathcal{P} = 1/81,000$

The product of the probability $\mathcal{P}$ with the tracking system rejection outlined in Table 16 is below the sensitivity planned for the experiment, and so it should not pose problem in our analysis. There are additionally other event characteristics that could be used to identify this background if the need arises. First, there will be many charged tracks in the spectrometer associated with the "late" interaction. Most of these tracks will be prompt, and they will all point back in time to an interaction which followed the initial triggered interaction. Second, the mass measured by momentum and time-of-flight will disagree with the mass measured by energy and time-of-flight over large windows in TOF, since energy was artificially added to the cluster in question. Third, the calorimeter cluster time-of-flight would only fortuitously agree with the scintillator's timing value since both interactions would be uncorrelated. Last, the calorimeter cluster's time pattern may show the presence of two clusters, one from the first and one from the second interaction.

A variation of this background results from contamination of the heavy ion beam with lighter ions or nucleons. In this situation the second beam interaction is caused by a low-A beam contaminant, and may be difficult for the multiplicity trigger to detect. At some level this will begin to affect E864's ability to achieve the desired sensitivity. Below is an estimate of the interaction rate of beam protons that will be tolerable.

The experiment plans to have a rejection of 9.7×10^{-12}, so it would be safe if this background occurred at the 1×10^{-12} level. Since the rejection of the tracking system is 1.94×10^{-7}, the multiple-beam background due to low-A beam protons would have to occur at most every $1.94 \times 10^{-7}/1 \times 10^{-12} = 194,000$ interactions. Thus $\mathcal{P} = 1/194,000 = LF$, where the variables have the same meaning as above. Some of the numbers which make up L and F will change because a single nucleon is responsible for the second interaction:

- Let the interaction rate of protons be I

- The 60 ns gate is unchanged.
- The 5% trigger inefficiency will be much higher, since the multiplicity in *p*–*A* events is much less than *A*–*A* events. To be safe, assume that the multiplicity trigger misses *all p*–*A* interactions, so the inefficiency is 1.0.
- The multiplicity of prompt nucleons per event will be less for *p*–*A* than for *A*–*A* collisions. From Ref. [63], it is evident that 0.2 protons per event are produced within 1 unit of the beam's rapidity in *p*–Pb collisions at 19.2 GeV/c. If we conservatively assume that *all* these track into the E864 spectrometer, and that the number of neutrons is twice the number of protons, then there would be a maximum of 0.6 nucleons/event with "strangelet-class energies" in the spectrometer due to a proton collision.
- The geometrical factor is unchanged.

Therefore,

$$\mathcal{P} = 1/194,000 = I(60 \times 10^{-9})(0.6)(6.6 \times 10^{-4})$$

$$I = 216,946$$

In other words, the experiment could conservatively tolerate as many as 217,000 proton interactions per second before they would be a problem as multiple-beam interactions. If our Au target is a 10% target for a Au beam, then it is a $10\%(1^{\frac{1}{3}} + 197^{\frac{1}{3}})^2/(197^{\frac{1}{3}} + 197^{\frac{1}{3}})^2 = 3.43\%$ target for proton collisions. The 217,000 *p*–Au interactions would thus correspond to 6.3×10^6 protons per second. This flux is 6/10 that of the Au beam itself.

4.6 Other Backgrounds

As indicated above, the most likely sources of background are those which produce a real slow track in the apparatus which did not come from the target. If this track has the right direction, it could be interpreted as a high rigidity (hence high mass) track from the target. If this track also points to a region of the calorimeter where coincidentally neutral particles have deposited substantial energy in the correct place with the correct time and energy, then the track could simulate a high mass object. Although such multiple overlapping processes are highly unlikely, if we want a sensitivity of order 10^{-11} such processes must be considered. We have given a detailed analysis of interactions in the upstream detectors above. Here we consider a decay process.

If a centrally-produced Λ^o travels through a significant part of the magnetic field and then decays, the decay proton will have a similar velocity and direction to the parent Λ^o. However the decay proton will not have been bent in the magnetic field by a large enough angle (corresponding to its low momentum) and thus will appear to be a track with higher momentum and hence higher mass. Since the Λ^o and the proton have similar velocities and directions and the Λ^o is centrally produced, the proton track can otherwise appear to be a good late track coming from the target in space and time.

In order to produce a proton that reconstructs as a high mass particle the Λ^o must pass through most of the magnetic field before decaying. In particular, Λ^o's which survive to the end of the first magnet but decay before the second magnet will only give protons that reconstruct to about three times the proton mass. To get masses as high as 10 GeV/c^2, which would be a background for the strangelet search, the Λ^o would have to survive more than 2/3 of the way through the second magnet or more than 7.5m from the target. Figure 44 shows the proton kinematics from Λ^o decay. The maximum rapidity of interest is 1.89, corresponding to a 3.02 GeV proton. From Fig. 44 one can see that the maximum momentum for a Λ^o which can produce such a proton is less than 4 GeV. For a 4 GeV Λ^o the decay distance is $\gamma c\tau$=0.294m. The probability to survive 7.5m or 25.5 lifetimes is less than 10^{-11}. Thus even without requiring any suppression from the calorimeter (the proton energy is wrong for a high mass particle by a large factor) or from the fact that there is no confirming hit in S1, this process is not a background.

We have also considered possible backgrounds due to neutrons and protons from electromagnetic dissociation and due to nuclear fragments. Neither of these represent a significant background source. Coulomb dissociation products are very peripheral in nature, hence they have the wrong velocity (beam rapidity) and very low $P_\perp$ so that they do not get into our apparatus. Heavy nuclear fragments have a low production cross section and tend to be produced at beam rapidity so they also pose no problem for this experiment. The details of both of these calculations are available in "Update to P-864: Production of Rare Composite Objects in Relativistic Heavy Ion Collisions," October 1, 1990.

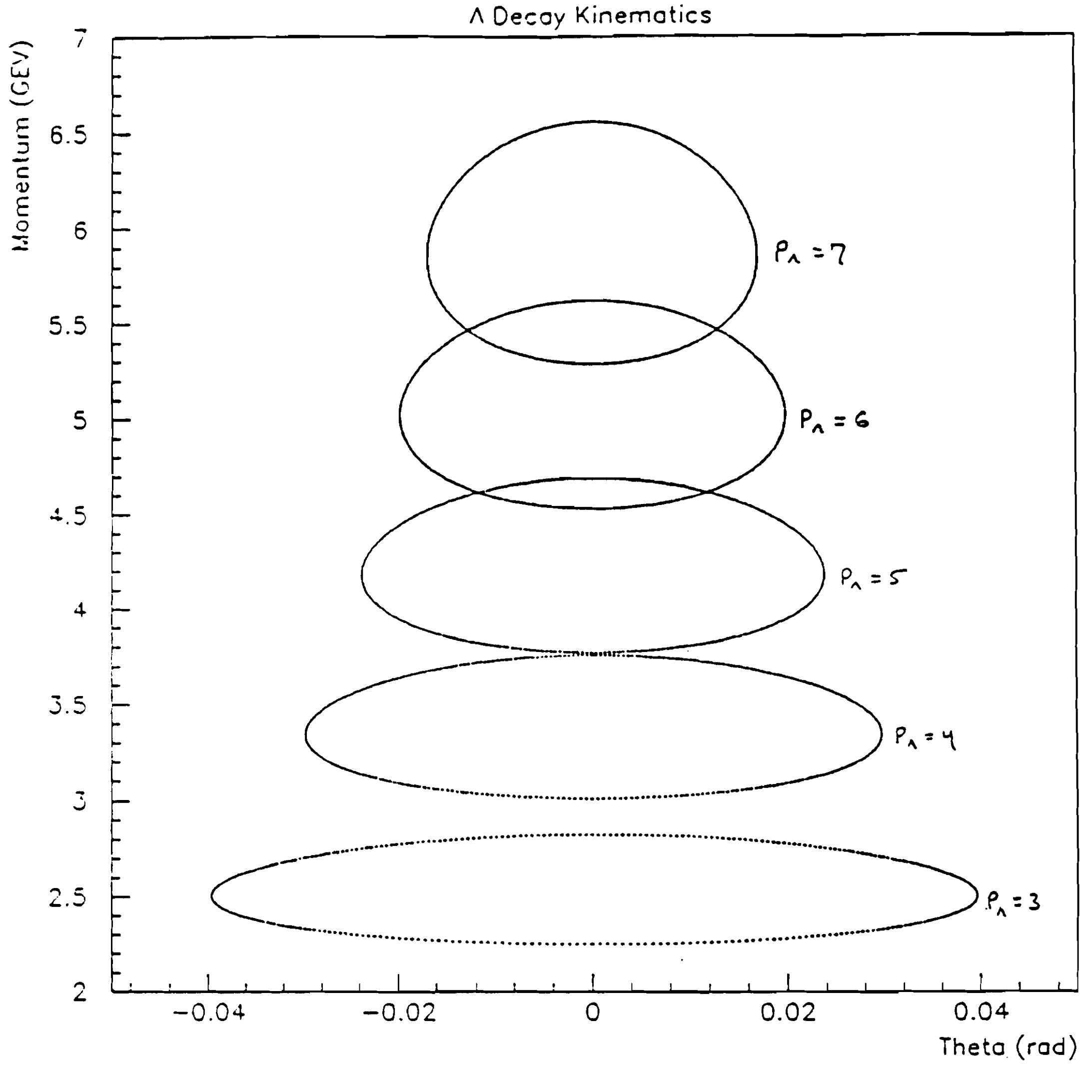

Figure 44: Λ^0 decay kinematics. Horizontal axis (Theta) is lab. angle of proton with respect to Λ^0 direction and vertical axis is proton lab. momentum.

5 Summary of Run Plans, Rates and Sensitivities

5.1 General

As discussed in the section on the trigger, we plan to use two different running modes. One mode, using only a centrality trigger and lower beam rates and/or a thinner target, will acquire data on the more abundant low mass systems. These runs can be done with a target as thin as 4% and beam rates of order 10^6 per spill or less. The other mode, using the centrality trigger, a late energy requirement from the calorimeter, a 20% target and the full beam rate of 10^7 per spill, will be used for high sensitivity searches for high mass systems. In the sections below we will describe the four main runs planned (one of each trigger type with positive and negative magnetic field settings) and draw together the rates, acceptance and efficiencies discussed in other sections to calculate the sensitivities which can be achieved in each running mode.

The four runs are:

- Run A ($Z/A \simeq 0.5$): 100 hours, B=+0.75T, multiplicity trigger only - central production of normal nuclei.
- Run B ($Z/A \simeq -1.0$): 100 hours, B=−0.45T, multiplicity trigger only - chiral soliton search.
- Run C ($Z/A \simeq 0.1 - 0.3$): 1200 hours, B=+1.5T, multiplicity and late energy trigger - positive strangelet search.
- Run D ($Z/A \simeq -0.1 - -0.67$): 1000 hours, B=−0.75T, multiplicity and late energy trigger - anti-nuclei study and negative strangelet search.

In the sections below we tabulate the systems to be studied in each of these runs. We note that the acceptance of the apparatus is large enough to be sensitive to neutrals in all the proposed runs. Since the metrology and backgrounds are very different for neutrals, the rates and sensitivities will be discussed separately.

5.2 Run A ($Z/A \simeq 0.5$)

The field in both spectrometer magnets will be set to +0.75T to optimize acceptance for species with $Z/A = +1/2$. The primary physics emphasis in this run is to study

Table 19: Centrally produced composites studied in Run A

Composite system	Z/A
d	.5
t	.333
^{3}He	.667
^{4}He	.5
^{6}He	.333
^{6}Li	.5
^{7}Li	.429
^{7}Be	.571
^{7}B	.714
^{8}He	.25
^{8}Li	.375
^{8}B	.5
H^{0}	neutral
$H^{0}-d$	.26

the central production of nuclei. This will help to understand the dynamics involved in producing composite systems. The species to be studied in this run are listed in Table 19. The positive value of the field means that the magnet is set to deflect positive particles into the experimental acceptance. With the multiplicity trigger only it is possible even with modest beam rate to saturate the DA system rate of 4000 events per spill. In 100 (calendar) hours, assuming an AGS macro duty cycle of 20%, a total of 2.88×10^{8} central collisions will be recorded.

The acceptance times efficiency of the apparatus for the positive nuclei listed in the table is about 4%. (See Table 12.) The efficiency of the calorimeter, as discussed in the section on the calorimeter simulation, is 42%. We note that there is no live time correction here since the 4000 events per spill is DA limited.

Thus, the species studied in this run will be detected at a sensitivity of one event per:

$$2.88 \times 10^{8} \times 10 \text{ (trigger on 10\% of total interactions)}$$

$$\times\ .04 \text{ (tracking efficiency } \times \text{ acceptance)} \times 0.42 \text{ (calorimeter efficiency)}$$

$$= 4.83 \times 10^{7} \text{ collisions}$$

For the more abundant species and species with charge greater than 1 where use of the calorimeter is probably not necessary this number will double. We note that the

Table 20: Centrally produced composites studied in Run B

Composite System	Mass (GeV/c^2)	Z/M
$\Sigma^-\Sigma^-$	2.39	.835
$\Sigma^-\Xi^-$	2.52	.794
$\Xi^-\Xi^-$	2.64	.757
$\Xi^-\Omega^-$	2.99	.669
$\Omega^-\Omega^-$	3.34	.598
H^0	2.0	neutral

typical rate for mass 8 nuclei predicted by a thermodynamic model is around 10^{-5} per central collision. This would give about 50 reconstructed particles for a mass 8 nucleus in this run.

We note that we can also search for the composite charged $H^0 - d$ system in Run A. The yield of H^0 in 14.5 Gev/c Si ions on Au has been estimated to be 10^{-2}-10^{-3} per central collision. This would surely be higher for Au-Au collisions. We know that deuterons are "plentiful" so that our sensitivity of 2×10^{-8} per collision would appear to be significant.

5.3 Run B (Z/A$\simeq -1.0$)

In this run, the magnet is set to $-.45$T to be sensitive to the possible chiral soliton states discussed in the section on physics goals. The sensitivity is the same as calculated for Run A. With the field at $-.45$T, the acceptance times efficiency for the range of Z/A covered by the postulated chiral soliton states ranges from 3% to 6% which is about the same as the acceptance for the positive nuclei of Run A with the field set to 0.75T. Thus these states will have a search limit of 5×10^{-8} per collision at the 90% confidence level. This run will also collect a very large sample of data on antiproton production.

Table 20 lists the composites studied in Run B.

5.4 Run C (Z/A$\simeq 0.1 - 0.3$)

Run C, with the magnetic field set to +1.5T, is designed to be a high sensitivity search for strangelets with Z/A in the range .1 to .3 and to measure the yields of positive nuclei with $Z/A \sim .3$. This run also will be sensitive to the $H^0 - H^0$

Table 21: Centrally produced composites studied in Run C

Composite System	Z/M
Strangelets	.1 to .3
^{8}He	.25
^{11}Be	.286
^{17}B	.294
^{19}B	.263
$H^0 - H^0$	neutral

composite. Table 21 summarizes the systems studied in Run C.

Adding the late energy requirement to the trigger will allow us to run at the full beam rate with a 20% target. If the trigger rate is as high as 4000 per beam spill this will give a 20% deadtime. From Table 12 the tracking efficiency times acceptance for strangelets is about 10%. For a 1200 hour run this will give a sensitivity of one event per:

$$2.0 \times 10^{6} \text{ (interactions rate)}$$

$$\times 0.1 \text{ (tracking efficiency } \times \text{ acceptance)} \times .42 \text{ (calorimeter efficiency)}$$

$$\times 1200 \text{ hours} \times 900 \text{ beam spills per hour} \times 0.8 \text{ live time}$$

$$= 7.25 \times 10^{10} \text{ collisions}$$

This gives a 90% confidence level of 3.17×10^{-11} of all interactions.

5.5 Run D (Z/A$\simeq -0.1 - -0.67$)

Run D is designed to measure the yields of antinuclei produced in these collisions and to search for negative strangelets. The magnet will be set to −0.75T so as to have a good acceptance for the $\bar{d}$, $\bar{t}$, $\overline{^{3}He}$ systems. This run is also sensitive to $H^0 - H^0$ composite.

Since the range of Z/A we wish to cover in this run is larger than for the positive strangelet runs (from 0.1 to 0.67 for this run), the acceptance for some species is less. As seen in Table 12 the acceptance times efficiency for $\overline{^{3}He}$ drops to 3.4%. For negative strangelets the acceptance remains comparable to that for positive strangelets. We note however that the total flux of particles through the apparatus is less in the negative running so that we believe we can increase the interaction rate by up to a factor of three. This would give a sensitivity for the negative

Table 22: Centrally produced composites studied in Run D

Composite System	Z/M
$\bar{d}$	$-.5$
$\bar{t}$	$-.33$
$\overline{^3He}$	$-.67$
Strangelets	$-.1$ to $-.5$
$H^0 - H^0$	neutral

strangelet search of 1.3×10^{-11} of all interactions and for antinuclei of 3.8×10^{-11} of all interactions (90% confidence level).

5.6 Rates and Sensitivities for Neutrals

As noted above, the apparatus is large enough to have sensitivity to neutral states for all the runs listed above. Runs A and B, which use only the multiplicity trigger, will be sensitive to all masses. Runs C and D, which use the late energy trigger, will not have full sensitivity for low masses such as the H^0, but will have full statistical sensitivity for higher mass states. Without the rejection from the tracking system, it is expected that the sensitivity for neutrals will be limited by background. The background is expected to fall as the mass increases. We have shown above that in the mass region of the H^0 dibaryon searches at the level of 10−3 per central interaction should be possible. For higher masses, the background falls by about one order of magnitude per 1.5 GeV/c^2 of increased mass.

5.7 Analysis

We comment here on the analysis required for the data samples discussed above. Potentially the largest sample will be the 1200 hour run for the positive strangelet search. If the trigger is sufficiently loose so as to saturate the DA system (a situation we do not expect), then the run could produce:

1200 hours × 900 beam spills per hour × 4000 events per spill $=$ 4.32×10^9events

The analysis programs used to study the Monte Carlo data discussed above do not have to deal with the full complexity of the detector, since our simulation is still evolving. However we have made a very realistic simulation of the scintillation counter hodoscopes and, as discussed in the section on the simulations, the hodoscopes form the basis for the pattern recognition. Currently, the full tracking analysis for events with a HIJET central interaction, tracks from interactions in the shielding and a strangelet takes 0.215 seconds per event on a VAXstation 3100 M76 (9 VUP's). To do only the hodoscope pattern recognition takes 0.105 seconds per event on the same machine. Since the hodoscope tracks give the velocity measurement and a mass measurement good to about 10% ($\Delta M/M$) we will be able to reject most events with only the hodoscope tracking. This means that the main data reduction for the 1200 hour run will not take more than 13.7 VAXstation 3100 M76 years. On the CPU power currently available in the collaboration this would take about one calendar year. We fully expect that the current rate of evolution of CPU power will allow us to have a least a factor of four more CPU power available by the time this experiment has data. Further, the first runs will most likely not be the long high sensitivity runs. By the time that analysis is required it is reasonable to expect that it should not take more than a few months calendar time on the CPU power available in the collaboration. Thus we do not see a need for major expenditures for specialized processing for this experiment. We also note that the currently available storage medium of choice (8mm tapes) will hold about 5×10^5 events each. At 0.1 sec per event this means a VAXstation 3100 M76 will take about 14 hours to process one tape. At full transfer rate the 8mm tape drives can read an entire tape in 2 to 2.5 hours. Thus even with processors 5-7 times faster, the analysis will still be CPU bound so new technology is not needed to match the data storage medium to the processing speed. Of course we will take advantage of any appropriate improvements in storage technology that become available.

6 Progress of Detector Development and Prototypes

6.1 Overview

Below we discuss our progress on designing the various detector systems. We also present plans and costs for prototype construction and tests, plans, and schedules for completion of the design and construction of the detectors. Costs for the full apparatus are presented in Section 7.

6.2 Scintillation Counter Hodoscopes

6.2.1 Introduction

The Yale group from the Wright Nuclear Structure Laboratory (WNSL) has assumed primary responsibility for the design and construction of the three TOF hodoscope stations. Within this project are four main efforts: design, fabrication, and testing of the individual hodoscope counters; photomultiplier high voltage supplies, control and readout; online calibration and monitoring system; and mechanical support structure. Within WNSL, excellent mechanical and technical support facilities (machine shop, electronics shop, technicians, engineers, CAD, etc.) are available for each of these efforts.

In Section 3.2.2 we discussed the design considerations driving the required granularity and timing characteristics of the scintillator hodoscopes. In this section we present a status report of the ongoing development efforts aimed towards the appropriate selection of detector components (e.g. scintillator, light guides, photomultiplier tubes, calibration system, readout electronics, etc.) which will allow the design goal of 200 ps RMS timing resolution to be met. Because the hodoscopes are the heart of the pattern recognition for charged particle tracking (see Section 4.3.1), it is imperative that the design goal of 200 ps timing resolution be met and maintained over the lifetime of the experiment. For this reason we are trying to exceed this design goal in our prototypes so as to provide adequate safety margin in the event of technical difficulties in actual operation.

6.2.2 Current Development and Prototypes

A time of flight (TOF) development effort has been initiated to assess the performance of various detector components planned for the E864 TOF hodoscopes. The immediate goal of these efforts has been to select a scintillator - photomultiplier combination which will deliver the desired timing resolution at a reasonable cost. Three types of plastic scintillator and two types of photomultiplier tubes (PMT's) were evaluated in these tests. A few characteristics of these scintillators and PMT's are summarized in Tables 23 and 24. The range of sizes and types of scintillators studied are listed in Table 25. Timing resolution was studied as function of scintillator size and type, PMT high voltage, dynode voltage ratio, discriminator threshold and source position.

Tests were performed using either cosmic ray muons or a ^{207}Bi source, which yields 1.0 MeV mono-energetic electrons. A schematic drawing of the test apparatus is shown in Fig. 45. As a trigger, a triple coincidence was formed between TRIGA, PMTA and PMTB. The trigger logic was such that the time-to- amplitude converters (TAC's) for PMTA and PMTB received a common start initiated by TRIGA. Each TAC was stopped by the respective logic signal generated by the discriminated PMTA and PMTB pulses. TRIGB could not be included in the trigger for the ^{207}Bi source tests since the 1.0 MeV electrons are stopped in the test scintillator. In the tests using cosmic rays, the trigger rate was sufficiently small that any TRIGB requirements could be made off-line if desired.

To determine the timing resolution of the PMT-scintillator combinations, time spectra were gathered corresponding to the time differences between TRIGA and PMTA and PMTB. The measured time interval for each channel, TOFA and TOFB, was corrected for slewing based on the ADC information recorded for each signal. The slewing corrections were determined by fitting the raw spectra to the functional form:

$$TOF_{cor} = A + \frac{B}{\sqrt{Q}}$$

where Q is the integrated charge recorded by the ADC. Figure 46 shows an example of the raw and slew-corrected time spectra obtained. Only the difference between the actual recorded time interval and TOF_{cor} is plotted. As can be seen, this procedure

Type	Relative Output % anthracene	Rise Time (ns)	Relative Cost
BC404	0.68	0.7	1.3
BC408	0.64	0.9	1.0
BC420	0.64	0.5	2.7

Table 23: Summary of test scintillator specifications.

PMT	Diameter	Window	Rise Time (ns)	T.T.S. (ns)
R1635	3/8"	Borosilicate	0.8	0.7
R3478	3/4"	Borosilicate	1.3	0.4

Table 24: Summary of test PMT specifications.

Reference Name	Size (cm^3)	Type
5L1-404	0.5 x 1.1 x 33.8	BC404
5L1-408	0.5 x 1.1 x 33.8	BC408
5L1-420	0.5 x 1.1 x 33.8	BC420
0L1-404	1.0 x 1.1 x 33.8	BC404
0L1-408	1.0 x 1.1 x 33.8	BC408
5L2-404	0.5 x 1.1 x 39.9	BC404
5L2-408	0.5 x 1.1 x 39.9	BC408
0L2-404	1.0 x 1.1 x 39.9	BC404
0L2-408	1.0 x 1.1 x 39.9	BC408
5L3-404	0.5 x 1.1 x 59.0	BC404
5L3-408	0.5 x 1.1 x 59.0	BC408
0L3-404	1.0 x 1.1 x 59.0	BC404
0L3-408	1.0 x 1.1 x 59.0	BC408
0L3-420	1.0 x 1.1 x 59.0	BC420

Table 25: Sizes and types of scintillators tested.

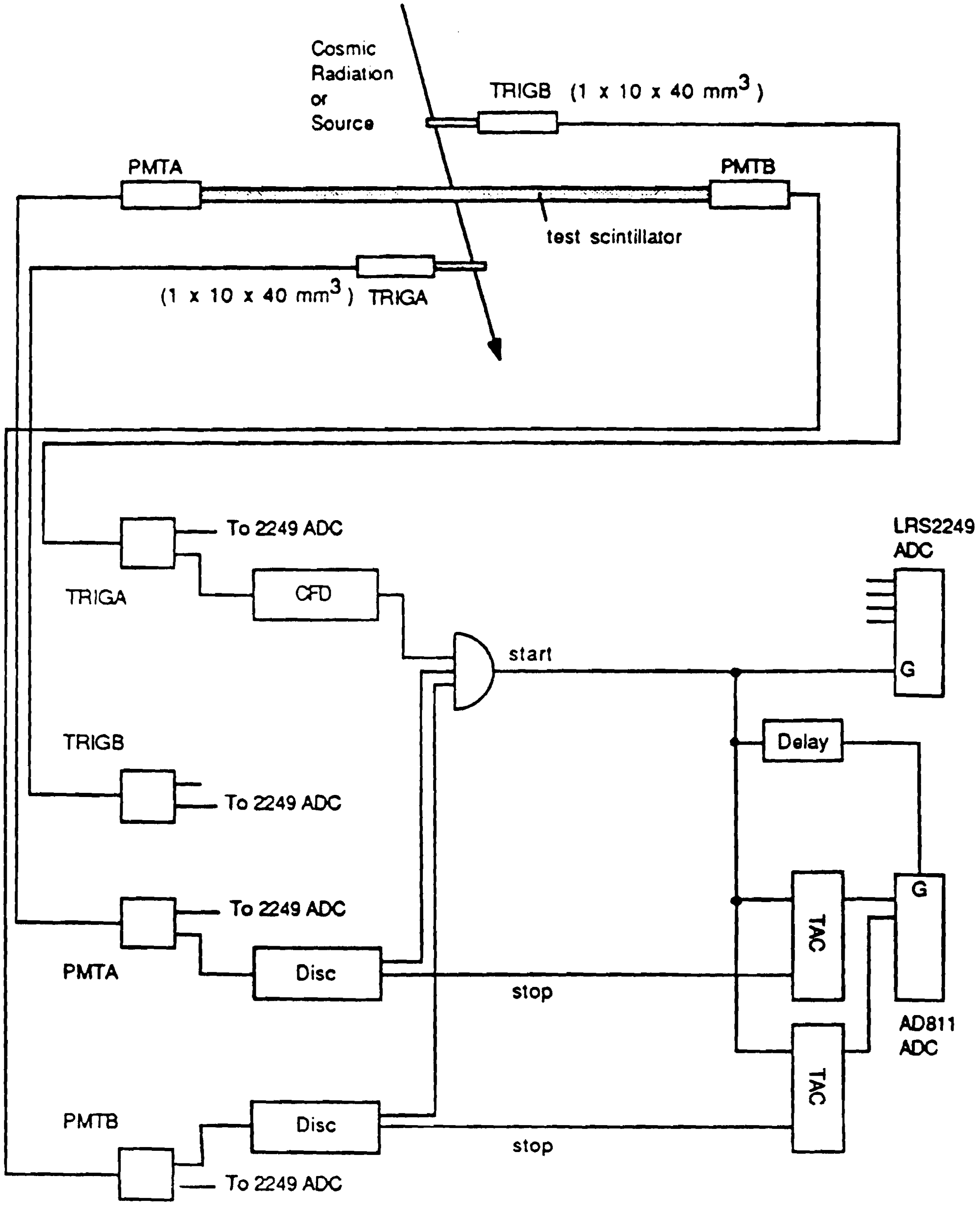

Figure 45: Schematic of the experimental apparatus used in the TOF tests.

largely removes any dependence of the recorded time on pulse height.

The width of the TOFA and TOFB distributions include contributions from timing jitter in the start counter as well as jitter in the PMTA and PMTB channels themselves. For these tests, the timing resolution of the start counter TRIGA was rather poor, being in the neighborhood of 140 → 160 ps. This was due in part to the PMT used for TRIGA. To exclude the contribution of the start counter to the measured widths of the time spectra, the time difference, DELTOF, between TOFA and TOFB was used to quantify the timing performance in each test. Assuming that the time jitter in each channel is statistically independent and that the timing resolution for PMTA and PMTB are equal, the intrinsic time jitter of either channel should be smaller than that of DELTOF by a factor $\sqrt{2}$. Independent of the assumption of equal time resolution for each channel, the jitter on the mean time, defined as $\frac{(TOFA+TOFB)}{2}$, will be one half that of DELTOF.

Proceeding in this manner, a number of tests were performed on various scintillator - PMT combinations. Unless otherwise noted, the numbers given refer to the implied mean time resolution ($= \frac{\sigma_{DELTOF}}{2}$) for the hodoscope element as determined by the measured DELTOF resolution.

Figure 47 shows the relative timing performance as a function of operating voltage of the two photomultiplier tubes considered. Since the two PMT's have different maximum operating potentials (-1500 V and -1800 V for the R1635 and R3478, respectively), they are compared as a function of the fraction of their recommended maximum operating voltage. As can be seen, the timing resolution obtained using the R3478 is better by approximately a factor of 1.4.

A study of the timing characteristics of the R3478 was made as a function of the magnitude of the applied high voltage and discriminator threshold. These results are shown in Fig. 48. For the 5L1-404 scintillator tested, the timing resolution appears to be rather insensitive to the operating voltage over the range examined, but degrades by about 15% when the magnitude of the threshold was changed from 25 to 100 mV.

The behavior of the timing resolution of the R3478 was further investigated as a function of the voltage ratio applied to the dynodes of the PMT. To obtain the best timing resolution, the voltage difference between the photocathode and the first dynode is typically made several times the voltage difference between subsequent dynodes to reduce jitter in the electron transit time. In an attempt to optimize the timing performance of the R3478, the resolution was studied as a function of the voltage difference between the photocathode and the first dynode, for a fixed operating potential. This was achieved by varying the resistance of the first stage in the voltage divider of the PMT base. Figure 49 shows the behavior of the time

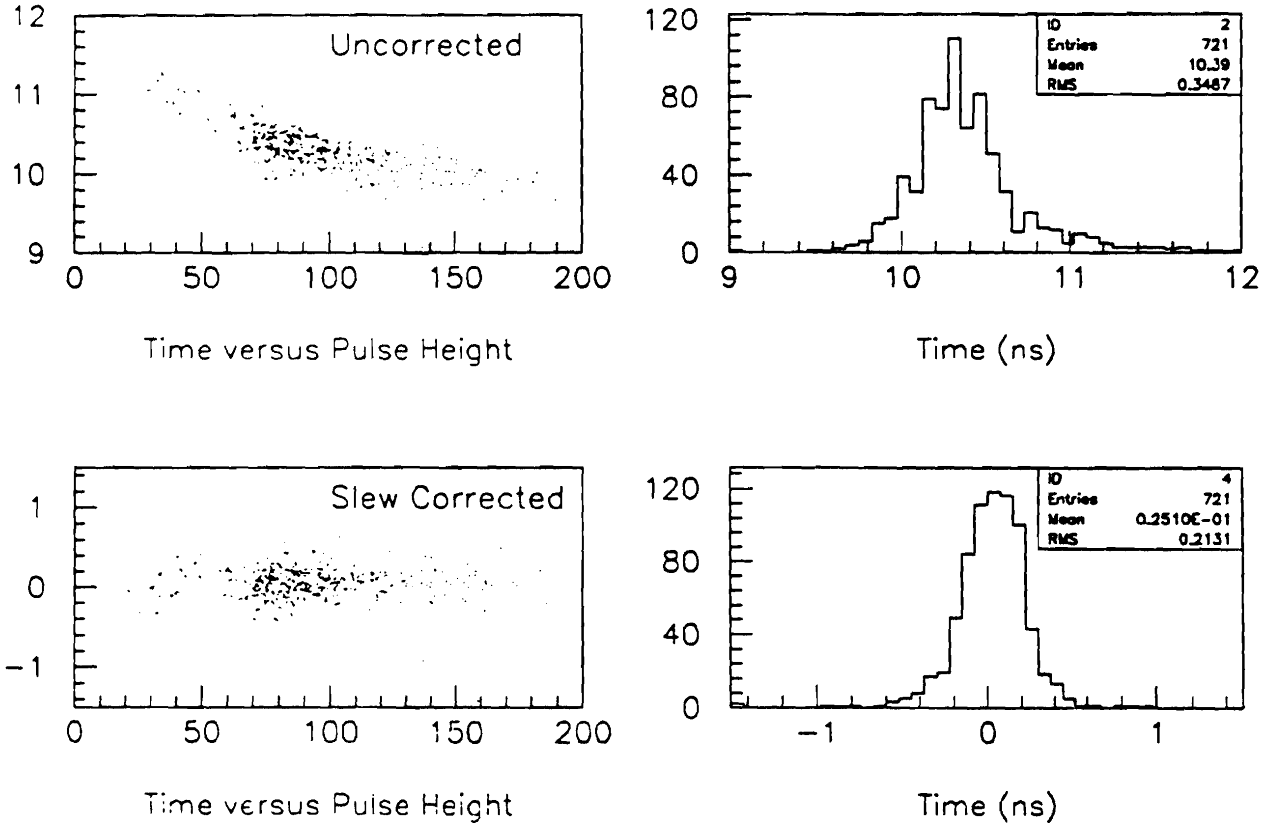

Figure 46: Recorded time (ns) versus pulse height (arbitrary units) for (top) raw and (bottom) slew-corrected time spectra. Also shown is the projection of the data onto the time axis for each plot.

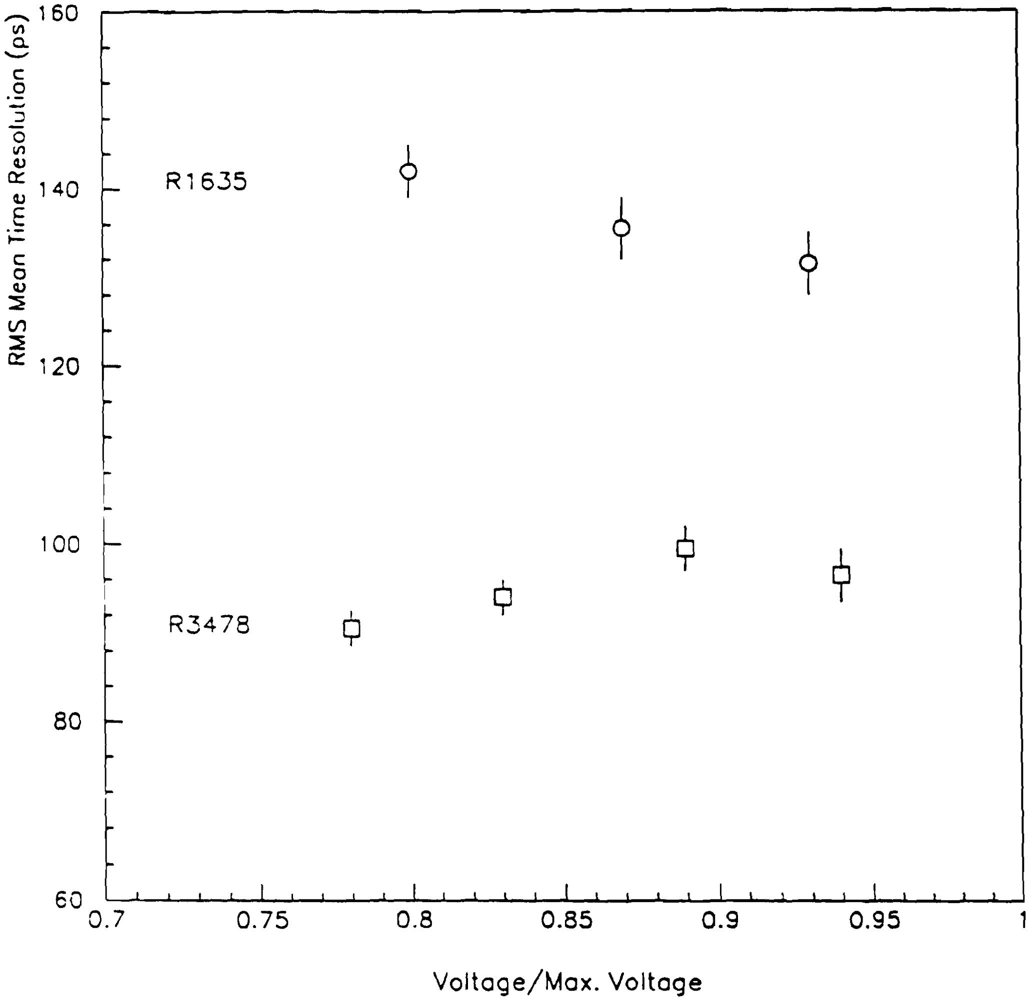

Figure 47: Relative timing characteristics of the Hamamatsu R1635 and R3478 photomultiplier tubes using the 5L1-408 scintillator and a ^{207}Bi source.

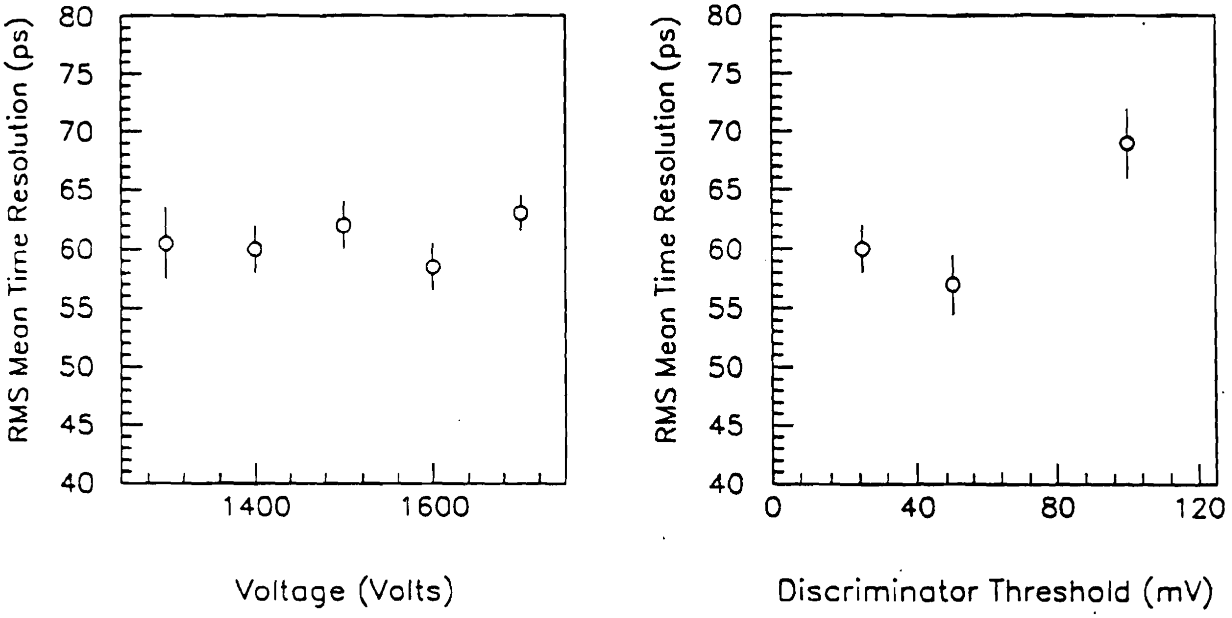

Figure 48: Relative timing characteristics of the Hamamatsu R3478 photomultiplier tube as a function of (a) operating voltage (discriminator = -25 mV) and (b) discriminator threshold (HV = -1400 V). For this test, the 5L1-404 scintillator was used with a cosmic ray source.

	BC404	BC408	BC420
5L1	62 ± 2 ps	66 ± 2 ps	65 ± 5 ps
0L1	47 ± 2 ps	53 ± 3 ps	not tested
5L2	66 ± 2 ps		not tested
0L2	49 ± 2 ps	59 ± 2 ps	not tested
5L3	82 ± 2 ps	crazed	not tested
0L3	57 ± 2 ps	68 ± 3 ps	59 ± 2 ps

Table 26: Mean time resolution (RMS) for various sizes and types of scintillators tested with cosmic rays.

resolution measured as a function of this resistance. Based on these measurements, it appears that the factory recommended voltage distribution ratio of 7:1:1.5:1:1:1:1:1 (corresponding to a cathode - first dynode resistor value of 1.68 MΩ) is nearly optimal for our timing purposes.

Having clearly established the photomultiplier of choice, a number of tests were performed to investigate the relative timing properties of the various scintillator sizes and types under consideration. The mean time resolution determined for each scintillator size and type tested with cosmic rays is listed in Table 26. A subset of these results is shown in Fig. 50.

Finally, a study of detector timing resolution as a function of position along the scintillator was performed. For this test, the trigger scintillators were positioned at various distances measured from the PMTA end of the 5L3-404 scintillator. The timing resolution, shown in Fig. 51, demonstrated a very slight (5 ± 3 %) degradation as the trigger scintillator position was moved from PMTA to PMTB.

As described above, our TOF tests demonstrate that for the 3 hodoscope stations we should be able to achieve mean time resolution for minimum ionizing particles in the neighborhood of 60 - 80 ps using R3478 photomultiplier tubes and almost any of the scintillator types considered. Assuming a timing resolution of 50 ps for the trigger counter which will be used in the actual experiment, it is possible that we can build a time-of-flight measurement system of the size and granularity required for E864 with intrinsic time resolution in the neighborhood of 80 $\longrightarrow$ 100 ps. Such resolution will be degraded in the actual operating environment of the detectors, e.g. due to dispersive losses in the signal cables, but is still expected to be superior to the 200 ps resolution proposed for the experiment. The resolution will also be affected by the required addition of light guides. We plan to design and test appropriate light guide - scintillator combinations in the near future but anticipate that such light guides will not drastically degrade the timing abilities of the proposed TOF

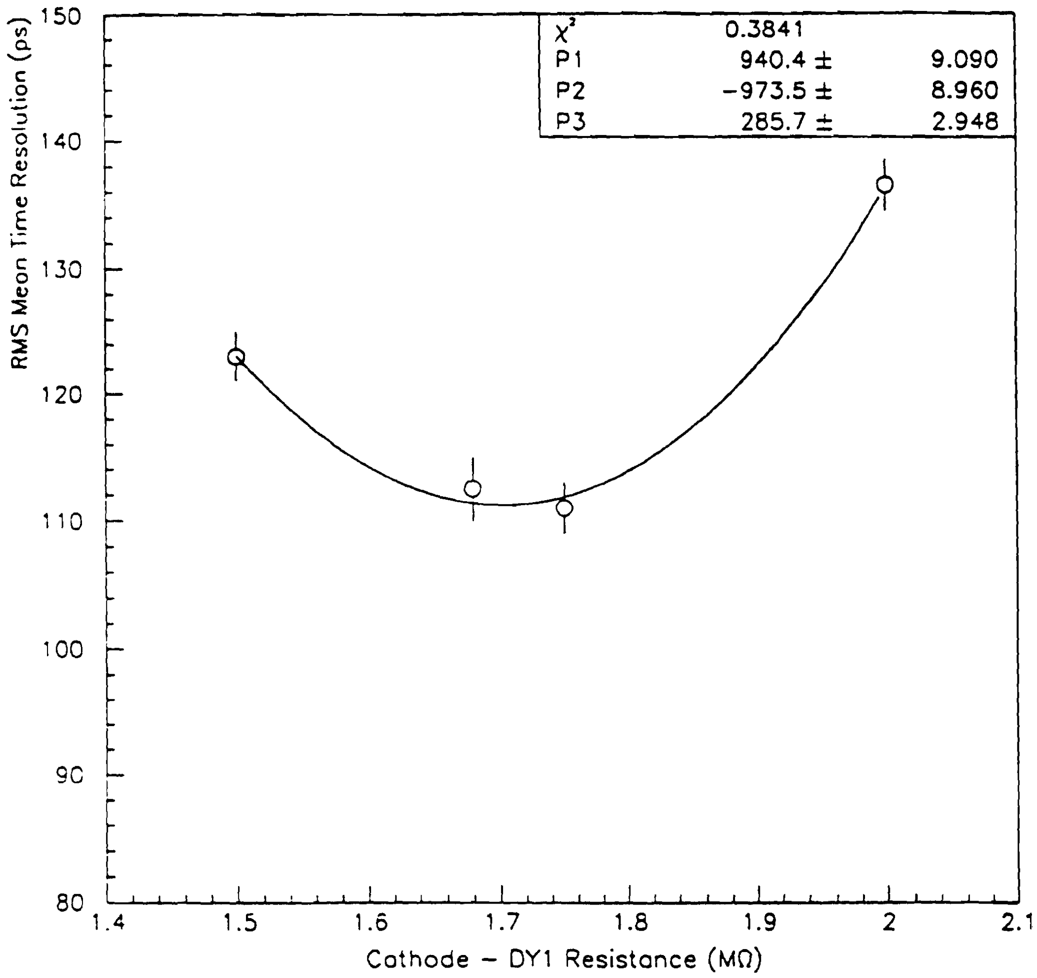

Figure 49: Relative timing characteristics of the Hamamatsu R3478 photomultiplier tube as a function of the photocathode - first dynode resistance (HV = -1400 V, discriminator = -25 mV). For this test, the 5L3-404 scintillator was used with a ^{207}Bi source.

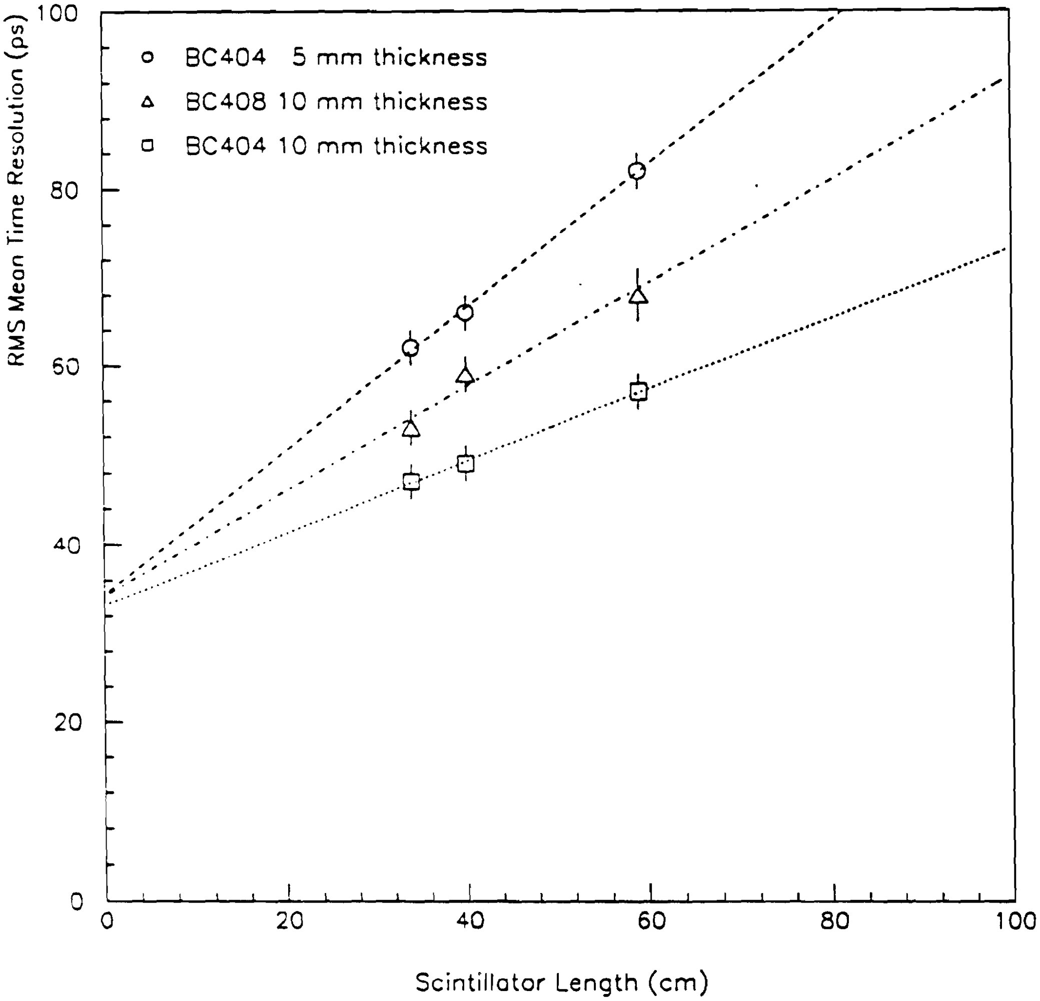

Figure 50: Mean time resolution as a function of length of the test scintillator.

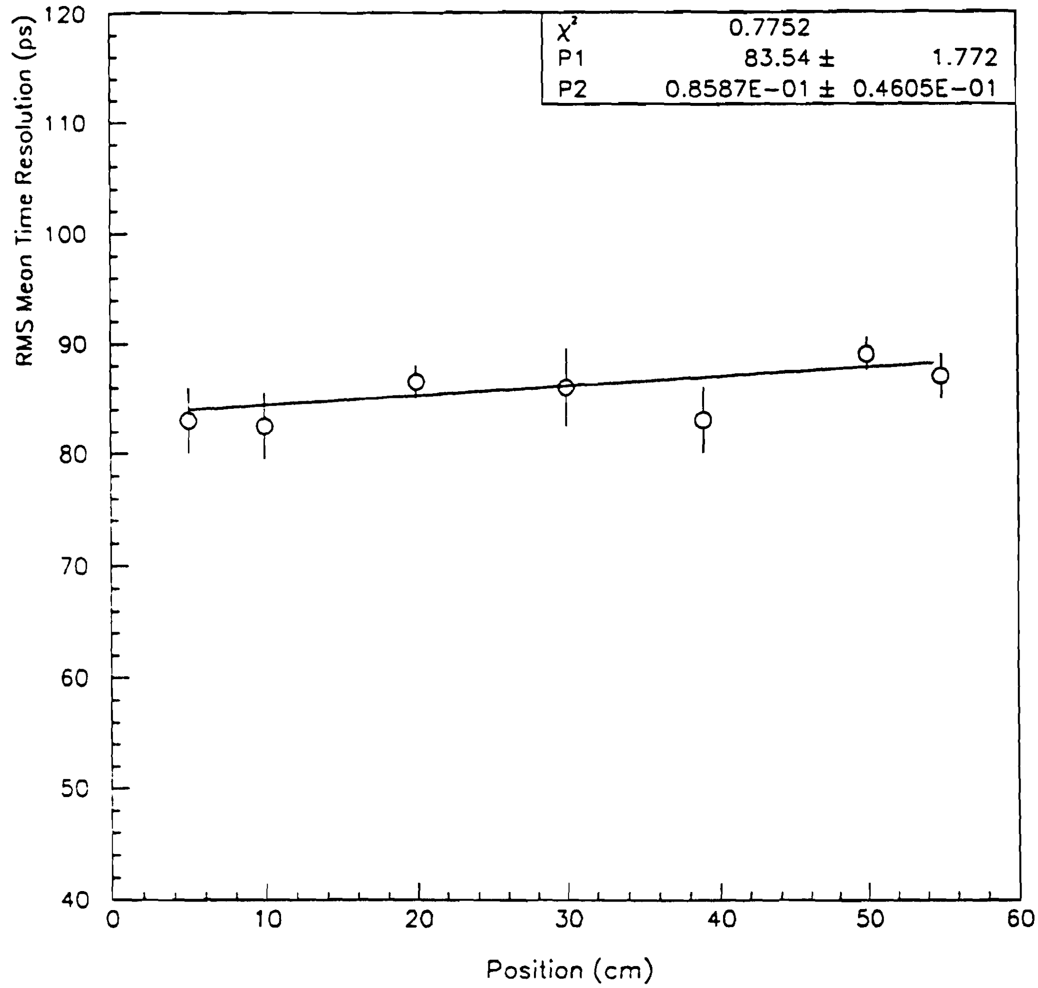

Figure 51: Mean time resolution as a function of trigger counter position along the length of the test scintillator (measured from PMTA). For this test, the 5L3-404 scintillator was used with a cosmic ray source.

hodoscope system.

6.2.3 Future Development and Production Schedule

Our TOF research and development efforts will continue over the next six months, during which time we will focus primarily on the development and testing of an on-line (laser) calibration system and a novel PMT base. The PMT base design envisioned is one similar to that developed for the ZEUS experiment at DESY, which incorporates a compact, remotely adjustable Cockcroft-Walton high voltage supply [64]. We also plan to explore the idea of incorporating part of the read out electronics (e.g. pulse discrimination) in the PMT base itself. This arrangement is expected to improve timing resolution by eliminating pulse dispersion in the cable between the PMT and discriminator. The additional benefits of such a design in a large detector system like E864 are many, including lower mass, fewer cables, easy control, and cost effectiveness.

In addition to the ongoing TOF research and development efforts, we will continue to design the mechanical support structure required for each hodoscope station.

As the TOF hodoscopes are required for all aspects of the E864 physics program, we would like to proceed on a development and construction schedule which will ensure all three stations are completed and installed on the experimental floor by 1993. Our present and future efforts to maintain such a schedule are outlined in Fig. 52. If this scenario is realized, it is anticipated that some use could be made of the 1993 AGS proton and/or Au beam running periods for detector shakedown and/or to pursue some of the lower sensitivity E864 physics objectives. The funding allocation needed for the TOF hodoscope system to progress on such a schedule requires a large fraction of the total budget for this project to be disbursed in FY92, with the remainder in FY93. The budgetary breakdown is provided in the section on staging and funding plans.

6.3 Straw Tube Chambers

6.3.1 Occupancy, Resolution and Efficiency Design Criteria

Three straw tube arrays will be located as shown in Fig. 5. The demands on the granularity of the arrays are mainly driven by the desire to minimize pile-up of multiple interactions during the maximum drift time in the tubes. With a beam rate of 10 MHz and a 10% interaction length target, events giving hits in the spectrometer occur at a rate of 1 MHz. About 10% of these events are central collisions, which

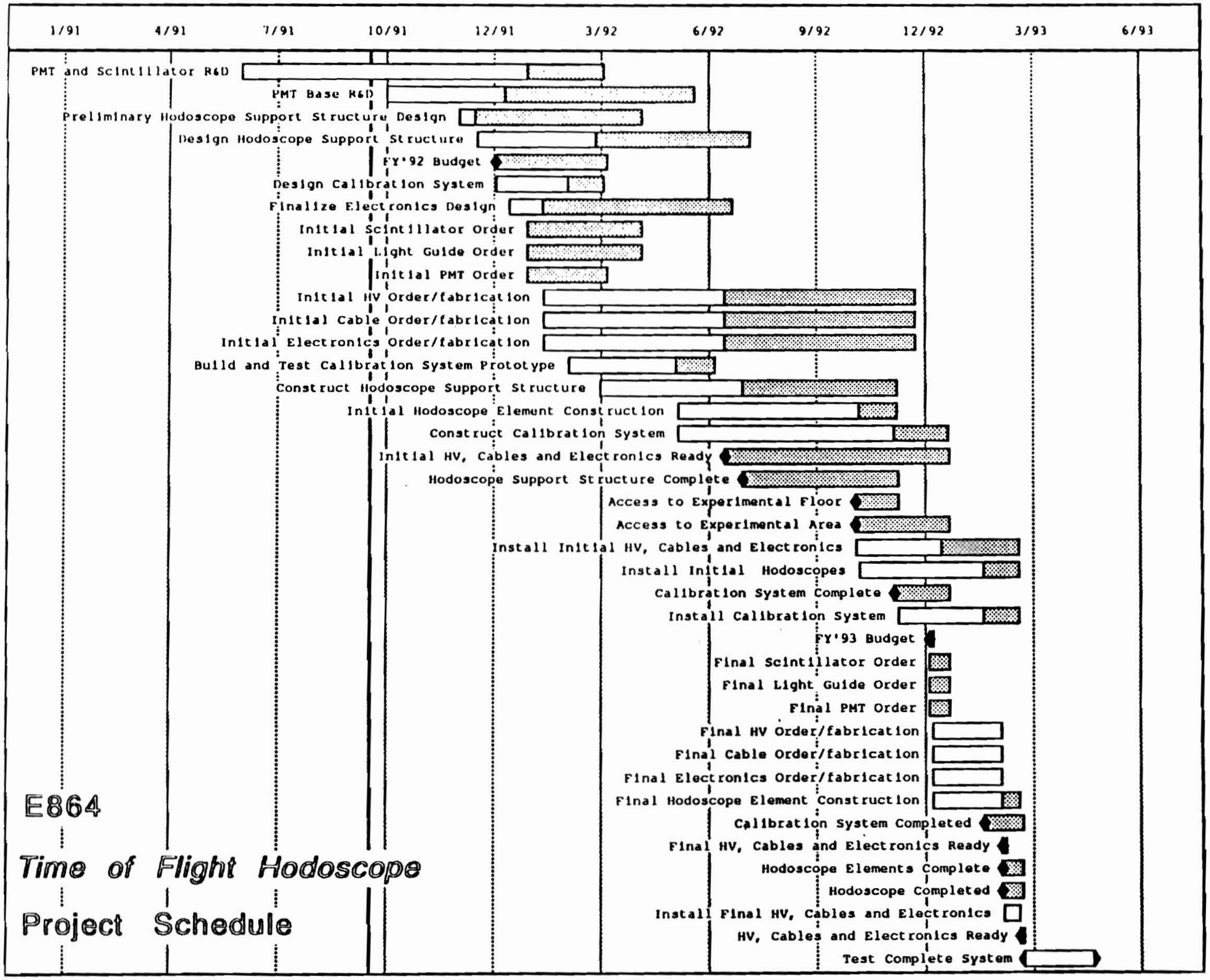

Figure 52: Schedule of present and future efforts in the development and construction of the TOF hodoscope system.

yield the hit multiplicities in Table 27. The occupancies for less central events are similar. The use of conventional argon plus ethane gas mixture results in maximum drift times of 40 nsec in arrays S1 and S2, and 80 nsec in S3, corresponding to pile-up rates of 4% to 8%. We plan to investigate the feasibility of using faster gases, such as CF_4 [65], which could reduce the pileup rates by a factor of two.

Occupancies of a few per cent and acceptable pile-up can be achieved with straw tube dimensions similar to those described in the literature [66, 67, 68, 69].

Each straw tube array is comprised of six layers, as illustrated in Fig. 53, with 2 layers each of x (vertical), u and v (stereo) tubes. The overlapping double layers are needed to cover the dead region at tube boundaries.

To save on electronics costs, the straw tubes in S1 and S2 are read out as yes/no hits. In principle the spatial resolution, both in horizontal and vertical directions, could be improved by measuring drift times. The resulting improvement in momentum resolution is marginal, since Coulomb scattering dominates for most of the rare objects of interest.

Design parameters for S3 are shown in Table 28.

6.3.2 Special Considerations for S1 in Vacuum

For S2 and S3 the frames around the end plugs are in a region shadowed by shielding. This is not the case for the upper end of the straws in array S1. The end plugs in this region need to contain minimal materials. We plan to use diffusion from one end of the S1 tubes, so that the plug on the upper end need provide only gas sealing and wire support. This technique of gas handling has been used successfully [69],

Table 27: Straw Tube Occupancies

Array	Hits	Width	Tube diameter	Hits/tube [a]
1	11.7	128 cm	0.4 cm	0.037
2	19.6	234 cm	0.4 cm	0.034
3	13.3	513 cm	0.8 cm	0.021

---

[a] Hit rate for one central event, including background from shielding leakage.

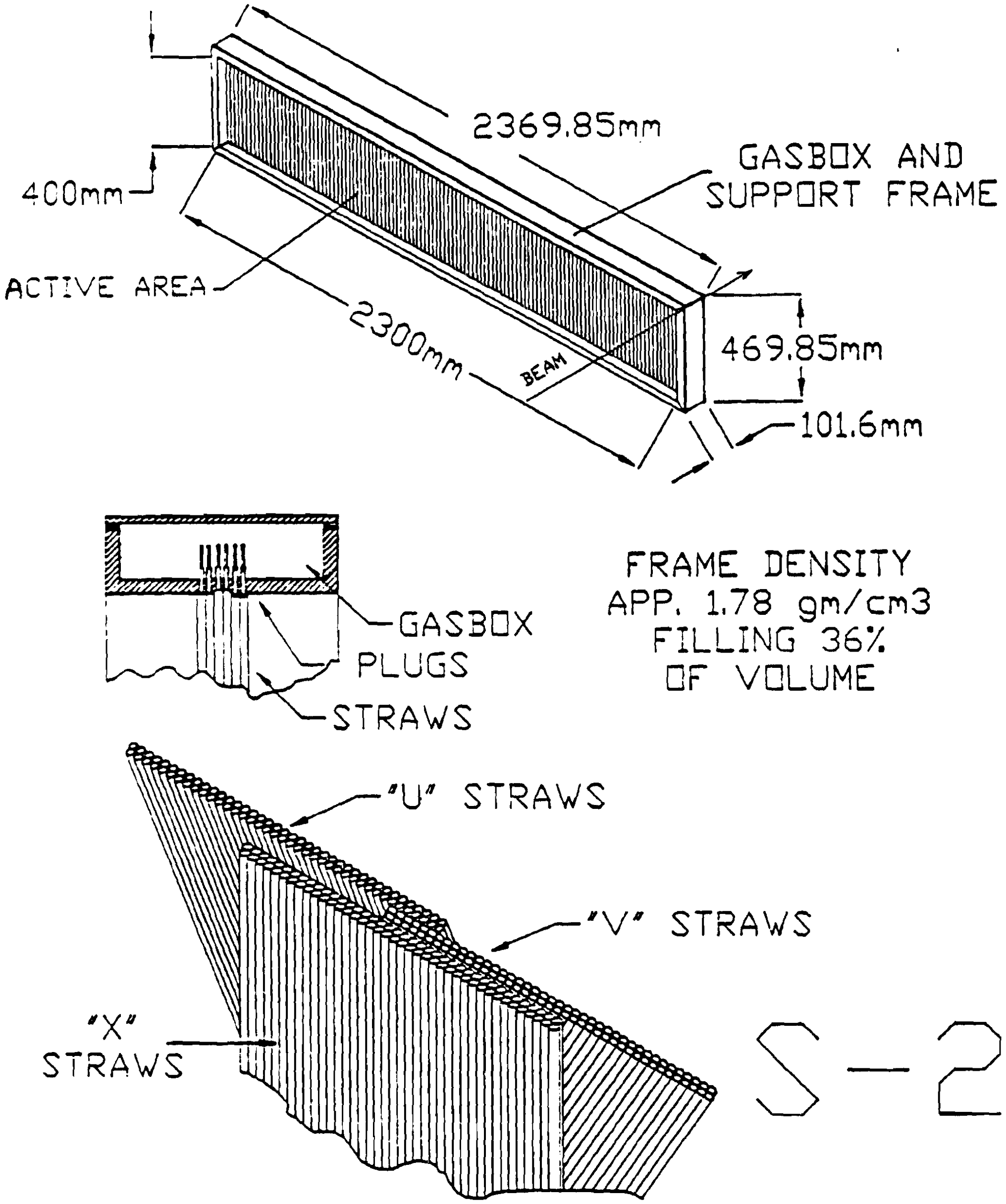

Figure 53: Contents of one straw tube array.

Table 28: Straw Tube design parameters.

Aluminum cathode	0.3 mils
Anode wire	25 micron gold-plated tungsten
Wire tension	70 grams
Gas flow rate	1 fill/6 hours

for straw tubes of similar diameter and length.

According to Ref. [70], straw tubes of similar diameter and wall thickness have been tested with an over-pressure of up to 40 psi. We expect the operation of S1 in vacuum to be a soluble problem, with the straw tube material withstanding the pressure differential in the active region of the array.

Prototype testing is planned to check the long-term mechanical stability of unsupported tubes with a 15 psi pressure differential. As a backup, a minimal frame structure is being considered for the upper end of the S1 straws.

6.3.3 Prototype Testing

Prototype construction and testing is to be initiated in fall 1991. Chambers S2 and S3 are similar to straw tube arrays documented in the literature. The prototype R&D includes testing various options for gas flow, high voltage connections, signal connections, and mechanical integrity. The feasibility of using fast gases (CF_4 mixtures) in E864 will be studied in a test beam, where the tubes must meet the E864 efficiency and stability requirements while minimizing pile-up.

The R&D work is planned so that chambers S2 and S3 will be ready for operation for phase 1 running in 1994. Chamber S1, which has the added complication of operating inside the vacuum enclosure, is planned to be available for phase 2 running.

Specific development tasks include the following:

- Determine how to keep a large number of straws in position to an accuracy of 100 to 200 microns.
- Build several sections of 500 straws with 6 mutually-supporting planes.

- Construct frame/gas structure, and equip a few straws with real plugs and wires to check operation.
- Work out logistics of electronics and connector placement, wire stringing, methods for replacing wires in the field, and support and alignment of planes.
- For S1, develop vacuum components such as seals and feed throughs.
- Investigate minimum tube wall thickness which can be used in S1 and S2 to minimize background from interactions in these chambers.

Prototype evaluation tasks include the following, using both cosmic rays and beam tests:

- Construct planes of 6.4 cm width, to have a reasonable cosmic ray rate, and to have enough samples to assess variations.
- Measure the efficiency of the X,X' combination, to demonstrate a reasonable high voltage plateau.
- Use TDC's to check that the single plane inefficiency is purely geometrical, associated with the straw walls, and evaluate the effect.
- Study the uniformity of the chambers to check for variations caused by sagitta or gas circulation effects (particularly in S1).

The prototypes to be constructed are as follows:

- S1: 16 X straws, 16 X' straws, 4 mm diameter, 22.5 cm length, in vacuum.
- S2: 16 X straws, 16 X' straws, 4 mm diameter, 40. cm length.

The costs for the development and prototypes are listed in Table 29.

6.3.4 Responsibility

The Penn State University group has taken responsibility for constructing the three tracking stations. This group has successfully deployed large MWPC's in E706 [71], as well as precision straw tube drift chambers in E706 [72] and E760, all at Fermilab. The group employs an experienced engineer (J. Passaneau), and has at its disposal laboratory facilities (large assembly hall with winding table, clean room, plastics shop, machine shop, electronics shop, CADCAM, etc.) necessary for the

Table 29: Costs of Development and Prototypes.

Prototype Construction	
64 straws	$ 50
128 end plugs (up-front cost of injection mold)	6000
frame and gas manifold materials, machine shop labor	2000
50 meters 25 micron gold-plated tungsten wire -$ 1/m	50
vacuum chamber design and construction, vacuum pump	2500
gas, gas distribution and monitoring	1500
electronics connectors, ribbon cable	500
anode pins, crimp tools	1000
labor: cutting, gluing, string wires	1000
jigs for gluing, stringing	800
miscellaneous (solder, conducting epoxy, glues)	250
Subtotal:	$ 15,650
Gas, Mechanical and Electrical	
Machine shop time, construction	$ 3000
1000 straws -$ 1/m	1000
structural components, miscellaneous	1000
Subtotal:	$ 5000
Test Setup (Required for PSU and BNL)	
3 Trigger counters	$ 1000
NIM bin + miscellaneous NIM units (inc. chamber HV)	5800
64 amplifiers (e.g., LeCroy 2735 discriminators)	2400
low voltage power (+-5V, Sorensen SRX200-5)	2000
64 channels of input register (LRS 4448)	5000
16 channels of TDC (LRS 2229)	4320
1 Camac crate	3000
Microvax II + Camac interface (PSU)	
Subtotal:	$ 23,520
Total:	$ 44,170

construction of the three stations. Large scale labor requirements are met by hiring undergraduate students who, under appropriate supervision, have been found to be very cost effective.

6.4 Scintillating Fiber Calorimeter

We plan to use a longitudinal fiber calorimeter which consists of scintillating fibers in a lead matrix, oriented so that the fibers are approximately along the beam direction. This design is expected to give improved energy and timing resolution over a plate calorimeter and to allow a virtually seamless tower geometry arrangement.

6.4.1 Calorimeter Requirements

The most stringent requirements on the energy and time-of-flight resolutions are set by the neutral particle search. Monte-Carlo studies have shown that an energy resolution of about $\delta E/E = 0.4/\sqrt{E}$, and a time-of-flight resolution of $\delta t = 0.5$ ns, will provide adequate mass resolution and background rejection for the neutral search.

The occupancy rate of the calorimeter cells is determined by the particle flux, cell size and the density of the detector. A lead-to-scintillator volume ratio of at least 4:1 would restrict the lateral spread of showers to an acceptable level, and a cell cross section of 10 cm by 10 cm would be granular enough to sufficiently separate showers in E864. Of course, the volume ratio is constrained more by the need to achieve compensation, and the 4:1 ratio has been confirmed by the SPACAL collaboration as appropriate to achieve this end.

The depth of the detector must be long enough to contain a large fraction of the shower, while short enough to keep the cost of the detector within reason. Towers of 100 cm (5.3 interaction lengths) should be adequate.

6.4.2 Construction Techniques

Constructing individual calorimeter towers with the dimensions 10 cm by 10 cm by 100 cm would be most convenient. A cross-section of such a tower, assuming 1 mm diameter fibers and the lead-to-scintillator volume ratio of about 4:1, is shown in Fig. 54. Each tower pictured contains 2500 fibers.

We investigated casting each tower, however this method proved to be too difficult. The 1 mm diameter holes, which were cast in the tower with stainless steel rods, inevitably varied from their ideal positions as the rods "clumped" together due to their small diameter, close proximity, and meter-long length. The "clumping" would cause certain regions of the tower to be over-sampled with fiber, with other regions lacking the proper density of scintillator. This nonuniformity would detract from the calorimeter's resolution. Another technique casts scintillating fiber directly in a low melting point eutectic alloy. However, the alloy contains a large percentage of cadmium, which has a large neutron cross section, and is thus not acceptable for hadronic calorimetry.

A more widely-used method is that of constructing plates with half-circular grooves, and then bonding the plates together. Grooves can be extruded, rolled, or machined into the plate. An example of such a plate is shown in Fig. 55. It would be easiest to set the fibers into their grooves, spread a layer of epoxy over the lead and fibers, and then sandwich this with another plate of lead. This method, though simple, is irreversible and can potentially exacerbate the radiation damage in the fibers.

The SPACAL collaboration at CERN is developing an alternative technique where extruded, grooved plates are tinned with a thin layer of solder, and then the plates are stacked and heated until the solder flows. The plates are thus bonded together but the holes remain empty so that fibers can be inserted after the tower is constructed. This has the advantages that the fibers can be removed from the module, and there is an air layer around the fiber which makes the fiber more resilient to radiation damage [73]. Unfortunately, this technique increases the cost of the extruded plates by a factor of five [74].

E864 is also developing a technique to construct towers out of grooved plates. As in the SPACAL method, the goal is to construct a tower which contains empty holes for the fibers, however, the adhesive used in this method is a 3M heat-curing epoxy [75]. This epoxy, which comes dissolved in a solvent, can be painted on material and left to dry to a tack-free surface. After painting a thin layer of epoxy on a plate of lead, grooves would be machined in the lead, thereby removing both the lead and adhesive from the groove. The machined plates would then be stacked and placed in an oven to cure. As in the SPACAL method of bonding, the fibers can be removed from the module, and there is also an air layer around the fiber which helps the fiber resist radiation damage. Applying the heat curing epoxy to the lead plates should only add about 10% to the cost of the plate.

6.4.3 Geant Simulation

We have begun an effort to simulate spaghetti calorimeters using the GEANT detector simulation package. The goal of this effort is to provide guidance in the design of our calorimeter prototype, and ultimately in the calorimeter used in the experiment.

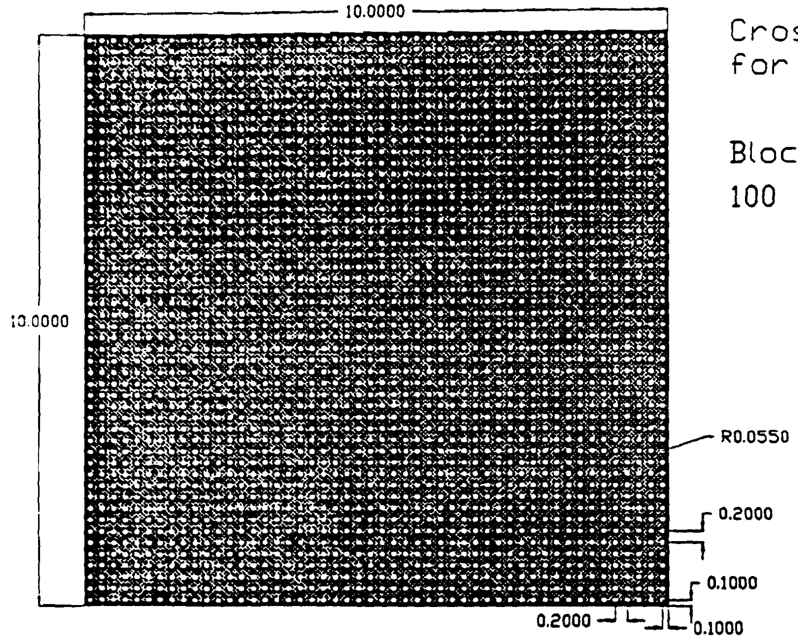

Cross section of block for Yale calorimeter.

Blocks will be approx. 100 cm long

Figure 54: Cross-section of a single calorimeter tower using 1 mm diameter fibers and a lead-to-scintillator volume ratio of about 4:1. (Dimensions are in cm.)

Cross section of lead plate for Yale calorimeter. Plates will be approx. 100cm long

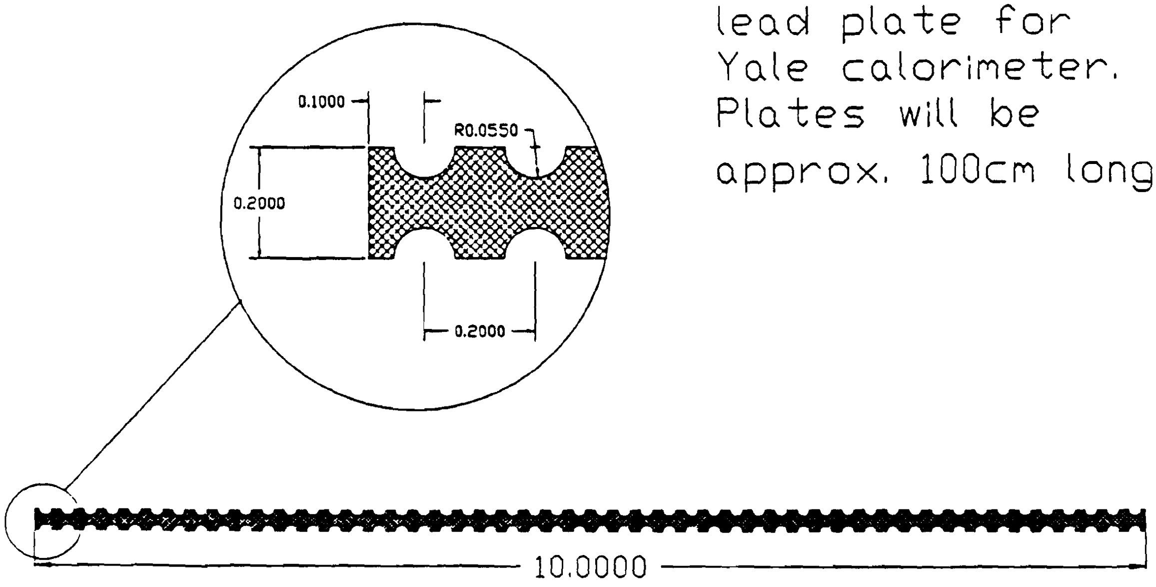

Figure 55: Cross-section of a grooved plate. Fifty stacked plates will make a single tower. (Dimensions are in cm.)

Hadronic Energy Resolution	
SPACAL data	$\sigma/E = (.277 \pm .020)/\sqrt{E} + (.025 \pm .001)$
GEANT simulation	$\sigma/E = (.328 \pm .02)/\sqrt{E} + (.019 \pm .005)$
Electromagnetic Energy Resolution	
SPACAL data	$\sigma/E = (.129 \pm .003)/\sqrt{E} + (.0123 \pm .0005)$
GEANT simulation	$\sigma/E = (.106 \pm .019)/\sqrt{E} + (.038 \pm .006)$

Table 30: Comparison of fiber calorimeter energy resolutions: Monte-Carlo vs. data.

The complex physical processes at the heart of calorimetry, combined with the fine-grained geometry inherent in fiber calorimetry, make this simulation a formidable task. We thus began by determining whether GEANT could reproduce results from actual spaghetti calorimeter tests performed by the SPACAL collaboration at CERN. So far these results are very encouraging.

We used GEANT to simulate a fiber calorimeter consisting of 1 mm diameter scintillating fibers embedded in lead such that the lead-to-scintillator volume ratio is 4:1. We chose the fiber materials (both scintillator and cladding type), the lead alloy (96% lead, 4% antimony), and other properties of the detector (effective attenuation length of the scintillator, length of the modules, etc.), to match the specifications of the SPACAL prototype detector [12, 76].

The hadronic and electromagnetic energy resolutions estimated by the GEANT simulation compared favorably to experimental results obtained by the SPACAL collaboration. Figure 56 shows both the Monte-Carlo and the experimental resolutions. Table 30 compares the fit of the simulation's resolution curve to the experiment's, assuming the functional form

$$\frac{\sigma(E)}{E} = \frac{a}{\sqrt{E}} + b,$$

where a and b are constants. Our simulation of electromagnetic showers shows slightly more energy deposited in the fibers than the SPACAL results. We are investigating this difference, which we believe is due to differences for incident particles which start to shower in the fiber. Since our requirements are only for hadronic showers, this small effect for electromagnetic showers has negligible influence on results of interest to E864.

The ratio of the electromagnetic and hadronic responses of the detector, e/π, can also be used as a measure of the simulation's accuracy. We will make this comparison upon completion of GEANT runs which are currently under way. Further tests of the spatial distributions and temporal development of showers will also be performed.

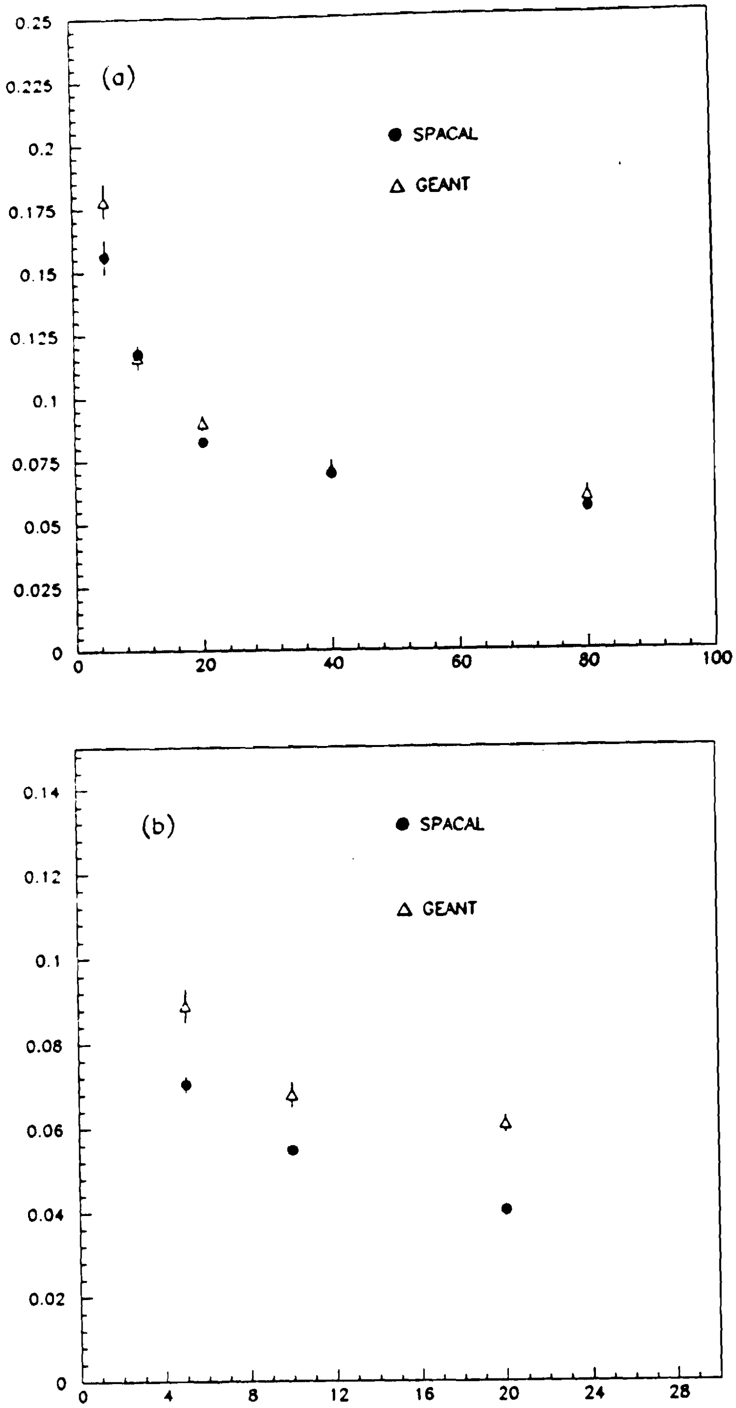

Figure 56: (a)Hadronic and (b) electromagnetic energy resolutions obtained by the SPACAL collaboration and E864's GEANT simulation. Vertical axis is $\delta E/E$ (best fit Gaussian), horizontal axis is kinetic energy in GeV.

The fiber diameter, tower length, volume ratio, and gate length are some of the design parameters to be determined before a prototype is constructed and tested. The GEANT simulation will, given continued success, help ascertain some or all of these parameters.

6.4.4 Scintillating Fiber Tester

A scintillating fiber tester is currently under construction. The schematic of this device is shown in Fig. 57. A quartz fiber carries modulated light from a UV lamp to the fiber to be tested. The UV lamp has its peak output at 365nm which is close to the peak of the primary scintillation in the fiber (≈350nm). The UV excites the fluors in the plastic scintillating fiber which give off visible light. A photomultiplier tube at the end of the plastic fiber views the light output. The signal from the photomultiplier and a reference signal from the chopper go to a lock-in amplifier. The output of the lock-in is then proportional to the light output from the scintillating fiber. Another photodetector not shown views the UV lamp directly to provide the normalization. The quartz fiber may be positioned anywhere along the scintillating fiber under computer control and also (not shown in the figure) stepped from one fiber to another across a tray holding up to 50 fibers. The output of the lock-in amplifier is also read into the computer. This allows us to measure attenuation lengths and relative light yields of various fibers. A small prototype of the fiber tester has been built and successfully used to test this technique.

The first role for this set-up will be to evaluate different brands of fiber for light output, attenuation length, and uniformity. After a brand of fiber is chosen for the prototype and the experiment, the tester will be used to characterize each batch of fiber according to attenuation length, so that similar fibers can be used in a given tower and tower-to-tower variations of fiber could be noted for use in calibrations.

6.4.5 R&D and Construction Schedule

The fiber calorimeter project is divided into three stages: design, prototype testing, and final construction.

The design effort will determine the physical characteristics of the prototype detector such as fiber type, lead-to-scintillator volume ratio, and construction methods. These decisions will then be evaluated by placing the ~10-tower prototype in a beam and measuring its characteristics. The prototype will also be used to evaluate calibration and monitoring schemes using radioactive sources and light pulsers. After final specifications are determined, construction of the 936-tower final detector

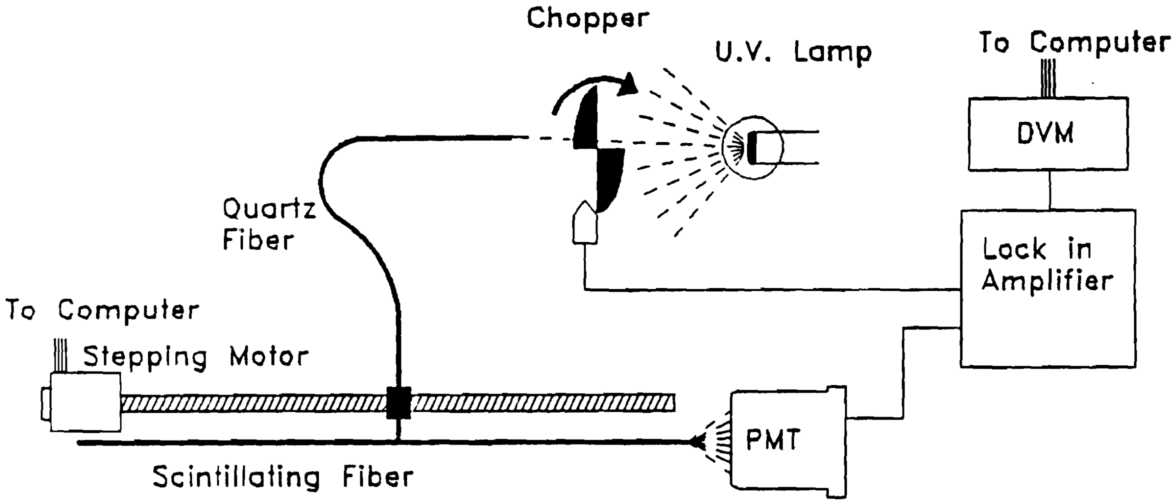

Figure 57: Schematic diagram of the scintillating fiber tester.

Materials Cost for One Module		
Fibers ($.33/meter x 3175meters	$1050	
Lead 200.18lb @$3/lb	$600.54	
Shipping of lead and modules	$40.00	
Epoxy for lamination	$40.00	
Light pipe and clamp	$60.00	
Photomultiplier	$700	
Base	$50	
Total	$2540.54	
Cost for 12 modules		$30,486
Cost for Tooling		
Parts and labor for fiber testing	$1000	
Part and labor for module assembly line	$10,000	
Jigs for lamination	$2000	
Jigs for termination and light pipe preparation	$2000	
Total tooling cost		$15000
Sources and fixtures for module calibration		$20,000
Electronics for testing		$5000
Total costs for R&D and Tooling		$70,486

Table 31: R&D and Tooling Costs for the Calorimeter

will proceed.

We hope to conclude the design phase by January 1992, at which time prototype materials can be ordered. The prototype items and costs are given in Table 31. The testing of the prototype, though dependent on an available test beam, should be completed by summer 1992. By that time materials can be ordered for the actual calorimeter.

As outlined in the staging plan given in the final chapter, 1/4 of the fiber calorimeter should be ready for a run in early 1994. Thus only 1/4 of the detector's materials will be ordered initially, and the remainder will be delayed.

6.5 Multiplicity Trigger

6.5.1 Introduction

The multiplicity trigger is designed to select central events. This is possible because of the direct correlation between particle multiplicity and centrality in heavy ion collisions. HIJET/GEANT monte carlo simulations have been used to help design this trigger.

For the monte carlo studies a 1 mm thick radially segmented scintillation counter was placed 10 cm from the gold target. The scintillation counter is a disk which covers the angular range from 10° to 45° (η = pseudorapidity = 0.88 - 2.44). The region between the target and scintillator is vacuum, and lead or a magnetic field can be used to eliminate the cloud of delta rays produced by the gold ion traversing the gold target. (Note that the lead in the study presented below is cylindrical with the same inner and outer radius as the scintillation counter. Future designs will include lead that is tapered so that the particles which hit the scintillator will traverse equal amounts of lead.) The energy deposited in each segment of the scintillator is then recorded and analysed.

An event is simulated with GEANT by sending a 11.71 GeV/nucleon gold ion through a 10% gold target. This ion produces delta rays until it interacts at a random depth in the gold target. This collision is simulated by the HIJET event generator. The interaction products and delta rays proceed through the target and in the lead, magnetic field, or vacuum region. Finally, particles deposit energy in the scintillator. All of GEANT's physics processes were turned on for the simulation so that all decays and secondary interactions in the target, lead and scintillator are included.

6.5.2 Monte Carlo Simulations

First, the discrimination between central and peripheral events was studied with vacuum between the target and scintillator. This study indicated that even a single counter trigger would give good central/peripheral discrimination. Under experimental conditions this would probably mean that a four counter system would be adequate. The segmentation would be useful for rejecting fake triggers due to upstream interactions, etc. Studies with more counters were carried out, however no simple trigger algorithm gave better discrimination for events coming from the target than the one counter system.

A gold ion which passes entirely through the target without interacting produces a cloud of delta rays. These events were simulated with GEANT to determine the counting rate at the scintillator. The computer simulation showed that ≈ 200 delta rays per traversal enter the scintillation counter. For the counter to work well it is desirable that the rate of delta rays from beam ions should be less than the rate of particles from from central and peripheral events. The delta rays are of relatively low energy. For example, if we eliminate those delta rays with kinetic energy less than 40 MeV, then the rate at the scintillator would be 4×10^7, which is comparable to the rate from peripheral and central events. Delta rays can be attenuated with a high-Z material. For the monte carlo simulation we used 9.6 cm of lead, which easily eliminates enough delta rays. Typically, depending on the details of edge scattering, the average number of delta rays going through the counter per beam gold ion is 0.05 — 0.1.

We next studied how the addition of lead affects the discrimination between central and peripheral events. Figure 58 is a scatter plot of integrated dE/dx in the scintillator per event versus impact parameter for 1000 Au-Au collisions. The integrated dE/dx per event will be referred to as simply dE/dx for the remainder of this section. We wish to make the dE/dx cut so that we accept approximately 10% of the events. Because of the correlation between dE/dx and impact parameter, these events will be quite central. Figure 59(a) is a plot of the distribution of impact parameters that pass the .16 dE/dx cut. This demonstrates that approximately 10% of the events are selected, and those events which are selected are the most central. Figure 59(b) is a plot of the fraction of events passing the .16 dE/dx cut as a function of impact parameter.

6.5.3 R&D and Prototype Program

The Monte Carlo studies indicate that a scintillation counter based trigger system is adequate to discriminate between central and peripheral events. We plan to prototype such a scintillator based system upon completion of the Monte Carlo design studies. In addition, the prototype program will include a timing system of two counters which will trigger on either the delta rays or reaction products produced by the incident beam particles as they pass through the target. This technique should be reliable for detecting incident beam particles with charge greater than 12.

We are requesting $21,500 for this R&D program. Note that part of these funds will be directly applicable to the final trigger system. The budget breakdown for these requested funds are presented in Table 32. We request that these funds become available in time to build and test the prototype in a BNL beam by the summer or fall of 1992. We plan to test our trigger system in the early stages of the installation of the experiment.

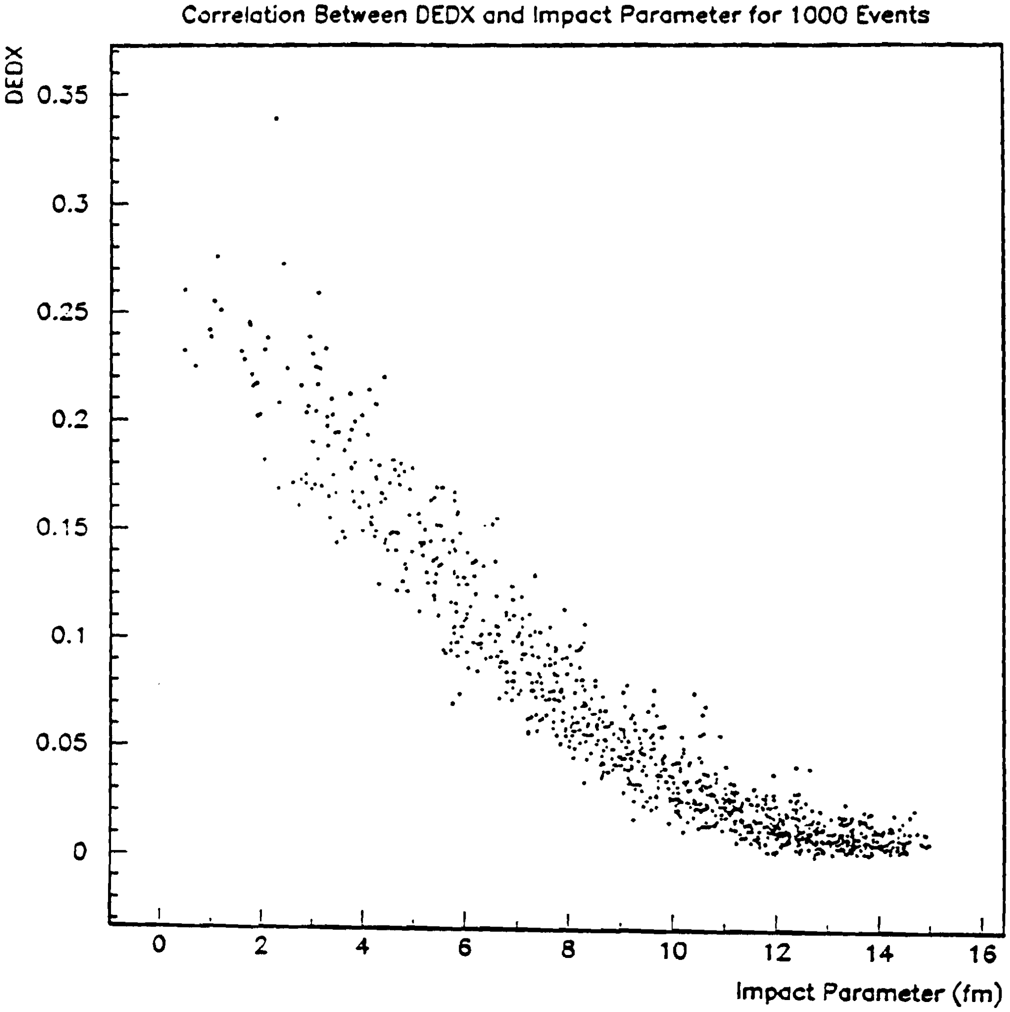

Figure 58: Correlation between integrated dE/dx and impact parameter for 1000 events.

Impact Parameter Distribution for Events with DEDX > .16

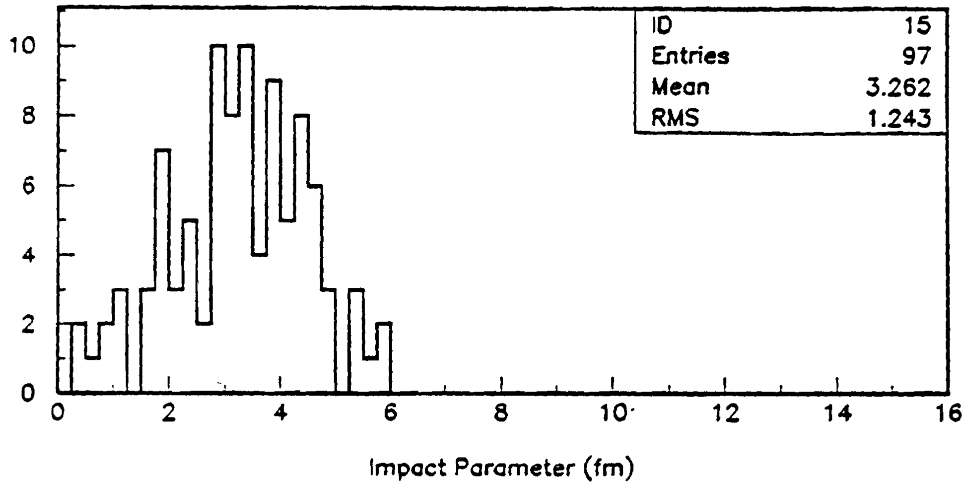

Trigger Probability for Different Impact Parameters with DEDX > .16 Cut

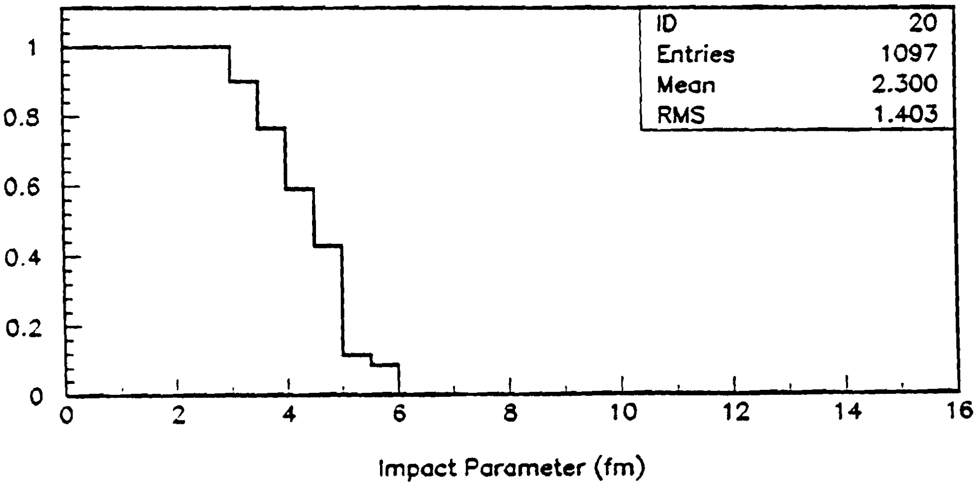

Figure 59: (a) Distribution of impact parameters which pass a dE/dx > .16 cut. (b) Trigger probability for a particular impact parameter event to pass the dE/dx > .16 cut.

Item	Cost ($)
Phototubes, Bases, and Scint.	5,400
Electronics	6,400
Data Acquisition	7,200
Machine aluminum plate and mounting brackets	1,000
Total	20,000

Table 32: R&D Requested Budget for the Multiplicity Trigger.

6.5.4 Conclusions

The Monte Carlo simulations demonstrate that a relatively simple multiplicity trigger gives excellent central/peripheral discrimination. Further refinements of the design, such as the exact amount of lead and its exact shape, remain to be done. In addition, a highly segmented scintillator system may be desirable. The segmentation is useful for event characterization, and may help the efficiency of this array for detecting a second interaction within our time window. Studies determining how highly segmented the scintillator should be as well as the timing resolution of this or another counter array are in progress.

7 Detector Costs

A detailed discussion of the E864 detectors and their performance requirements was given in the experimental method section above. A review of the basic systems and the number of channels in each detector is given here for clarity.

Each of the three hodoscope planes consists of 256 counters, with each counter viewed by two phototubes. The Pb/fiber calorimeter is made of 936 towers, also viewed by phototubes. Each of the three straw tube tracking stations will cover (x,y,u) coordinates, with two planes of straws for each coordinate to ensure full efficiency. There will be a total of 5430 4 mm diameter tubes, and 3858 8 mm diameter tubes. There will also be a multiplicity counter used in the pretrigger, electronics for a higher-level trigger, and a data aquisition system to record the experiment's data.

The detector cost estimate for these systems comes to a total of $ 5,847,000, plus $ 41,000 of the R&D request which provides some equipment used to fabricate the E864 detectors. The reasoning used to get this number is outlined in Tables 33–36. This estimate accounts for the materials and labor needed to build the systems listed above. It is based on discussions with vendors and includes quantity discounts wherever applicable.

This estimate is meant to be representative of detectors which can be built using already-existing methods, or systems purchased as new equipment. We therefore feel that this estimate is an upper limit of the cost of the experiment. For example, actual quantity discounts cannot be realized without initiating a formal bidding process between vendors. Finally, additional savings from obtaining used materials or systems were not included.

MATERIALS	Unit	Cost/unit	# Units	Total (k$)
Lead sheets (0.083 x 24 x 40 in)	sheet	$31.04	8075	250.65
Scintillating fibres (1 mm dia.)	meter	$0.33	3087500	1018.875
Lucite terminator ("donut")	foot	$40.00	238	9.52
Lucite lightpipe	foot	$15.00	475	7.125
Epoxy cement (eg. BC-500)	gallon	$400.00	100	40
Calibration system	channel	$30.00	950	28.5
Support structure for calorimeter	item	$20,000.00	1	20
SUBTOTAL:				**1374.668**
TOOLING (R&D budget)				
Parts and labor: fiber tester	item	$1,000.00	1	(1)
Parts and labor: assembly machine	item	$10,000.00	1	(10)
Jigs for terminator and l.p. prep.	item	$2,000.00	1	(2)
Gluing jigs (lamination)	item	$2,000.00	1	(2)
Cobalt-60 module testing system	item	$20,000.00	1	(20)
R&D SUBTOTAL:				**(35)**
LABOR				
Cut lead into 10 cm strips	hour	$38.00	500	19
Groove lead strips	hour	$19.20	400	7.68
QC 2% of fibers	hour	$19.20	325	6.24
Wash lead strips	hour	$19.20	160	3.072
Lay in fibres and epoxy	hour	$19.20	133	2.5536
Laminate layers	hour	$19.20	133	2.5536
Machine module sides for stacking	hour	$38.00	475	18.05
Machine beam end of module	hour	$38.00	475	18.05
Mach. Lucite "donuts" and lt. pipe	hour	$38.00	475	18.05
Trim fibre bundles & att. "donuts"	hour	$19.20	238	4.5696
Test completed module (cobalt-60)	hour	$19.20	475	9.12
Transport to BNL (service)	item	$20,000.00	1	20
SUBTOTAL:				**128.9388**
DETECTOR TOTAL:				**1504**
R&D TOTAL:				**(35)**

Table 33: Cost estimate of E864 Pb/fiber calorimeter. The tooling costs in parentheses are contained in the R&D budget.

Item	Description	Cost
	HODOSCOPES ($ 259k):	
counters	quotes from Bicron sales rep.:	
	* materials (BC-420) for all 3 planes	$ 95k
	* diamond tool finishing (equivalent to polishing)	$ 25k
light pipes	from experience in FNAL E760, $ 25/pipe	$ 38k
labor	glue, wrap, test counters, 1hr./counter at $ 20/hr.	$ 31k
misc.	* calibration equipment	$ 50k
	* mounting/mechanical supports	$ 20k
	STRAW CHAMBERS ($ 243k):	
tube materials	est. by R. Lewis and J. Passaneau (Penn State) from experience on FNAL E760: includes tube cost from Euclid Spiral Tubes (Apple Creek, OH), end plugs, feedthroughs for gas and wire	$ 61k
labor	$ 12/tube to cut, glue, wire	$ 120k
misc.	* frames (also act as gas feed for tubes)	$ 38k
	* wire - 1 mil Au-plated tungsten	$ 2k
	* epoxy	$ 8k
	* jigs, etc.	$ 4k
	* engineering time (J.Passaneau)	$ 10k
	PHOTOMULTIPLIERS ($ 988k):	
hodoscope tubes	Hamamatsu R2076 (or equivalent): 8 stage, 3/4" diam., risetime = 1.3 ns, transit jitter = 0.36 ns. Cost for tube, base, μ-metal shield is $ 400 in E814 and E802 experience.	$ 614k
calorimeter tubes	Hamamatsu R1828-01 (or equivalent): 12 stage, 2" diam., risetime = 1.3 ns, transit jitter = 0.55 ns., also assume $ 400 for tube, base, and μ-metal shield.	$ 374k

Table 34: Cost estimate of E864 hodoscopes, tracking chambers, and PMT's.

Item	Description	Cost
ELECTRONICS - PMTs ($1,058k):		
ADCs	Phillips 10C2 32 chan. (FASTBUS), 10 bit, full scale=256 pC, 7.5 μsec conversion, $4512.50/card including quantity discount (estimate by sales rep.)	$ 352k
TDCs	Phillips 10C6 32 chan. (FASTBUS), 10 bit, least count=25-800 ps, 7.5 μsec conversion, $4227.50/card including quantity discount (est. by sales rep.)	$ 330k
Discriminators	LeCroy 4413 16 chan, CAMAC card, $1300	$ 202k
FASTBUS crates for ADCs, TDCs	Kinetic Systems F050-A11 crate ($2370), K.S. F050-A01 power supply ($7550), K.S. F053 fan ($800), controller ($3000 from experience in FNAL E791), total cost: $13,720	$ 110k
CAMAC crates (discriminators)	K.S. 1525 high power crate (100A on ±6 V) plus K.S. 3900 controller	$ 64k
ELECTRONICS - STRAWS ($ 724k):		
pre-amps/ discriminators	* pre-amp and discrim., $20/chan. in E814 * power supply for pre-amps	$ 186k $ 10k
PCOS system	LeCroy 2731A latch/delay. 32 chan./card, $1381.60/card (use only on S1 and S2)	$ 235k
TDC system	LeCroy 4290 series drift chamber system, 32 chan./card at $1381.60/card	$ 167k
CAMAC crates	* K.S. 1500 series at $3000 ea with PCOS controller at $4460 ea * K.S. 1500 series ($3000 ea) with controller for dedicated TDC system ($6420 ea) * LeCroy 4299 readout for PCOS and TDCs	$ 60k $ 57k $ 9k

Table 35: Cost estimate of E864 electronics.

Item	Description	Cost
TRIGGER ($ 300k):		
	multiplicity counter	$ 20k
	centrality trigger	$ 180k
	late energy trigger	$ 100k
DATA ACQUISITION ($ 76k):		
	see Table 8 for breakdown	
	event builders and buffers	$ 34k
	tape drives and spares	$ 42k
HIGH VOLTAGE ($ 381k):		
for PMTs	LeCroy 1440 system: $150/chan. in our quantity (quote from company)	$ 371k
for straws	from BNL E814 experience	$ 10k
CABLES ($ 314k):		
PMT signals	each PMT channel has: 300' for ADCs and 100' for TDCs (at $.108/ft), $10 for connectors (FNAL prices),$5 for labor.	$ 144k
PMT HV	100ft. at $.135/ft., $15 for connectors and $5 labor	$ 83k
straw signals	50ft. of 16 channel flat cable, $3/ft.	$ 87k

Table 36: Cost estimate of other E864 systems.

8 Staging and Funding Plan

8.1 E-864 Funding Proposal

We present our proposal for the funding plan for the detector and R&D costs for E-864 in Table 37. In preparing this plan we have assumed that the experiment will be staged as discussed in the overview section. Thus, the plan provides for H1, H2, H3, S2, S3, and 1/4 of the calorimeter, in time for the heavy ion run in FY 94. It also provides for the centrality trigger and enough of the late energy trigger to operate with the 1/4 of the calorimeter that will be available for the FY 94 run. As noted below, we propose to construct 1/3 of the towers by FY 94 (rather than 1/4) in order to lessen the burden of completion in time for the FY 95 heavy ion run. However, only 1/4 will be instrumented for the FY 94 run.

The details of the cost estimates are presented in the section on detector costs, and the details of the R&D costs are presented in the sections on progress of the detector subsystems. In the discussion given below, following the table, we simply indicate how the funds would have to be allocated by fiscal year in order to stage the experiment.

It is perhaps worth repeating that the cost estimate we are using includes the full "value" of all the equipment, assuming that all items which can be obtained commercially are indeed purchased. We believe that there may be some economies possible in the use of existing equipment, and in "in house" construction of some items that are commercially available. However, we have not carried out a reliable analysis of such economies at this time, and prefer to present a cost estimate which can be clearly explained even though it may represent the "list" price of the experiment.

Of course, our suggestions as to the details of the split between the DOE high energy and nuclear physics divisions are open to negotiation. However, the approximate balance of support represents the true joint nature of the experiment, which addresses key questions in both disciplines.

8.2 Explanatory Comments on Funding Proposal

8.2.1 Hodoscope System

In FY 92, we must carry out the R&D on the hodoscope system (at a cost of 20 k\$) and prepare $\approx 2/3$ of the scintillators and photomultiplier tubes. We also plan to construct 1/3 of the high voltage system and prepare 1/3 of the cables. A calibration system as well as mounting and support hardware will also be constructed.

System (Responsible Collaborator)	FY 92 (k$)			FY 93 (k$)			FY 94 (k$)			Total (k$)
	DOE (HEP)	DOE (NP)	NSF	DOE (HEP)	DOE (NP)	NSF	DOE (HEP)	DOE (NP)	NSF	
Hodoscope (Yale, WNSL)		748 (20)			515					1,263 (20)
Calorimeter (Yale, HEP)	(70.5)			651			1,453			2,104 (70.5)
Straw Tubes (Penn State)			192 (44)			106			42	340 (44)
Centrality trig. syst. (MIT/UMASS/UNM/UNM)	20 (20)									20 (20)
Central Trig. and gate elect. (BNL)		100			80					180
Late E trig. electronics (BNL)					40		60			100
PMT Electronics (BNL, HEEP)		200			538			301		1,039
Straw Tube Read out (BNL,HEEP)					574			150		724
D/A system (BNL)		38			38					76
Total Detector Costs	20 (90.5)	1,068 (20)	167 (44)	651	1785	84	1,513	451	31	5,846 (154.5)
Beam Line, etc. (BNL,AGS)	500	137		1,393				500		2,530

Table 37: Breakdown of E-864 equipment costs and R&D costs (in parentheses).

Table 38: Hodoscope system FY 92 cost breakdown

Item	FY 92 Cost (k$)
2/3 of Scintillators for H1,H2,H3	126
2/3 of Photomultipliers for H1,H2,H3	409
1/3 of High Voltage System	77
Electronics	19
Calibration System	50
Mountings	20
1/3 of Cables	47
Total	748

Table 39: Hodoscope system FY 93 cost breakdown

Item	FY 93 Cost (k$)
1/3 of Scintillators for H1,H2,H3	63
1/3 of Photomultipliers	205
2/3 of High Voltage System	153
2/3 of Cables	94
Total	515

Some electronics will also need to be purchased to carry out tests of the system components. These could, perhaps be obtained from BNL HEEP but are listed here as part of the WNSL group budget. These electronics will be brought to BNL and used in the experiment. A summary is given in Table 38.

In FY 93, the remaining 1/3 of the scintillators and 2/3 of the high voltage system will be built. The balance (2/3) of the cables will be obtained. A breakdown is given in Table 39.

8.2.2 Calorimeter

We plan to devote FY 92 to the R&D phase and to build and test a prototype. The jigs and tooling for constructing the calorimeter will be developed and completed as part of the R&D effort (they will be used in constructing the prototype). This effort is to be supported by the 70.5 k$ of R&D funds requested for FY 92.

In FY 93 we propose to construct 1/3 of the calorimeter towers and to instrument 1/4 of the towers for the FY 94 heavy ion run. The cost for the electronics is contained

Table 40: Calorimeter FY 93 cost breakdown

Item	FY 93 Cost (k$)
1/3 of Calorimeter Materials	458
Labor (for 1/3 of towers)	43
1/4 of Photomultipliers	94
1/4 of High Voltage System	35
1/4 of Cables	21
Total	651

Table 41: Calorimeter FY 94 cost breakdown

Item	FY 94 Cost (k$)
2/3 of Calorimeter Materials	917
Labor (for 2/3 of towers)	86
3/4 of Photomultipliers	281
3/4 of High Voltage System	105
3/4 of Cables	64
Total	1,453

in the BNL HEEP budget but the photomultipliers, their high voltage and cables are listed here as part of the Yale HEP group budget. Table 40 summarizes the FY 93 costs.

In FY 94 we plan to complete the calorimeter. The breakdown is given in Table 41.

8.2.3 Straw Tube System

The straw tube R&D will be carried out in FY 92 (at a cost of 44.2 k$) and construction of S2 and S3 initiated. The breakdown for FY 92 is given in Table 42.

In FY 93, S2 and S3 will be completed and the material for S1 will be acquired. Table 43 gives the breakdown.

In FY 94, S1 will be completed in time to be used in the run in FY 95. The breakdown is given in Table 44.

Table 42: Straw Tube FY 92 cost breakdown

Item	FY 92 (k$)
Straw Tube Materials	98
Labor	52
Cables	32
High Voltage	10
Total	192

Table 43: Straw Tube FY 93 cost breakdown

Item	FY 93 (k$)
Straw Tube Materials	25
Straw Tube Labor	45
Cables	36
Total	106

Table 44: Straw Tube FY 94 cost breakdown

Item	FY 94 (k$)
Straw Tube Labor	23
Cables	19
Total	42

8.2.4 Central Trigger Counter System

The research and development will be carried out in FY 91 and FY 92 at a cost of 20 k$. The counter system itself will also be constructed in FY 92 at a cost of 20 k$. However, the electronics and fast electronics for the trigger counters will be built partly in FY 92 and FY 93. The costs for these will be listed in the next section.

Although we expect to obtain the electronic modules from BNL (HEEP), the responsibility for the major task of designing and commissioning the centrality trigger counter will be borne by the MIT/UMASS groups.

8.2.5 Electronics for Central Trigger and Experiment Control

The electronics needed to implement the centrality trigger and to provide the various control and gating signals for the detectors will be obtained through BNL (HEEP). As noted previously, the responsibility for commissioning the centrality trigger rests with the MIT/UMASS groups. All of the other detector groups (and the D/A group) will , of course, be involved in the overall experiment control and gating system.

We estimate that 100 k$ will be needed in FY 92 and 80 k$ in FY 93 for BNL (HEEP) to build the centrality trigger and equipment control and gating system.

8.2.6 Late Energy Trigger Electronics

The late energy trigger is derived from the calorimeter signals. The design and commissioning of the late energy trigger is a responsibility of the BNL collaborators.

The design of the trigger will be carried out in FY 92 and the construction of approximately 1/3 of it (at a cost of 40 k$) carried out in FY 93, to be ready for use in the FY 94 run.

The remainder, at a cost of 60 k$, will be built in FY 94 for use in the FY 95 run.

8.2.7 Electronics for Photomultiplier Tubes

The electronics will be drawn from BNL (HEEP) as listed in Table 45.

8.2.8 Electronics for Straw Tube Readout

Electronics for S1 and S3 must be acquired in FY 93 for the FY 94 run at a cost of 617 k$. The electronics for S1 must be acquired in FY 94 to be ready for the FY

Table 45: Electronics for Photomultiplier Tubes

Item	FY 92 (k$)	FY 93 (k$)	FY 94 (k$)
ADC's and TDC's for hodoscope	200	438	
ADC's and TDC's for calorimeter		100	301
Total	200	538	301

95 run, at a cost of 150 k$.

8.2.9 D/A System

It is important to put the D/A system together as early as possible. As noted, we plan to do some running during the FY 93 proton run. We estimate expenditures of 38 k$ in each of FY 92 and FY 93 to complete the D/A system.

References

[1] R.L. Jaffe, Phys. Rev. Lett. **38**, 195, 617E (1977).

[2] S.A. Chin and A.K. Kerman, Phys. Rev. Lett. **43**, 1292 (1979).

[3] E. Witten, Phys. Rev. **D30**, 272 (1984).

[4] G.L. Shaw, M. Shin, R.H. Dalitz and M. Desai, Nature **337**, 436 (1989).

[5] Workshop on Strange Quark Matter in Physics and Astrophysics, Århus, Denmark, May 1991. Proceedings of this workshop will appear as a Nucl. Phys. B supplement.

[6] C. Baglin *et al.*, *Letter of Intent: Search for Strangelets and Free Quarks in Pb-Pb Collisions*, CERN/SPSLC91-41, SPSLC/I 183, 20 August 1991.

[7] E. Farhi and R.L. Jaffe, Phys. Rev. **D30**, 2379 (1984) and D32, 2452 (1985).

[8] J. Barrette *et al.*, Phys. Lett. **B252**, 550 (1990).

[9] F.S. Rotondo, *Limits on Strange Quark Matter Production*, Ph.D. thesis, Yale University, May 1991.

[10] J.V. Germani, thesis in preparation.

[11] S.V. Greene, thesis in preparation.

[12] D. Acosta, *et al.*, Nucl. Instrum. and Meth. **A294**, 193 (1990).

[13] C. Greiner and H. Stöcker, *Distillation and survival of strange quark matter droplets in ultrarelativistic heavy ion collisions*, preprint July 1991.

[14] O. Hansen, Comments Nucl. Part. Phys. **20**, 1 (1991).

[15] V.B. Kopeliovich, B. Schwesinger and B.E. Stern, Phys. Lett. **B242**, 145 (1990).

[16] R. Slansky *et al.*, Phys. Rev. Lett. **47**, 887 (1981).

[17] R. Saly *et al.*, Phys. Lett. **B115**, 239 (1982).

[18] R.L. Rinfret and P.J.S. Watson, Phys. Lett. **B200**, 177 (1988).

[19] V.S. Berezinsky, J. Ellis, and B.L. Ioffe, Phys. Lett. **B172**, 423 (1988).

[20] J. Kapusta, Phys. Rev. **C21**, 1301 (1980).

[21] S. Nagamiya *et al.*, Phys. Rev. **C24**, 971 (1981).

[22] H. Crawford, private communication (Experiment E858) (1991).

[23] M.S. Berger and R.L. Jaffe, Phys. Rev. **C35**, 213 (1987), (erratum in Phys. Rev. **C44**, 566 (1991)); the surface tension σ is to be increased by a factor two).

[24] F. Curtis Michel, Phys. Rev. Lett. **60**, 677 (1988).

[25] A.Z. Mekjian, Phys. Rev. **C17**, 1051 (1978).

[26] J.L. Bailly *et al.*, Phys. Lett. **B195**, 609 (1987).

[27] C. Greiner, D.H. Rischke, H. Stöcker and P. Koch, Phys. Rev. **D38**, 2797 (1988).

[28] C. Greiner and H. Stöcker, Phys. Rev. D (in press).

[29] H.J. Crawford, M.S. Desai, and G.L. Shaw, *Production of Drops of Strange Matter in Fixed-Target Heavy Ion Collisions*, to appear in the Proc. of the Workshop on Strange Quark Matter in Physics and Astrophysics, Århus, Denmark, May 1991 (Nucl. Phys. B supplement).

[30] NA35 Collaboration, Nucl. Phys. **A498**, 133c–150c (1989).

[31] J.L. Rosner, Phys. Rev. **D33**, 2043 (1986).

[32] A.P. Balachandran *et al.*, Nucl. Phys. **B256**, 525 (1985).

[33] C.G. Callen and I. Klebanov, Nucl. Phys. **B262**, 365 (1985).

[34] J. Kunz and P.J. Mulders, Phys. Lett. **B215**, 449 (1989).

[35] Y. Iwasaki, T. Yoshie and Y. Tsuboi, Phys. Rev. Lett. **60**, 1371 (1988).

[36] U. Straub *et al.*, Phys. Lett. **B200**, 241 (1988).

[37] Y. Koike, K. Shimizu and K. Yazaki, Nucl. Phys. **A513**, 653 (1990).

[38] M. Oka and S. Takeuchi, Nucl. Phys. **A524**, 649 (1991).

[39] G.B. Franklin, Nucl. Phys. **A450**, 117c (1986).

[40] A.T.M. Aerts and C.B. Dover, Phys. Rev. **D28**, 450 (1983).

[41] A.T.M. Aerts and C.B. Dover, Phys. Rev. **D29**, 433 (1984).

[42] C.B. Dover, P. Koch, and M. May, Phys. Rev. **C40**, 115 (1989).

[43] C.B. Dover, U. Heinz, E. Schnedermann and J. Zimanyi, Phys. Rev. C (October 1991).

[44] J.F. Donoghue, E. Golowich and B.R. Holstein, Phys. Rev. **D34**, 3434 (1986).

[45] C.B. Dover, Nuovo Cimento **A102**, 521 (1989).

[46] V.B. Kopeliovich, Yad. Fiz. **51**, 241 (1990) [Sov. J. Nucl. Phys. **51**, 151 (1990)].

[47] V.B. Kopeliovich, B. Schwesinger and B.E. Sterm, Phys. Lett. **B242**, 145 (1990).

[48] J.B. Costales, *Antiproton Production in Central Nucleus–Nucleus Collisions at 14.6 GeV/A*, Ph.D. Thesis, M.I.T. (1990); this thesis contains an extensive list of references and a critical discussion of theoretical models.

[49] S. Gavin, M. Gyulassy, M. Plümer and R. Venugopalan, Phys. Lett. **B234**, 175 (1990).

[50] J. Ellis, U. Heinz and H. Kowalski, Phys. Lett. **B233**, 223 (1989).

[51] U. Heinz, P.R. Subramanian, H. Stöcker and W. Greiner, J. Phys. **G12**, 1237 (1986).

[52] C.B. Dover, Proceedings of the Workshop on Heavy Ion Physics at the AGS, Brookhaven National Lab., BNL-44520, March 1990.

[53] L.D. Csernai and J. Kapusta, Phys. Rep. **131**, 223 (1986).

[54] J. Stevenson *et al.*, Phys. Rev. **C37**, 2220 (1988).

[55] T. Abbott *et al.*, Phys. Rev. Lett. **64**, 847 (1990).

[56] S. Ahlen, *et al.*, Particle World, 1, 168 (1990), and references therein.

[57] J. Fischer, *et al.*, Nucl. Instrum. and Meth. **A238**, 1249 (1988).

[58] R. Wigmans, *The Spaghetti Calorimeter Project at Cern*, Proceedings of the Summer Study on High Energy Physics in the 1990's, June 27–July 15, 1988, Snowmass, Colorado. World Scientific.

[59] A. Para, *et al.*, *Scintillator Based Calorimetry for the SSC. A Subsystem Proposal.* October 2, 1989.

[60] P. Cushman, private communication.

[61] M. Livan, Talk presented at Boston University, 18 June 1990.

[62] S. Amato, S. Bracker, J.M. de Miranda, C. James, J.R.T. de Mello Neto, D. Summers, *The E791 Data Acquisition Software*, E791 Internal Note.

[63] W. Busza and R. Ledoux, *Ann. Rev. of Nucl. and Part. Sci.*, **38**, 119 (1988).

[64] B. Lu, L.W. Mo, and T.A. Nunamaker, Virginia Polytechnic Institute preprint VPI-IHEP-91/1.

[65] J.A. Kadyk *et al.*, *Detector Research and Development for the Superconducting Super Collider*, 236, World Scientific, 1990.

[66] P. Baringer, *et al.*, Nucl. Instr. and Meth. **A254**, 542 (1987).

[67] H. Crawford, *et al.*, Nucl. Instr. and Meth. **A241**, 265 (1985).

[68] S. Ahlen *et al.*, Particle World 1, 168 (1990).

[69] C. Biino *et al.*, Nucl. Instrum. and Meth. **A271**, 417 (1988)

[70] W. Robertson, private communication.

[71] G. Alverson *et al.*, *Direct Photon Production in* π^-*-Be Collisions at 530 Gev/c*, Proc. XXV International Conference on High Energy Physics, Singapore, August 1990. See also G. Alverson *et al.*, *Production of* π^0 *and* η *Mesons in Hadronic Collisions at Large* P_t and *Event Structure for Single-Photon Production at 530 Gev/c* in the same reference.

[72] C. Bromberg *et al.*, *Design and Operation of Large Straw-Tube Drift Chamber Planes*, to appear in Nucl. Instrum. and Meth. A.

[73] N.A. Amos *et al.*, FERMILAB-Pub-90/150, submitted to Nucl. Instr. and Meth.,
D. Acosta *et al.*, CERN-PPE/91-45, submitted to Nucl. Instr. and Meth.

[74] L. Poggioli, private communication.

[75] 3M Scotch-Weld 2290 Epoxy Adhesive.

[76] CERN-PPE/91-85, to be published in Nucl. Instr. and Meth.